UNIVERSITY OF CALIFORNIA,
MERCED

Tracing Leopard Shark (*Triakis semifasciata*) Life History Patterns in Northern California Estuaries: Insights from Stable Isotope Ecology

DISSERTATION

submitted in partial satisfaction of the requirements for the degree of

DOCTOR OF PHILOSOPHY
Quantitative Systems Biology

by

Jonathon Peter Kuntz

Dissertation Committee:

Dr. Justin D Yeakel, Chair
Dr. Matthew C Hutchinson
Dr. Sora L Kim, Advisor

2025

Copyright

The dissertation of Jonathon Peter Kuntz is approved and is acceptable in quality and form for publication on microfilm and in digital formats:

Dr. Sora L Kim, Advisor

Dr. Justin D Yeakel, Chair

Dr. Matthew Hutchinson

University of California, Merced
2025

Dedication

This PhD dissertation is dedicated to my parents, grandparents, ancestors, and elders who came before me. Every choice they made, whether big or small, easy or hard, joyous or painful, created the path I now walk. This body of work would not have happened if not for **you**.

Table of Contents

List of Tables

List of Figures

List of Equations

Acknowledgements

This PhD has tested every part of my being. I honestly don't know if I would have made it this far without the incredible support system that lifted me up, step by step.

First and foremost, I want to acknowledge my fiancé, Angela Korabik. Your unwavering love and support—and, of course, our little black cat Igor—have kept me grounded through it all. Whether you were just making me smile, helping me write grants, or staying up with me until 3 a.m. dissecting sharks in the lab, this dissertation simply would not exist without you.

I am deeply grateful to my family, who instilled in me a love for the ocean and its inhabitants that has fueled my curiosity and passion over these years. Mom and Dad, you gave me the space to dream and the support to achieve it. I will always be thankful for that. To my brother Nick, our childhood adventures in nature are the foundation of this work. Your competitiveness and relentless drive to thrive in any situation has always inspired me to keep going, even when I felt like giving up.

To my friends who have become family—from Ohio, to Utah, to Hawai‘i, to California, and now Alaska—thank you. In every place I've called home, I've found an extra family in you. You welcomed me in, gave me laughter, warmth, and a sense of belonging exactly when I needed it. Through every high and low, you reminded me that life is about more than the work—it's about connection, community, and love.

I am also incredibly thankful to all the members of the Stable Isotope Ecosystems Lab at UC Merced who supported me along the way: Robin Trayler, Mario Hernandez, Gabriele Larocca Conte, Hyejoo Ro, Anna Jurusik, Divia Feinstein, Gina Palefsky, Molly Karnes, Rachel Chan, Leila Wahab, Angelique Rea, Lauren Lopes, Ashley Liao, Antonio Gonzalez, Alejandro Montiel Torres, Maya Morris, Alyssa Valdez, and Connie Munyer. Your camaraderie, insight, and encouragement—whether in the lab, at conferences, or during everyday moments—have shaped both my science and my journey as a scholar.

Lastly, I want to acknowledge my advisor, Sora Kim. Sora, I truly would not trade you for any other advisor. You understand that science isn't just about *the science*—it's an avenue to uplift people—and you've consistently challenged me to think about how I can help make our scientific community more equitable. That is, without a doubt, the most meaningful thing I'm taking from this PhD. Additionally, our shared openness has allowed for honest, deeply meaningful conversations, and I've always felt safe bringing my full self into those spaces. For that, and so much more, I am forever grateful.

This project was supported by the NOAA Grant # NA22OAR4170106, California Sea Grant College Program [Project R/HCE-27F], through NOAA'S National Sea Grant College Program, U.S. Dept. of Commerce. AMS salary and analyses funded by a UKRI Future Leaders Fellowship [MR/V023578/1]. The statements, findings, conclusions, and recommendations are those of the author(s) and do not necessarily reflect the views of California Sea Grant, state agencies, NOAA or the U.S. Dept. of Commerce.

Chapter 3 is a full reprint of the material as it appears in Environmental Biology of Fishes: https://doi.org/10.1007/s10641-024-01656-6. © 2024 Springer. Jonathon P. Kuntz contributed to writing, reviewing, and editing both the original and final drafts, as well as conceptualization, methodology, formal analysis, investigation, funding acquisition, resources, and project administration. Miranda Bell-Tilcock contributed to writing, reviewing, and editing both the original and final drafts, as well as methodology. Julie L. Vecchio contributed to writing, reviewing, and editing both the original and final drafts, as well as methodology, formal analysis, investigation, funding acquisition, and resources. Amy A. Wallace contributed to writing, reviewing, and editing, as well as methodology. Anna M. Sturrock contributed to writing, reviewing, and editing, as well as formal analysis, investigation, funding acquisition, and resources. Sean M. Perry contributed to writing, reviewing, and editing, as well as resources. Sora L. Kim contributed to writing, reviewing, and editing both the original and final drafts, as well as conceptualization, funding acquisition, resources, and supervision.

Curriculum Vitae

EDUCATION

2025 **Doctor of Philosophy in Quantitative Systems Biology**

Concentration in Ecology and Evolutionary Biology

University of California – Merced, CA, USA

2017 **Bachelor of Science (B.S.) in Biology**

Concentration in Environmental and Organismal Biology

University of Utah, Salt Lake City, UT, USA

SCIENTIFIC (PEER-REVIEWED) PUBLICATIONS

2024 **Kuntz JP**, Bell-Tilcock M, Vecchio JL, Wallace AA, Sturrock AM, Perry SM, Kim SL. "Investigating eye lens composition for stable isotope analysis in fishes: a comparison between Chondrichthyes and Actinopterygii." *Environmental Biology of Fishes*. (https://doi.org/10.1007/s10641-024-01656-6)

2024 Hofstetter KS, Haas PM, **Kuntz JP**, Zheng Y, Fuhrmann S. "Loss of Cdc42 causes abnormal optic cup morphogenesis and microphthalmia in mouse." *Frontiers in Cellular Neuroscience*. 18:1474010. (https://doi.org/10.3389/fncel.2024.1474010)

2023 Karnes M, Chan RL, **Kuntz JP**, Griffiths ML, Shimada K, Becker MA, Maisch H, Eagle RA, Brenner-Coltrain J, Miller S, Kim SL. "Enigmatic Carbonate Isotope Values in Shark Teeth: Evidence for Environmental and Diet Controls." *Palaeogeography, palaeoclimatology, palaeoecology*, *635*, 111943. (https://doi.org/10.1016/j.palaeo.2023.111943)

2021 Fichman R, Khen A, Willmes M, **Kuntz J**, Scott A, Hobbs J and Lewis L. "The Clever Strategies That Fishes Use to Survive in San Francisco's Dynamic Estuary." *Front. Young Minds*. 9:608881. (https://kids.frontiersin.org/articles/10.3389/frym.2021.608881)

RESEARCH GRANTS/FELLOWSHIPS

2025	Dean's Dissertation Fellowship	$17,000
2022	California Sea Grant Research Fellowship, NOAA	$100,000
2022	ES Professional Development Fellowship, UC Merced	$1,000
2019	Stable Isotope Facility Pilot Project Grant, UC Davis	$1,000
2016	UROP Grant, University of Utah	$1,200
2016	Sustainable Campus Initiative Fund, University of Utah	$1,000

AWARDS

2024 Quantitative Systems Biology Teaching Service Award

2017 Associated Students of the University of Utah Tuition Award

2016 Associated Students of the University of Utah Tuition Award

2014 Associated Students of the University of Utah Assembly Funding Award

2013 Dean's list, University of Utah

RESEARCH POSITIONS

Year started; Position; Principal Investigator

2020 **PhD Candidate (Dr. Sora Kim)**

Stable isotope ecology using chronological tissue types of Leopard Shark (*Triakis semifasciata*).

Pres. University of California – Merced, CA, USA

2018 **Junior Specialist; UC technician series (Dr. James Hobbs and Dr. Levi Lewis)**

Otolith biogeochemistry of Smelts (*Hypomesus transpacificus; Spirinchus thaleichthys*).

University of California – Davis, CA, USA

2018 **Field Technician (Dr. Rebecca Ostertag)**

Hawaiian lowland forest plant community ecology and restoration.

University of Hawai'i – Hilo, HI, USA

2016 **Lab Aide (Dr. Thure Cerling and Dr. Joan Brenner-Coltrain)**

Chronological stable isotope analysis in teeth of Smooth Hammerhead Shark (*Sphyrna zygaena*).

University of Utah, Salt Lake City, UT, USA

RESEARCH POSITIONS (VOLUNTEER)

Year started; Position; Principal Investigator; Volunteer hours

2018 **Lab Aide (Dr. Tim Grabowski) – 40 hours**

Otolith aging and growth estimation for Bluestripe Snapper (Ta'ape; *Lutjanus kasmira*).

University of Hawai'i – Hilo, HI, USA

2017 **Lab Technician (Dr. Richard McKenzie) – 1,032.5 hours**

Mangrove forest blue carbon storage throughout Southeast Asia and Pacific islands.

Institute of Pacific Island Forestry, US Forest Service, Hilo, HI, USA

2015 **Lab Aide (Dr. Vicky Rowntree) – 120 hours**

Tracking Southern Right Whale migration via aerial images.

University of Utah, Salt Lake City, UT, USA

INVITED ACADEMIC SEMINARS AND COURSE GUEST LECTURES

2024 **"The San Francisco Estuary and the Sharks that Call it Home"**

Life and Environmental Sciences Department Colloquium

University of California – Merced, CA, USA

2024 **"Population and Food Web Dynamics of Estuaries"**

ESP 150C — Biological Oceanography

University of California – Davis, CA, USA

2023 **"Anthropogenic Impacts and Downstream Effects to Isotope Systems"**

ES/QSB 278: Stable Isotopes in Ecosystems (Graduate Course)

University of California – Merced, CA, USA

2022 **"Ecological Dynamics of Northern California's Leopard Shark (*Triakis semifasciata*)"**

Biology Department Colloquium Seminar Series

Sonoma State University – Rohnert Park, CA

2022 **"The Role of Science Communication in Marine Ecology"**

ESS/BIO 034: Introduction to Marine Science (Undergraduate Course)

University of California – Merced, CA, USA

2019 **"Stable Isotopic Record of Great Hammerhead Shark Ecology in Series of Teeth"**

Discover Your Niche! Wildlife Professional Development Conference

The Wildlife Society Student Chapter of UC Davis

University of California – Davis, CA, USA

ORAL PRESENTATIONS AT CONFERENCES

2024 **Kuntz JP**, Bell-Tilcock M, Gonzalez A, Pathirana BM, Cooper A, Kim SL. "Comparing Vertebrae and Eye Lenses for Stable Isotope Analysis in Elasmobranchs: A Case Study on the Leopard Shark (*Triakis semifaciata*)." *IsoEcol Semi-Annual Meeting, Fredericton, NB, CAN*

2023 **Kuntz JP**, Bell-Tilcock M, Kim SL. "Leopard Shark Life History with Novel Application of Stable Isotopes in Eye Lenses." *57th American Fisheries Society Cal-Neva Annual Chapter Meeting, Long Beach, CA, USA*

POSTER PRESENTATIONS AT CONFERENCES

2024 Rea A, **Kuntz JP**, and Kim SL. "Leopard Shark Teeth Series Reveal Life History Patterns with Stable Isotopes." *Society for Integrative and Comparative Biology Annual Meeting, Seattle, WA, USA*

2023 Montiel Torres A, **Kuntz JP**, Larocca Conte G, Rea A, and Kim SL. "Leopard Shark Teeth Track Seasonal Life History Patterns Between Estuarine and Marine Ecosystems with Stable Isotopes." *Undergraduate Research Opportunities Center Summer Symposium, Merced, CA, USA*

2023 **Kuntz JP**, Bell-Tilcock M, Cooper A, Johnson RC, Jeffres C, and Kim SL. "Stable Isotope Analysis in the Eye Lens of Fishes." *1st annual Northern California Geobiology symposium, Stanford, CA, USA*

2023 Ly R, Hernandez M, **Kuntz JP**, and Kim SL. "California Leopard Shark (*Triakis semifasciata*) Parturition through Stable Isotopes." *57th American Fisheries Society Cal-Neva Annual Chapter Meeting, Long Beach, CA, USA*

2022 Rea A, **Kuntz JP**, and Kim SL. "Leopard Shark Teeth Series Reveal Life History Patterns with Stable Isotopes." *Undergraduate Research Opportunities Center Summer Symposium, Merced, CA, USA*

2022 **Kuntz JP**, Bell-Tilcock M, Vecchio J, Johnson RC, Jeffres C, and Kim SL. "Enhancing our Understanding of Stable Isotope Analysis in the Eye Lens of Fishes." *107th Ecological Society of America Annual Conference, Montreal, CAN*

2019 **Kuntz J**, Lewis L, Willmes M, and Hobbs J. "Habitat Use and Diet Composition of Leopard Shark in the San Francisco Estuary." *100th Western Society of Naturalists Annual Conference, Ensenada, MEX*

2019 **Kuntz J**, Lewis L, Willmes M, and Hobbs J. "Habitat Use and Diet Composition of Leopard Shark in the San Francisco Estuary." *149th American Fisheries Society & The Wildlife Society Joint Annual Conference, Reno, NV, USA*

2019 Lewis L, Willmes M, Denney C, **Kuntz J**, Scott A, and Hobbs J. "The Delta's Smelts: Life History Diversity within a Highly-Modified and Ever-Changing Environment" *149th American Fisheries Society & The Wildlife Society Joint Annual Conference, Reno, NV, USA*

TEACHING, MENTORING, AND SCIENCE COMMUNICATION DEVELOPMENT

2023 **Workshop Panelist: "Path to Graduate School"**

Diversifying Ocean Sciences Program

2023 **Workshop Panelist: "Grant Writing with MISS"**

Minorities in Shark Sciences

2021 **Pod Participant: Unlearning Racism in Geoscience (URGE)**

PROFESSIONAL SERVICE

2024 **NSF Leading Culture Change Through Professional Societies of Biology (BIO-LEAPS) Advisory Board**

2023 **Graduate Dean's Advisory Council on Diversity**

University of California – Merced, CA, USA

2017 **Associate Director of Sustainability**

Associated Students of the University of Utah, Salt Lake City, UT, USA

TEACHING POSITIONS AND COURSES TAUGHT

2024 **Graduate Instructor**

- UCSB Smithsonian Scholars Program – Led a 5-week summer R-code training program for first-gen community college students. The program is a partnership between UC Santa Barbara, the Smithsonian National Zoo and Conservation Biology Institute, and local community colleges. The program brings together diverse students of historically marginalized backgrounds, for a summer learning experience focused on conservation ecology, biodiversity, and green careers in STEM.

2021 **Teaching Assistant**

Department of Life & Environmental Sciences, University of California – Merced, CA

- ESS 001: Intro to Earth Systems Science (Fa21, Sp22, Fa23, Fa24)
- ESS/BIO 174: Stable Isotope Fundamentals (Fa22)

COMMUNITY ENGAGEMENT AND OUTREACH

2022 **Bobcat STEM Summer Academy (Middle School)**

Taught a two-week summer ocean science module for CalTeach, which is a program designed to address the shortage of STEM teachers in the Central Valley's underserved school systems.

CalTeach, University of California – Merced, CA, USA

2021 **Frontiers for Young Minds (Middle School)**

Frontiers for Young Minds (FFYM) is a kids journal specifically geared towards simplifying your science down for ages 8-15. The best part? Kids are the reviewers! My colleagues and I published a Core Concept (i.e., explains fundamental ideas from a field) paper in FFYM's San Francisco Bay collection to increase accessibility and understanding for kids learning about estuarine fish life history strategies in the San Francisco Bay Estuary (see publication list above).

Where the River Meets the Ocean: Stories from the San Francisco Estuary – FFYM

2018 **Ka ‘Umeke Ka’eo, Liko Nā Pilina Restoration Project (Elementary School)**

Lead field and classroom lessons on culturally important plant ecology with the University of Hawai’i – Hilo, where students presenting their end of year findings entirely in their native Hawaiian language.

Ka ‘Umeke Ka’eo Hawaiian immersion charter school, Hilo, HI

UNDERGRADUATE STUDENTS MENTORED AS RESEARCH ASSISTANTS

Year(s); Name; Institution (Students consented to their inclusion here)

2023 – 2024	Antonio Gonzales	University of California – Merced, USA
2023 – 2024	Alejandro Montiel Torres	Instituto Politécnico Nacional – Mexico
2022 – 2023	Russel Ly	University of California – Merced, USA
2021 – 2024	Angelique Rea	University of California – Merced, USA
2019 – 2020	Lee Burrows	University of California – Davis, USA
2018 – 2020	Jonathan Huang	University of California – Davis, USA

WORKSHOPS & CONTINUED EDUCATION COURSES TAKEN

2024 **Collective Alaska Native Perspectives Workshop**

Chugach Regional Resource Commission, Kodiak, AK, Alutiiq Land

2023 **Isotopes in Spatial Systems (SPATIAL) Short Course**

University of Utah, Salt Lake City, UT, USA

2016 **IsoCamp (SIRFER) Short Course**

University of Utah, Salt Lake City, UT, USA

CERTIFIED SKILLS & COURSES TAKEN

2022 **Motorboat Operator Training Course (MOTC)**

Bodega Marine Laboratory Boating Safety Program

University of California – Davis, CA, USA

2016 **Open Water Scuba Diver, Scuba Diving International (SDI)**

University of Utah, UT, USA

Abstract of the Dissertation

Despite their ecological importance, many aspects of chondrichthyan (cartilaginous fishes; sharks, skates, rays, and chimeras) biology remain poorly understood, even as their populations face widespread decline due to anthropogenic pressures. Native to California's estuarine and coastal systems, the Leopard Shark (*Triakis semifasciata*) is a generalist mesopredator whose foraging ecology, movement, and response to environmental change are still not fully understood—particularly in heavily impacted estuaries like the San Francisco Bay Estuary (SFBE). This dissertation uses bulk stable isotope analysis (SIA) and compound-specific isotope analysis of amino acids (CSIA-AA) to investigate the trophic ecology, site fidelity, and habitat connectivity of Leopard Shark subpopulations across four Northern California sites: the SFBE, Drakes Estero, Tomales Bay, and Bodega Bay. These estuarine systems differ in hydrodynamics, nutrient regimes, and conservation protections, making them ideal for exploring how environmental context shapes resource use. Here, I develop high-resolution $\delta^{13}C$ and $\delta^{15}N$ isoscapes across the SFBE to track spatial variation in baseline isotope values, which are influenced by nutrient inputs, especially from wastewater. I then use bulk tissue SIA and chronological tooth samples to assess seasonal movement and localized habitat use, revealing long-term site fidelity and distinct isotopic niches among regions. CSIA-AA $\delta^{13}C$ fingerprinting further shows that estuarine and bay habitats support different productivity pathways. Finally, I pioneer the use of eye lenses as a novel chronological tissue to reconstruct long-term trophic life histories in Chondrichthyans, offering insight into lifetime dietary patterns and habitat use. Together, these studies demonstrate that Leopard Sharks exhibit high habitat fidelity and flexibility in resource use, shaped by the isotopic and ecological characteristics of their environment. This work provides critical insight into how anthropogenic change impacts mesopredator ecology and highlights the utility of isotope-based tools for studying long-term movement and foraging strategies in estuarine systems.

1. Introduction to the Dissertation

1.1 Introduction

Despite their ecological importance and evolutionary legacy, much about Chondrichthyes—cartilaginous fishes including sharks, skates, rays, and chimeras—remains unknown (Stein et al., 2018), even as their populations, particularly sharks, have suffered dramatic global declines in recent decades due to mounting anthropogenic pressures (Baum et al., 2003; Dulvy et al., 2014, 2021; Pacoureau et al., 2021; Roff et al., 2018). Today, nearly one-third of all chondrichthyan species are considered threatened due to human activity (Dulvy et al., 2014). As many apex chondrichthyans decline, a cascading ecological response has emerged in the form of 'mesopredator release'—a phenomenon in which mid-level predatory chondrichthyans increase in abundance in the absence of top-down control (Brashares et al., 2010). Mesopredators play a crucial ecological role by linking upper and lower trophic levels (Prugh et al., 2009), and shifts in their abundance can profoundly alter food web dynamics (Ferretti et al., 2010; Myers et al., 2007; Ritchie & Johnson, 2009). Such trophic shifts underscore the far-reaching consequences of human impacts on marine ecosystems, with anthropogenic pressures not only depleting apex predators but also restructuring community composition and ecosystem functioning at multiple trophic levels.

A key mesopredator that may be subject to these broader trophic shifts is the Leopard Shark (*Triakis semifasciata*), a species endemic to California's coastal and estuarine ecosystems (Ebert, 2003; Ebert & Ebert, 2005) and supports a primarily recreational fishery (Smith, 2001). The species is considered a generalist and exhibits behavioral plasticity in response to shifting environmental conditions (Ackerman et al., 2000; Carlisle & Starr, 2010; Hopkins & Cech, 2003). As a native predator that occupies a mid-trophic position, the Leopard Shark plays an important role in regulating lower trophic levels. Despite its ecological importance, many aspects of the Leopard Shark's life history remain poorly understood, particularly in vulnerable estuarine environments. However, the species has emerged as a model organism in marine biogeochemical research, particularly through the use of stable isotope analysis (SIA)—a powerful tool for reconstructing diet, habitat use, and trophic interactions over time (Kim, Casper, et al., 2012; Kim, Del Rio, et al., 2012; Kim, Tinker, et al., 2012; Kim & Koch, 2012; Kuntz et al., 2024; Whiteman et al., 2018). As such, the Leopard Shark offers a unique opportunity to investigate how environmental and ecological changes shape resource use and trophic dynamics in estuarine systems.

The SIA of carbon and nitrogen ($\delta^{13}C$ and $\delta^{15}N$) can uncover consumer diet, trophic interactions, and habitat use, as these isotopes are derived from nutritional resources in the environment and incorporated into body tissues (Fry, 2006). The $\delta^{13}C$ and $\delta^{15}N$ values in a consumer reflect both the isotopic signatures of primary producers at the base of the

food web and the physiological discrimination between heavy and light isotopes that occurs during metabolism (DeNiro & Epstein, 1978; Post, 2002). Baseline $\delta^{13}C$ and $\delta^{15}N$ values in primary producers vary due to differences in carbon and nitrogen sources and biogeochemical cycling. As the isotopic composition of primary producers is propagated through food webs, heavier isotopes (^{13}C and ^{15}N) biomagnify in consumer tissues due to preferential excretion of lighter isotopes (^{12}C and ^{14}N), resulting in trophic enrichment (DeNiro & Epstein, 1978; Post, 2002). However, accurate ecological interpretation of these values depends on understanding two critical parameters: consumer tissue-specific incorporation rates, which determine the timescale of dietary isotopic integration, and trophic discrimination factors (TDFs), which quantify the isotopic offset between a consumer and its diet. While both trophic discrimination and baseline isotopic variation contribute to the isotopic composition of consumers, it is the spatial and temporal variability in baseline values that fundamentally structures ecosystem-level isotopic gradients. Therefore, understanding baseline dynamics is essential for tracing energy flow and disentangling ecological processes across heterogeneous environments.

Isotopic baselines are fundamentally shaped by the nutrients available to primary producers and the biogeochemical processes that govern their uptake. The $\delta^{13}C$ and $\delta^{15}N$ values in aquatic primary producers—such as phytoplankton, macroalgae, and aquatic or terrestrial plants—reflect differences in carbon and nitrogen assimilation pathways, which are themselves influenced by the availability of inorganic nutrient species (e.g., CO_2, HCO_3^-, NH_4^+, and NO_3^-). In particular, anthropogenic nitrogen inputs—primarily wastewater-derived NH_4^+ and NO_3^-—drive eutrophication and introduce nitrogen with elevated and variable $\delta^{15}N$ values into estuarine systems (McClelland et al., 1997), creating distinct isotopic signals that are incorporated into local food webs. These dynamics, particularly in the San Francisco Bay Estuary (SFBE) are shaped by the system's unique geography: water originating in the Sierra Nevada flows through the Sacramento-San Joaquin Delta into the lower estuary, passing through Suisun Bay, Carquinez Strait, San Pablo Bay, and Central Bay before reaching the Pacific Ocean. The South Bay, in contrast, functions as a semi-enclosed brackish lagoon with longer residence times and reduced freshwater input, making it particularly susceptible to nutrient retention. Hydrodynamic processes—including freshwater inflow, tidal mixing, and estuarine circulation—modulate nutrient residence times (Cloern & Jassby, 2012) and, consequently, the opportunity for primary producers to assimilate these isotopically distinct nutrient sources. Together, these processes establish complex and dynamic gradients of isotopic baselines across the SFBE.

Given the complexity of hydrological and nutrient dynamics across the SFBE, understanding how $\delta^{13}C$ and $\delta^{15}N$ values vary spatially and temporally is critical for interpreting the movement patterns and food web interactions of the Leopard Shark in this system. This is especially important in the SFBE, which serves as a vital nursery and foraging ground for a subpopulation of the northern genetic stock of Leopard Sharks (Barker et al., 2015; Hughes et al., 2014; Russo, 2019). Unlike the broader southern genetic population, which has shown signs of recovery following fishery regulations implemented in the mid-1990s (Pondella & Allen, 2008), the SFBE subpopulation has continued to exhibit signs of localized decline over the past four decades (Kuntz et al.,

2019), further compounded by episodic mass mortality events (Retallack et al., 2019). Investigating the ecology of this estuarine subpopulation within an isotopically dynamic landscape offers a unique opportunity to explore how environmental variability shapes resource use and trophic dynamics across space and time.

Understanding the ecology of the SFBE subpopulation requires a broader view of the northern genetic lineage of Leopard Sharks, which spans several estuarine and coastal habitats from central to northern California. While the SFBE remains a region of concern due to ongoing declines and episodic mortality events (Kuntz et al., 2019; Retallack et al., 2019), it is embedded within a network of nearby estuarine systems—including Drakes Estero State Marine Conservation Area (SMCA), Tomales Bay, and Bodega Bay—that are also utilized by this northern genetic population (Barker et al., 2015). These localities differ in hydrodynamics, conservation protections, and anthropogenic inputs, presenting a unique opportunity to investigate movement ecology, habitat connectivity, and trophic life history across a mosaic of environmental contexts. By leveraging the isotopic distinctiveness of each site, this study aims to examine how Leopard Sharks move among and forage within these habitats. The goals of this dissertation are fourfold: (1) to create a fine-scale isoscape of the SFBE that captures spatial variation in $\delta^{13}C$ and $\delta^{15}N$ values; (2) to use SIA and compound-specific isotope analysis of amino acids (CSIA-AA) to examine short-term movement and trophic interactions across localities; (3) to evaluate the potential of eye lenses as a chronological substrate for SIA; and (4) to validate the use of eye lenses for reconstructing long-term movement and trophic interactions in the Leopard Shark. Together, these chapters will provide a comprehensive view of how ecological, environmental, and physiological factors shape the trophic life history of this estuarine mesopredator across its northern range.

1.2 References

Ackerman, J. T., Kondratieff, M. C., Matern, S. A., & Cech, J. J. (2000). Tidal influence on spatial dynamics of leopard sharks, Triakis semifasciata, in Tomales Bay, California. Environmental Biology of Fishes, 58(1), 33–43. https://doi.org/10.1023/A:1007657019696

Barker, A. M., Nosal, A. P., Lewallen, E. A., & Burton, R. S. (2015). Genetic structure of leopard shark (Triakis semifasciata) populations along the Pacific coast of North America. Journal of Experimental Marine Biology and Ecology, 472, 151–157. https://doi.org/10.1016/j.jembe.2015.06.020

Baum, J. K., Myers, R. A., Kehler, D. G., Worm, B., Harley, S. J., & Doherty, P. A. (2003). Collapse and conservation of shark populations in the Northwest Atlantic. Science, 299(5605), 389–392. https://doi.org/10.1126/science.1079777

Brashares, J. S., Prugh, L. R., Stoner, C. J., & Epps, C. W. (2010). Ecological and conservation implications of mesopredator release. In Trophic cascades: predators, prey, and the changing dynamics of nature (pp. 221–240).

Carlisle, A. B., & Starr, R. M. (2010). Tidal movements of female leopard sharks (Triakis semifasciata) in Elkhorn Slough, California. Environmental Biology of Fishes, 89(1), 31–45. https://doi.org/10.1007/s10641-010-9667-0

Cloern, J. E., & Jassby, A. D. (2012). Drivers of change in estuarine-coastal ecosystems: Discoveries from four decades of study in San Francisco Bay. Reviews of Geophysics, 50(4), 1–33. https://doi.org/10.1029/2012RG000397

DeNiro, M. J., & Epstein, S. (1978). Influence of diet on the distribution of carbon isotopes in animals. Geochemica et Cosmochimica Acta, 42, 495–506. https://doi.org/10.1002/mop.25285

Dulvy, N. K., Fowler, S. L., Musick, J. A., Cavanagh, R. D., Kyne, P. M., Harrison, L. R., Carlson, J. K., Davidson, L. N., Fordham, S. V, Francis, M. P., Pollock, C. M., Simpfendorfer, C. A., Burgess, G. H., Carpenter, K. E., Compagno, L. J., Ebert, D. A., Gibson, C., Heupel, M. R., Livingstone, S. R., … White, W. T. (2014). Extinction risk and conservation of the world's sharks and rays. ELife, 3, 1–34. https://doi.org/10.7554/elife.00590

Dulvy, N. K., Pacoureau, N., Rigby, C. L., Pollom, R. A., Jabado, R. W., Ebert, D. A., Finucci, B., Pollock, C. M., Cheok, J., Derrick, D. H., Herman, K. B., Sherman, C. S., VanderWright, W. J., Lawson, J. M., Walls, R. H. L., Carlson, J. K., Charvet, P., Bineesh, K. K., Fernando, D., … Simpfendorfer, C. A. (2021). Overfishing drives over one-third of all sharks and rays toward a global extinction crisis. Current Biology, 31(21), 4773-4787.e8. https://doi.org/10.1016/j.cub.2021.08.062

Ebert, D. A. (2003). Sharks, rays and chimaeras of California. In University of California Press, Berkely, CA.

Ebert, D. A., & Ebert, T. B. (2005). Reproduction, diet and habitat use of leopard sharks, Triakis semifasciata (Girard), in Humboldt Bay, California, USA. Marine and Freshwater Research, 56(8), 1089–1098. https://doi.org/10.1071/MF05069

Ferretti, F., Worm, B., Britten, G. L., Heithaus, M. R., & Lotze, H. K. (2010). Patterns and ecosystem consequences of shark declines in the ocean. Ecology Letters, 13(8), 1055–1071. https://doi.org/10.1111/j.1461-0248.2010.01489.x

Fry, B. (2006). Stable Isotope Ecology (521st ed.). Springer.

Hopkins, T. E., & Cech, J. J. (2003). The influence of environmental variables on the distribution and abundance of three elasmobranchs in Tomales Bay, California. Environmental Biology of Fishes, 66(3), 279–291. https://doi.org/10.1023/A:1023907121605

Hughes, B. B., Levey, M. D., Brown, J. A., Fountain, M. C., Carlisle, A. B., Litvin, S. Y., Greene, C. M., Heady, W. N., & Gleason, M. G. (2014). Nursery functions of U.S. West Coast estuaries: The state of knowledge for juveniles of focal invertebrates and fish species. 168.

Kim, S. L., Casper, D. R., Galván-Magaña, F., Ochoa-Díaz, R., Hernández-Aguilar, S. B., & Koch, P. L. (2012). Carbon and nitrogen discrimination factors for elasmobranch soft tissues based on a long-term controlled feeding study. Environmental Biology of Fishes, 95(1), 37–52. https://doi.org/10.1007/s10641-011-9919-7

Kim, S. L., Del Rio, C. M., Casper, D., & Koch, P. L. (2012). Isotopic incorporation rates for shark tissues from a long-Term captive feeding study. Journal of Experimental Biology, 215(14), 2495–2500. https://doi.org/10.1242/jeb.070656

Kim, S. L., & Koch, P. L. (2012). Methods to collect, preserve, and prepare elasmobranch tissues for stable isotope analysis. Environmental Biology of Fishes, 95(1), 53–63. https://doi.org/10.1007/s10641-011-9860-9

Kim, S. L., Tinker, M. T., Estes, J. A., & Koch, P. L. (2012). Ontogenetic and Among-Individual Variation in Foraging Strategies of Northeast Pacific White Sharks Based on Stable Isotope Analysis. PLoS ONE, 7(9). https://doi.org/10.1371/journal.pone.0045068

Kuntz, J. P., Bell-Tilcock, M., Vecchio, J. L., Wallace, A. A., Sturrock, A. M., Perry, S. M., & Kim, S. L. (2024). Investigating eye lens composition for stable isotope analysis in fishes: a comparison between Chondrichthyes and Actinopterygii. Environmental Biology of Fishes. https://doi.org/10.1007/s10641-024-01656-6

Kuntz, J. P., Lewis, L. S., Willmes, M., & Hobbs, J. A. (2019). Habitat use and diet composition of Leopard Sharks (Triakis semifasciata) in the San Francisco Estuary. American Fisheries Society Symposium.

McClelland, J. W., Valiela, I., & Michener, R. H. (1997). Nitrogen-stable isotope signatures in estuarine food webs: A record of increasing urbanization in coastal watersheds. Limnology and Oceanography, 42(5 I), 930–937. https://doi.org/10.4319/lo.1997.42.5.0930

Myers, R. A., Baum, J. K., Shepherd, T. D., Powers, S. P., & Peterson, C. H. (2007). Cascading effects of the loss of apex predatory sharks from a coastal ocean. Science, March, 1846–1850.

Pacoureau, N., Rigby, C. L., Kyne, P. M., Sherley, R. B., Winker, H., Carlson, J. K., Fordham, S. V., Barreto, R., Fernando, D., Francis, M. P., Jabado, R. W., Herman, K. B., Liu, K. M., Marshall, A. D., Pollom, R. A., Romanov, E. V., Simpfendorfer, C. A., Yin, J. S., Kindsvater, H. K., & Dulvy, N. K. (2021). Half a century of global decline in oceanic

sharks and rays. Nature, 589(7843), 567–571. https://doi.org/10.1038/s41586-020-03173-9

Pondella, D. J., & Allen, L. G. (2008). The decline and recovery of four predatory fishes from the Southern California Bight. Marine Biology, 154(2), 307–313. https://doi.org/10.1007/s00227-008-0924-0

Post, D. M. (2002). Using stable isotopes to estimate trophic position: Models, methods, and assumptions. Ecology, 83(3), 703–718. https://doi.org/10.1890/0012-9658(2002)083[0703:USITET]2.0.CO;2

Prugh, L. R., Stoner, C. J., Epps, C. W., Bean, W. T., Ripple, W. J., Laliberte, A. S., & Brashares, J. S. (2009). The rise of the mesopredator. BioScience, 59(9), 779–791. https://doi.org/10.1525/bio.2009.59.9.9

Retallack, H., Okihiro, M. S., Britton, E., Van Sommeran, S., & Derisi, J. L. (2019). Metagenomic next-generation sequencing reveals miamiensis avidus (Ciliophora: Scuticociliatida) in the 2017 epizootic of leopard sharks (Triakis semifasciata) in san francisco bay, California, USA. Journal of Wildlife Diseases, 55(2), 375–386. https://doi.org/10.7589/2018-04-097

Ritchie, E. G., & Johnson, C. N. (2009). Predator interactions, mesopredator release and biodiversity conservation. Ecology Letters, 12(9), 982–998. https://doi.org/10.1111/j.1461-0248.2009.01347.x

Roff, G., Brown, C. J., Priest, M. A., & Mumby, P. J. (2018). Decline of coastal apex shark populations over the past half century. Communications Biology, 1(223), 1–11. https://doi.org/10.1038/s42003-018-0233-1

Russo, R. A. (2019). Primary and secondary nursery areas for leopard and brown smoothhound sharks in San Francisco Bay, California. California Fish and Game, 105(1), 21–30.

Stein, R. W., Mull, C. G., Kuhn, T. S., Aschliman, N. C., Davidson, L. N. K., Joy, J. B., Smith, G. J., Dulvy, N. K., & Mooers, A. O. (2018). Global priorities for conserving the evolutionary history of sharks, rays and chimaeras. Nature Ecology and Evolution, 2(2), 288–298. https://doi.org/10.1038/s41559-017-0448-4

Whiteman, J. P., Kim, S. L., McMahon, K. W., Koch, P. L., & Newsome, S. D. (2018). Amino acid isotope discrimination factors for a carnivore: physiological insights from leopard sharks and their diet. Oecologia, 188(4), 977–989. https://doi.org/10.1007/s00442-018-4276-2

2. Chapter 1: Mapping complexity in the San Francisco Bay Estuary — Carbon and nitrogen isoscapes to reveal spatiotemporal dynamics

2.1 Introduction:

The San Francisco Bay Estuary (SFBE) is one of the most extensively studied estuarine systems in the world, yet critical gaps remain in understanding the biogeochemical processes that shape its stable isotope dynamics (Cloern et al., 2002). The stable isotope compositions of carbon ($\delta^{13}C$) and nitrogen ($\delta^{15}N$) serve as powerful tracers for studying diet, trophic interactions, and movement patterns in both terrestrial and aquatic systems (Fry, 2006). However, accurately interpreting these tracers requires accounting for spatial and temporal variation in baseline isotope values. Isoscapes—spatially explicit models of isotopic variation—offer a crucial tool for refining our understanding of biogeochemical cycling by integrating spatial and temporal data (Bowen, 2010). These models capture how environmental conditions and biogeochemical processes influence isotope distributions, providing a framework for assessing ecological connectivity (Graham et al., 2010). Despite their utility, isoscapes remain largely undeveloped for estuarine systems, including the SFBE, limiting our ability to resolve key biogeochemical and ecological patterns in these critical transition zones between terrestrial and marine ecosystems.

Both $\delta^{13}C$ and $\delta^{15}N$ values offer powerful insights into consumer diet and trophic interactions, as these isotopes are derived from food sources and incorporated into body tissues (Fry, 2006). Primary producers assimilate both carbon and nitrogen, and their isotopic compositions form the foundation of food webs. As primary consumers feed on these producers, and predators feed on consumers, physiological processes differentiate (i.e., fractionate) isotope ratios. For example, nitrogen isotopes undergo stepwise enrichment where lighter isotopes are preferentially excreted, resulting in higher $\delta^{15}N$ values at each successive trophic level (Post, 2002). Meanwhile, $\delta^{13}C$ values tend to show less change across trophic levels, making them useful for tracing basal carbon sources (DeNiro & Epstein, 1978). Because the $\delta^{13}C$ and $\delta^{15}N$ values in a consumer's tissues reflect both the isotopic composition of primary producers and trophic-level fractionation, understanding baseline variation is essential for interpreting trophic dynamics and ecosystem processes (DeNiro & Epstein, 1978; Post, 2002).

Stable isotope analysis (SIA) has already provided valuable insights into the SFBE's nutrient dynamics, primary production, and food web structure. For example, $\delta^{15}N$ has been used to trace inorganic nitrogen sources and cycling, revealing inputs from seawater, riverine discharge, and sewage effluent, with spatial variation driven by estuarine hydrodynamics (Fackrell et al., 2022; Kendall et al., 2015; Lehman et al., 2015; Wankel

et al., 2006). However, most of these studies focused on the upper delta region and excluded fully marine habitat. Additionally, SIA has been applied to food web studies in the SFBE, including assessments of marsh food web structure and predator diets (Schroeter et al., 2015), as well as the role of wetland restoration in supporting food web integrity (Howe & Simenstad, 2011). While these studies demonstrate the utility of SIA in the SFBE, Cloern et al. (2002) found high variability in $\delta^{13}C$ and $\delta^{15}N$ values among plants and organic matter pools across this system, complicating their use as biomarkers for tracing organic matter sources and resolving ecological interactions.

Despite these findings, the absence of a comprehensive isoscape for the SFBE limits our ability to resolve fine-scale spatial and temporal variability in isotope distributions. Developing estuarine isoscapes will refine our understanding of biogeochemical cycling and enhance predictive models of ecosystem change, ultimately improving conservation and management strategies. Here, we integrate biogeochemical and hydrodynamic models with SIA of particulate organic matter (POM) to generate $\delta^{13}C$ and $\delta^{15}N$ isoscapes across the SFBE, addressing the following questions: 1) What biogeochemical processes drive $\delta^{13}C$ and $\delta^{15}N$ variation in the SFBE? 2) Do isoscapes exhibit a clear gradient in $\delta^{13}C$ and $\delta^{15}N$ values from riverine to marine environments across the estuarine transition?

2.2 Methods:

2.2.1 Sampling:

To create isoscapes of the SFBE, we sampled particulate organic matter (POM) at 37 sites across the estuary, spanning both the riverine-dominated North Bay, the marine-lagoon South Bay, estuary-ocean interface, and fully marine habitat (Fig. 2.1). The majority of sampling was conducted during USGS's monthly bay-wide water quality cruises (USGS sampling survey; Fig. 2.1), strategically timed to capture seasonal shifts in organic matter sources. We sampled in October to capture the transition between water year types during a period when freshwater influence is typically at its lowest, following the dry summer months; additional sampling occurred in January and February, during the storm season when high freshwater inflows substantially alter estuarine circulation. Additionally, during the storm season, we sampled two extra sites at the mouth of the SFBE and into the adjacent open ocean habitat to assess how freshwater outflow influences isotopic variability at the estuary-ocean interface (UCM sampling survey; Fig. 2.1). At each site included in the 'training' dataset, biogeochemical variables—including total depth, salinity, total oxygen (OXY), nitrate (NO_3^-), ammonium (NH_4^+), phosphate (PO_4^{3-}), and silicate (Si)—were measured to characterize environmental conditions. The remaining localities were sampled to include in the 'validation' dataset. SFBE water samples were collected onboard the USGS R/V Peterson from a flow-through water system via a 2 m deep intake, which was pre-filtered at 100 μm to remove large particulates. Thereafter, POM was collected onto pre-combusted glass fiber (GF/F) filters (0.7 μm) and subsequently stored frozen at -20°C prior to freeze-drying.

2.2.2 Stable Isotope Analysis

We analyzed POM on glass fiber filters for $\delta^{13}C$ and $\delta^{15}N$ values at the Stable Isotope Ecosystem Laboratory (SIELO) of University of California, Merced. After the initial freeze-drying step of the whole filter, each filter was split in half: one portion was acid-fumigated to remove carbonate for carbon isotope analysis, while the other was left untreated for nitrogen isotope analysis. For $\delta^{13}C$ values, samples were placed in a desiccation chamber, where 50 mL of 12M HCl was added to a beaker and left to evaporate for 6 hours, dissolving carbonate from filter particulates. Post acid fumigation, samples were dried in an oven at 60 C. Both treated and untreated samples were analyzed using an Elemental Analyzer coupled to a continuous-flow Isotope Ratio Mass Spectrometer (EA-cf-IRMS) via Conflo IV. Findings are presented in standard delta notation (δ, ‰), with $\delta^{13}C$ values relative to Vienna Pee Dee Belemnite (VPDB) and $\delta^{15}N$ values relative to V-AIR. Data were corrected for linearity and drift with calibrated reference materials (EA acetanilide [$\delta^{13}C$ = -26.5 ± 0.1 ‰ and $\delta^{15}N$ = -5.1 ± 0.1 ‰, n = 20]; USGS 40 [$\delta^{13}C$ = -26.4 ± 0.1 ‰ and $\delta^{15}N$ = -4.5 ± 0.2 ‰, n = 40]; USGS 41a [$\delta^{13}C$ = 36.5 ± 0.04 ‰ and $\delta^{15}N$ = 47.5 ± 0.1 ‰, n = 14]) and checked with an internal reference material (Mb Squid [$\delta^{13}C$ = -18.7 ± 0.1 ‰ and $\delta^{15}N$ = 11.9 ± 0.2 ‰, n = 8]).

2.2.3 Spatial Modeling

To investigate the relationship between POM isotopic composition and environmental conditions, we applied generalized additive models (GAMs) using the *mgcv* package (Wood, 2017). Separate models were built for $\delta^{13}C$ and $\delta^{15}N$, each modeled as a response variable. Only isotopic data from the designated training sites (Fig. 2.1) were used to fit the models. Predictor variables included smooth terms for USGS-measured biogeochemical parameters, as well as a two-dimensional smooth interaction between latitude and longitude to account for spatial variability. Model selection was assessed using the corrected Akaike Information Criterion (AICc), and model assumptions and residual diagnostics were evaluated using the *DHARMa* package (Hartig, 2022).

To extend the spatial and temporal coverage of biogeochemical conditions across the SFBE, we utilized the San Francisco Estuary Institute's (SFEI) Biogeochemical and Hydrodynamic Model, which has been validated across multiple water years. This model provides spatiotemporal predictions of key USGS-monitored water quality variables that are included as explanatory variables in our GAMs. The SFEI model operates at a high temporal resolution, generating predictions at 30-minute intervals across the entire water year. To align with our observational dataset and reduce computational complexity, we averaged these outputs to annual timescales for a wet water year (2018), a dry water year (2013), and an average water year (2015).

The SFEI model also runs on an irregular grid composed of polygons of varying sizes, necessitating conversion for spatial interpolation. To standardize the data, we extracted centroid coordinates from each polygon to generate a set of point data. We then applied a nearest-neighbor resampling approach to assign values from the original irregular grid to a regularly spaced grid. Since the nearest-neighbor resampling only assigns values from the closest available point, we further refined the spatial

representation using kriging to interpolate a continuous surface. These interpolated estuary-wide datasets were then used to predict POM $\delta^{13}C$ and $\delta^{15}N$ values across the entire SFBE using the GAMs on the training dataset, providing a broader spatial and temporal understanding of organic matter sources and biogeochemical variability. We then used linear regression models from the *stats* package (R Core Team, 2023) to compare predicted versus observed isotope values in both the training and validation datasets, allowing us to evaluate how well the isoscapes captured observed spatial patterns of $\delta^{13}C$ and $\delta^{15}N$ across the SFBE. Finally, we calculated the root mean square error (RMSE) and mean absolute error (MAE) between the predicted isotope values and the validation dataset values. All statistical analyses were performed in R version 4.3.1 (R Core Team, 2023).

2.3 Results:

2.3.1 Statistical Modeling

The best-performing models with accurate $\delta^{13}C$ and $\delta^{15}N$ predictions in the SFBE highlighted strong influences of biogeochemical factors and spatial gradients. Due to the inherent complexity of estuarine gradients, all variables exhibited concurvity (non-linear multicollinearity) with one another, which limited us to modeling only single-term GAMs. For $\delta^{13}C$, the model with the lowest AICc—detailed in Table 2.1—included a smooth term for salinity ($p < 0.001$) and explained a high proportion of variance ($R^2 = 0.88$). The GAM for $\delta^{13}C$ exhibited strong agreement between observed and predicted values (Fig. 2.2A), with linear regressions applied to both the training and validation datasets showing strong fits (training: $y = 1.01x - 0.30$, $R^2 = 0.91$, $p < 0.001$; validation: $y = 0.95x - 1.30$, $R^2 = 0.81$, $p < 0.001$). Additionally, we observed a root mean square error (RMSE) of 0.6 ‰ and an absolute square error (ASE) of 0.5 ‰ for the validation dataset.

To evaluate the drivers of $\delta^{15}N$ variability across the estuary, we identified the top-performing GAM based on AICc (Table 2.2). This model included a two-dimensional smooth interaction between latitude and longitude to account for spatial variability ($p < 0.001$) and explained a large proportion of variance ($R^2 = 0.892$). The GAM for $\delta^{15}N$ values also demonstrated strong agreement between observed and predicted values (Fig. 2.2B), with linear regressions indicating good model performance for both the training ($y = 1.01x - 0.06$, $R^2 = 0.90$, $p < 0.001$) and validation datasets ($y = 0.92x + 0.57$, $R^2 = 0.79$, $p < 0.001$). Additionally, the GAM demonstrated strong predictive performance, with an RMSE of 0.7 ‰ and an ASE of 0.5 ‰ in the validation dataset. These findings underscore the critical role of spatial heterogeneity in shaping $\delta^{13}C$ and $\delta^{15}N$ patterns across the estuary.

2.3.2 Isoscapes

The predicted $\delta^{13}C$ and $\delta^{15}N$ isoscapes of the SFBE reveal a distinct gradient from the freshwater-dominated upper estuary to the marine-influenced Pacific Ocean. This system originates in the Sierra Nevada, with water flowing through the upper SFBE (i.e., Sacramento-San Joaquin Delta) before entering the lower SFBE via the Sacramento River. It then moves through Suisun Bay, Carquinez Strait, San Pablo Bay, and Central Bay before ultimately reaching the Pacific. However, the South Bay functions as a

marine/brackish lagoon, influenced by both the freshwater flow from the upper estuary and the tidal dynamics of the Pacific Ocean. The biogeochemistry, hydrology, and geography of this system play a crucial role in shaping the spatiotemporal distribution of isotopic variation.

Despite variability in hydrologic conditions, we observed remarkably consistent annual $\delta^{13}C$ isoscape patterns across different water year types (2013: dry; 2017: average; 2018: wet; Fig. 2.3), with subtle yet ecologically meaningful differences. In all years, $\delta^{13}C$ values were lowest (~ –28 ‰) in the Sacramento River, reflecting terrestrial carbon inputs, and increased progressively toward the Pacific Ocean (~ –20 ‰), capturing the transition to marine-derived carbon sources (Fig. 2.3). However, the spatial extent and magnitude of this gradient varied slightly among years. For instance, in the dry year (2013; Fig. 2.3A), the plume of low $\delta^{13}C$ values extended farther offshore, suggesting that terrestrial carbon was transported further into the Pacific. During the average water year (2017; Fig. 2.3B), the South Bay exhibited slightly elevated $\delta^{13}C$ values compared to other years. Across all years, the South Bay consistently showed $\delta^{13}C$ values between those of the river and ocean, closely aligning with the Central Bay. This pattern reflects its limited freshwater input and a carbon signature shaped more by estuarine mixing than direct riverine influence.

Unlike $\delta^{13}C$, which was modeled across multiple water years, the predicted annual $\delta^{15}N$ isoscape was based solely on our 2024 collected data, as spatial predictors—specifically latitude and longitude—outperformed hydrological and biogeochemical variables that varied through time. Despite relying on a single water year, the $\delta^{15}N$ isoscape revealed clear and consistent spatial patterns (Fig. 2.4). Values were lowest in the upper estuary (~3 ‰) and increased progressively toward the South Bay, where they peaked around ~10 ‰. Beyond the estuary, $\delta^{15}N$ values followed a distinct north-to-south gradient, with lower values in northern coastal waters and higher values further south. These patterns underscore the dominant role of spatially structured processes—such as estuarine mixing, nutrient availability, and hydrodynamics—in shaping $\delta^{15}N$ distributions across the estuary and adjacent coastal zones.

2.4 Discussion:

2.4.1 Carbon

Carbon isotope values ($\delta^{13}C$) in aquatic systems provide insight into the biogeochemical processes and nutrient dynamics shaping primary production across landscapes. In estuarine ecosystems, $\delta^{13}C$ values in primary producers vary systematically due to differences in carbon sources and assimilation pathways. For instance, phytoplankton preferentially fix $^{12}CO_2$ from dissolved inorganic carbon (DIC), with $\delta^{13}C$ values influenced by upwelling and water temperature (Znachor & Nedoma, 2010). Macroalgae often utilize bicarbonate (HCO_3^-) or CO_2, resulting in relatively enriched $\delta^{13}C$ values (Raven et al., 2002), while terrestrial C_3 plants draw on atmospheric CO_2, with $\delta^{13}C$ values reflecting photosynthetic efficiency and water use (Brugnoli & Farquhar, 2000; Farquhar et al., 1989). These differences create a consistent isotopic gradient across aquatic environments—from low $\delta^{13}C$ values in freshwater systems

dominated by terrestrial detritus to higher $\delta^{13}C$ values in marine systems fueled by phytoplankton and macroalgae (Simenstad & Wissmar, 1985).

This predictable variation was evident in the $\delta^{13}C$ isoscape across the SFBE, which exhibited an increasing gradient from the Sacramento River to the Pacific Ocean, with intermediate values in South San Francisco Bay. The best-performing GAM identified salinity as the strongest predictor of $\delta^{13}C$ variation (Table 2.1). However, we observed little to no change between water year types (Fig. 2.3), likely due to spatial location being the dominant driver in the model. These patterns suggest that spatial location may serve as a proxy for unmeasured environmental drivers of $\delta^{13}C$ variability in the SFBE. Because latitude and longitude are static through time, their inclusion in the model results in consistent spatial gradients in $\delta^{13}C$ values across water year types (Fig. 2.3). However, the presence of salinity, depth, and nitrate among the significant predictors indicates that $\delta^{13}C$ isoscapes are also shaped by hydrologic connectivity, geographic variation, and the spatial distribution of biogeochemical processes within the estuary.

In the upper estuary, low $\delta^{13}C$ values are associated with terrestrial carbon inputs delivered by freshwater flow. These regions are characterized by high nitrate concentrations, low salinity, shallow depths, and upstream spatial locations. In contrast, marine carbon inputs dominate the lower estuary and coastal Pacific, where $\delta^{13}C$ values are higher. These areas are defined by high salinity, low nitrate concentrations, greater depth, and downstream spatial locations—conditions indicative of oceanic influence, including carbon delivery via marine upwelling along the California coast. Additionally, emerging evidence suggests that oxidative processing of terrestrial organic matter can alter its $\delta^{13}C$ values during transport and sedimentation, that may create an estuarine gradient similar to that driven by primary producer differences (Goranov et al., 2025). Therefore, the gradient we observed may reflect both the mixing of distinct carbon sources and the progressive oxidation of terrestrial plant material during its transport from the Sacramento River to the Pacific Ocean.

2.4.2 Nitrogen

Nitrogen isotope values ($\delta^{15}N$) in aquatic primary producers are shaped by the availability and cycling of inorganic nitrogen species, much like how $\delta^{13}C$ values are influenced by carbon source and assimilation pathways. In estuarine environments, $\delta^{15}N$ values reflect both natural and anthropogenic processes that govern nitrogen transformations, including ammonification, nitrification, and denitrification. These processes preferentially act on lighter ^{14}N, enriching the residual nitrogen pool in ^{15}N while producing transformed nitrogen species with lower $\delta^{15}N$ values (Mariotti et al., 1981). Elevated nutrient loading, especially from anthropogenic sources such as wastewater, can amplify these effects. Wastewater-derived ammonium (NH_4^+) and nitrate (NO_3^-) often exhibit high and variable $\delta^{15}N$ values, making them distinct tracers of eutrophication and nitrogen cycling (McClelland et al., 1997). Once introduced, these nitrogen sources become available for uptake by primary producers, embedding the isotopic signatures of their sources and transformation histories into the base of the food web.

We found that the $\delta^{15}N$ isoscape of the SFBE revealed a distinct spatial pattern, with the lowest $\delta^{15}N$ values in the upper estuary and progressively increasing values toward the South Bay, where values peaked. Among the best-performing GAMs, spatial location (latitude and longitude) emerged as the strongest predictor of $\delta^{15}N$ variability (Table 2.2). These patterns suggest that spatial location may serve as a proxy for combined or unmeasured environmental drivers of $\delta^{15}N$ variability that we were unable to model due to statistical and sampling limitations. For example, elevated $\delta^{15}N$ values in the South SFBE likely result from the accumulation and transformation of anthropogenic nitrogen inputs, particularly those from wastewater effluent. This region functions as a semi-enclosed marine lagoon with limited freshwater input, reducing flushing rates and prolonging nitrogen residence time. These conditions—combined with warm temperatures and stratified water columns—create low-oxygen environments that promote denitrification (Diaz & Rosenberg, 2008). Denitrification, particularly at the oxic–anoxic interface of benthic sediments, fractionates nitrogen isotopes by preferentially removing ^{14}N and enriching the remaining nitrate pool in ^{15}N (Christensen et al., 1989; Granger et al., 2008; Mariotti et al., 1981). In contrast, the upper estuary receives high freshwater flow from the Sacramento River, which dilutes nitrogen concentrations, limits residence time, and reduces opportunities for isotopic fractionation. As a result, $\delta^{15}N$ values remain comparatively low in this region. These findings highlight the importance of hydrodynamic conditions—particularly the interplay between nutrient loading, residence time, and oxygen availability—in modulating nitrogen isotope distributions across the estuary.

Outside the estuary, $\delta^{15}N$ values followed a subtle but consistent north-to-south gradient along the California coast, with lower values in the northern marine waters and progressively higher values toward the south. This spatial trend mirrors previously published $\delta^{15}N$ isoscapes of the California Current System, which attribute this pattern to a combination of oceanographic processes, including upwelling intensity, regional nitrogen cycling, and latitudinal variation in anthropogenic inputs (Vokhshoori & Mccarthy, 2014). Our findings extend this coastal gradient into the estuary, suggesting that large-scale marine nitrogen dynamics continue to influence $\delta^{15}N$ values within the SFBE. Overall, the spatial alignment of $\delta^{15}N$ values across both estuarine and coastal waters underscores the interconnected nature of these systems and the role of estuarine mixing, oxygen availability, and anthropogenic nutrient loading in driving $\delta^{15}N$ distributions. In particular, the combination of spatial and biogeochemical predictors highlights the importance of both hydrodynamic transport and localized nitrogen sources—especially those tied to urban wastewater infrastructure—in shaping the nitrogen isotope landscape of this complex estuarine–coastal system.

2.4.3 Implications for Isoscape Applications

These results have important implications for the application of isoscapes in ecological and biogeochemical studies in the SFBE. The consistent spatial patterning and strong predictive performance of both $\delta^{13}C$ and $\delta^{15}N$ isoscapes indicate that these baseline maps can serve as reliable spatial tracers for studying animal movement, food web structure, and nutrient sourcing. Critically, our isoscapes span the full estuarine gradient—including marine habitats typically excluded from past studies—thereby

expanding the spatial resolution available to researchers. This advancement directly addresses challenges highlighted in previous work. For example, earlier studies (e.g., Cloern et al., 2002) noted high variability in $\delta^{13}C$ and $\delta^{15}N$ among organic matter sources, complicating the use of isotopes as ecological tracers. Our spatially explicit isoscapes help resolve that variability, offering a framework for interpreting isotopic data in context. Likewise, food web studies and nutrient tracing efforts that focused on localized estuary regions (e.g., Schroeter et al., 2015) can now be extended into the North, Central, and South Bays, as well as fully marine habitat using these isoscapes. This creates new opportunities to infer habitat use, organic matter sourcing, and trophic interactions in mobile organisms like fish, birds, and invertebrates across the estuary. Given ongoing changes in freshwater flow regimes and nutrient loading in the SFBE, continued monitoring and refinement of these isoscapes will be essential for tracking ecosystem responses to climate change, land use, and management actions. As spatial baselines, these isoscapes provide a powerful tool to integrate biogeochemical and ecological data across space and time.

2.5 Conclusion

This study provides the first detailed $\delta^{13}C$ and $\delta^{15}N$ isoscapes for the SFBE, revealing how spatial and biogeochemical gradients shape isotope variability across a dynamic estuarine-to-coastal continuum. Our findings demonstrate that predictable hydrodynamic forces, nutrient loading, and source mixing govern the spatial distribution of carbon and nitrogen isotopes in this complex system. The strong performance of our models underscores the utility of isoscapes as tools for tracking nutrient dynamics, identifying carbon sources, and interpreting animal movement and trophic ecology. Moreover, the extension of coastal isotope gradients into the estuary highlights the interconnectedness of marine and estuarine processes. As environmental conditions in the SFBE continue to shift due to climate change and anthropogenic pressures, these isoscapes offer a valuable baseline and a flexible framework for ongoing ecological monitoring and management.

2.6 References

Bartoń, K. (2023). MuMIn: Multi-Model Inference (1.47.5). The Comprehensive R Archive Network.

Bowen, G. J. (2010). Isoscapes: Spatial pattern in isotopic biogeochemistry. Annual Review of Earth and Planetary Sciences, 38, 161–187. https://doi.org/10.1146/annurev-earth-040809-152429

Brugnoli, E., & Farquhar, G. D. (2000). Photosynthetic Fractionation of Carbon Isotopes.

Christensen, P. B., Nielsen, L. P., Revsbech, N. P., & S□rensen, J. (1989). Microzonation of denitrification activity in stream sediments as studied with a combined oxygen and nitrous oxide microsensor. Applied and Environmental Microbiology, 55(5), 1234–1241. https://doi.org/10.1128/aem.55.5.1234-1241.1989

Cloern, J. E., Canuel, E. A., & Harris, D. (2002). Stable carbon and nitrogen isotope composition of aquatic and terrestrial plants of the San Francisco Bay estuarine system.

Limnology and Oceanography, 47(3), 713–729. https://doi.org/10.4319/lo.2002.47.3.0713

DeNiro, M. J., & Epstein, S. (1978). Influence of diet on the distribution of carbon isotopes in animals. Geochemica et Cosmochimica Acta, 42, 495–506. https://doi.org/10.1002/mop.25285

Diaz, R. J., & Rosenberg, R. (2008). Spreading dead zones and consequences for marine ecosystems. Science, 321(5891), 926–929. https://doi.org/10.1126/science.1156401

Fackrell, J. K., Kraus, T. E. C., Young, M. B., Kendall, C., & Peek, S. (2022). Stable isotopes provide insight into sources and cycling of N compounds in the Sacramento-San Joaquin Delta, California, USA. Science of the Total Environment, 816, 151592. https://doi.org/10.1016/j.scitotenv.2021.151592

Farquhar, G. D., Ehleringer, J. R., & Hubick, K. T. (1989). Carbon Isotope Discrimination And Photosynthesis. Annual Review of Plant Physiology and Plant Molecular Biology, 40(1), 503–537.

Fry, B. (2006). Stable Isotope Ecology (521st ed.). Springer.

Goranov, A. I., Carter, S. J., Pearson, A., & Hatcher, P. G. (2025). Oxidation camouflages terrestrial organic matter to appear marine-like. Environmental Science and Technology, 59, 5607–5620. https://doi.org/10.1021/acs.est.4c12913

Graham, B. S., Koch, P. L., Newsome, S. D., McMahon, K. W., & Aurioles, D. (2010). Using isoscapes to trace the movements and foraging behavior of top predators in oceanic ecosystems. In Isoscapes: Understanding Movement, Pattern, and Process on Earth Through Isotope Mapping (pp. 299–318). https://doi.org/10.1007/978-90-481-3354-3

Granger, J., Sigman, D. M., Lehmann, M. F., & Tortell, P. D. (2008). Nitrogen and oxygen isotope fractionation during dissimilatory nitrate reduction by denitrifying bacteria. Limnology and Oceanography, 53(6), 2533–2545. https://doi.org/10.4319/lo.2008.53.6.2533

Hartig, F. (2022). DHARMa: Residual Diagnostics for Hierarchical (Multi-Level / Mixed) Regression Models. http://florianhartig.github.io/DHARMa/

Howe, E. R., & Simenstad, C. A. (2011). Isotopic Determination of Food Web Origins in Restoring and Ancient Estuarine Wetlands of the San Francisco Bay and Delta. Estuaries and Coasts, 34(3), 597–617. https://doi.org/10.1007/s12237-011-9376-8

Kendall, C., Young, M. B., Silva, S. R., Kraus, T. E. C., Peek, S., & Guerin, M. (2015). Tracing nutrient and organic matter sources and biogeochemical processes in the Sacramento River and Northern Delta: proof of concept using stable isotope data.

Lehman, P. W., Kendall, C., Guerin, M. A., Young, M. B., Silva, S. R., Boyer, G. L., & Teh, S. J. (2015). Characterization of the Microcystis bloom and its nitrogen supply in San Francisco Estuary using stable isotopes. Estuaries and Coasts, 38(1), 165–178. https://doi.org/10.1007/s12237-014-9811-8

Mariotti, A., Germon, J. C., Hubert, P., Kaiser, P., Letolle, R., Tardieux, A., & Tardieux, P. (1981). Experimental determination of nitrogen kinetic isotope fractionation: Some

principles; illustration for the denitrification and nitrification processes. Plant and Soil, 62(3), 413–430. https://doi.org/10.1007/BF02374138

McClelland, J. W., Valiela, I., & Michener, R. H. (1997). Nitrogen-stable isotope signatures in estuarine food webs: A record of increasing urbanization in coastal watersheds. Limnology and Oceanography, 42(5 I), 930–937. https://doi.org/10.4319/lo.1997.42.5.0930

Post, D. M. (2002). Using stable isotopes to estimate trophic position: Models, methods, and assumptions. Ecology, 83(3), 703–718. https://doi.org/10.1890/0012-9658(2002)083[0703:USITET]2.0.CO;2

R Core Team. (2023). R: A Language and Environment for Statistical Computing. https://www.r-project.org/

Raven, J. A., Johnston, A. M., Kübler, J. E., Korb, R., Mcinroy, S. G., Handley, L. L., & Scrimgeour, Charlie M Walker, D. I. (2002). Mechanistic interpretation of carbon isotope discrimination by marine macroalgae and seagrasses. Functional Plant Biology, 29, 255–378.

Schroeter, R. E., O'Rear, T. A., Young, M. J., & Moyle, P. B. (2015). The aquatic trophic ecology of Suisun Marsh, San Francisco Estuary, California, during autumn in a wet year. San Francisco Estuary and Watershed Science, 13(3). https://doi.org/10.15447/sfews.2015v13iss3art6

Simenstad, C. a, & Wissmar, R. C. (1985). δ13C evidence of the origins and fates of organic carbon in estuarine and nearshore food webs. Marine Ecology, 22, 141–152.

Vokhshoori, N. L., & Mccarthy, M. D. (2014). Compound-Specific d 15 N Amino Acid Measurements in Littoral Mussels in the California Upwelling Ecosystem : A New Approach to Generating Baseline d 15 N Isoscapes for Coastal Ecosystems. 9(6). https://doi.org/10.1371/journal.pone.0098087

Wankel, S. D., Kendall, C., Francis, C. A., & Paytan, A. (2006). Nitrogen sources and cycling in the San Francisco Bay estuary: A nitrate dual isotopic composition approach. Limnology and Oceanography, 51(4), 1654–1664. https://doi.org/10.4319/lo.2006.51.4.1654

Wood, S. N. (2017). Generalized Additive Models: An Introduction with R (2nd ed.). Chapman and Hall/CRC.

Znachor, P., & Nedoma, J. (2010). Importance of dissolved organic carbon for phytoplankton nutrition in a eutrophic reservoir. Journal of Plankton Research, 32(3), 367–376. https://doi.org/10.1093/plankt/fbp129

2.7 Tables

Table 2.1: Generalized Additive Model (GAM) selection for $\delta^{13}C$ isoscape.

GAM Smooth Term	AICc	RMSE	MAE
Salinity*	68.8	0.6	0.5
Latitude, Longitude	70.4	0.7	0.6

GAM Smooth Term	AICc	RMSE	MAE
NH_4^+	103.7	5.2	5.0
Total Depth	103.8	1.4	1.1
Total Oxygen	108.0	1.7	1.2
PO_4^{3-}	108.1	4.7	4.5
NO_3^-	111.9	1.6	1.1

Note: Model selection was assessed using the corrected Akaike Information Criterion (AICc) for GAMs fitted with a maximum likelihood estimator to determine model of best fit (*), along with root mean square error (RMSE) and mean absolute error (MAE) to evaluate model performance.

Table 2.2: Generalized Additive Model (GAM) selection for $\delta^{15}N$ isoscape.

GAM Smooth Term	AICc	RMSE	MAE
Latitude, Longitude*	53.0	0.7	0.5
NH_4^+	85.2	1.6	1.3
PO_4^{3-}	87.2	1.6	1.3
Total Oxygen	95.0	1.4	1.1
Salinity	96.5	1.2	1.0
NO_3^-	97.0	1.9	1.5
Total Depth	105.1	1.4	1.1

Note: Model selection was assessed using the corrected Akaike Information Criterion (AICc) for GAMs fitted with a maximum likelihood estimator to determine model of best fit (*), along with root mean square error (RMSE) and mean absolute error (MAE) to evaluate model performance.

2.8 Figures

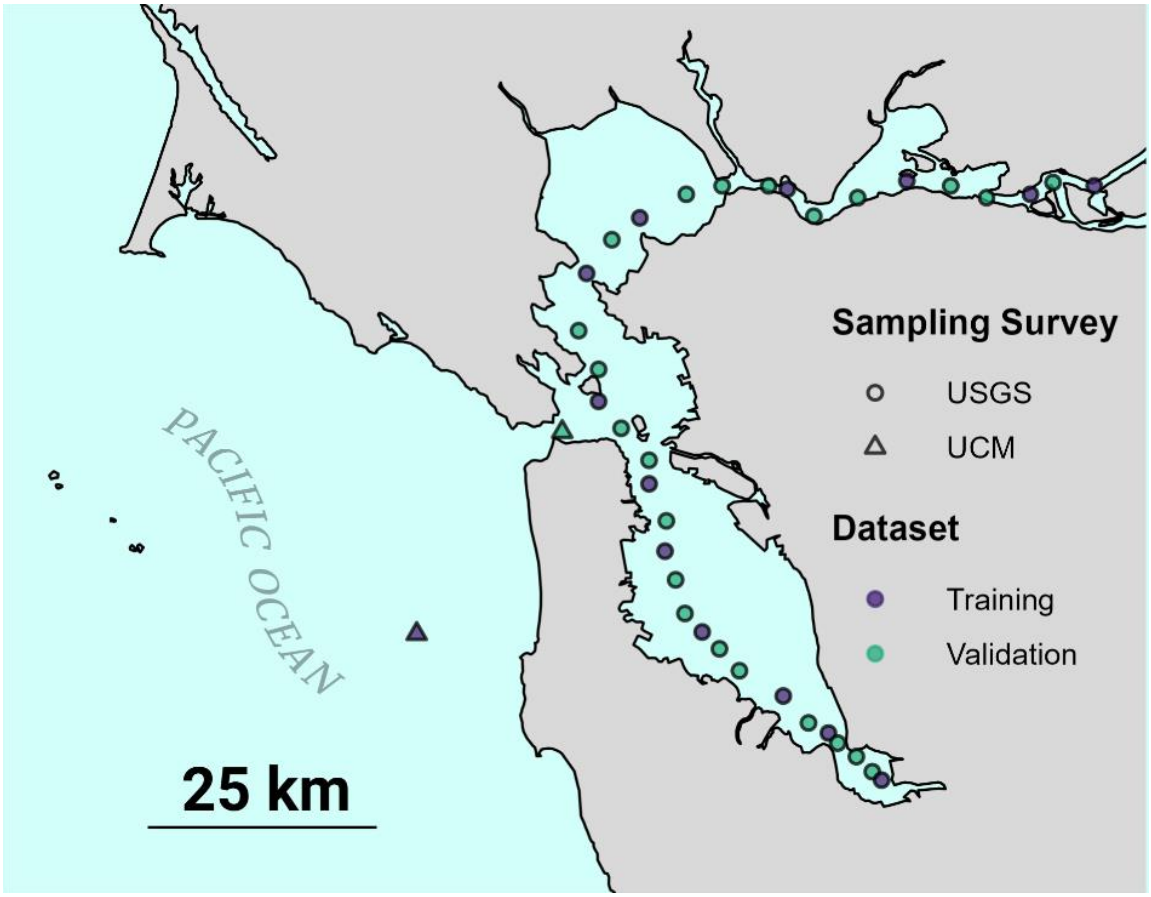

Figure 2.1: Particulate organic matter (POM) sampling sites of the San Francisco Bay Estuary. Circles indicate sampling locations from the US Geological Survey sites, while triangles indicate sampling locations from the University of California, Merced (UCM) for this study specifically. Purple symbols represent data points that were used to train generalized additive models (GAMs), while green symbols were data points used to validate the GAMs.

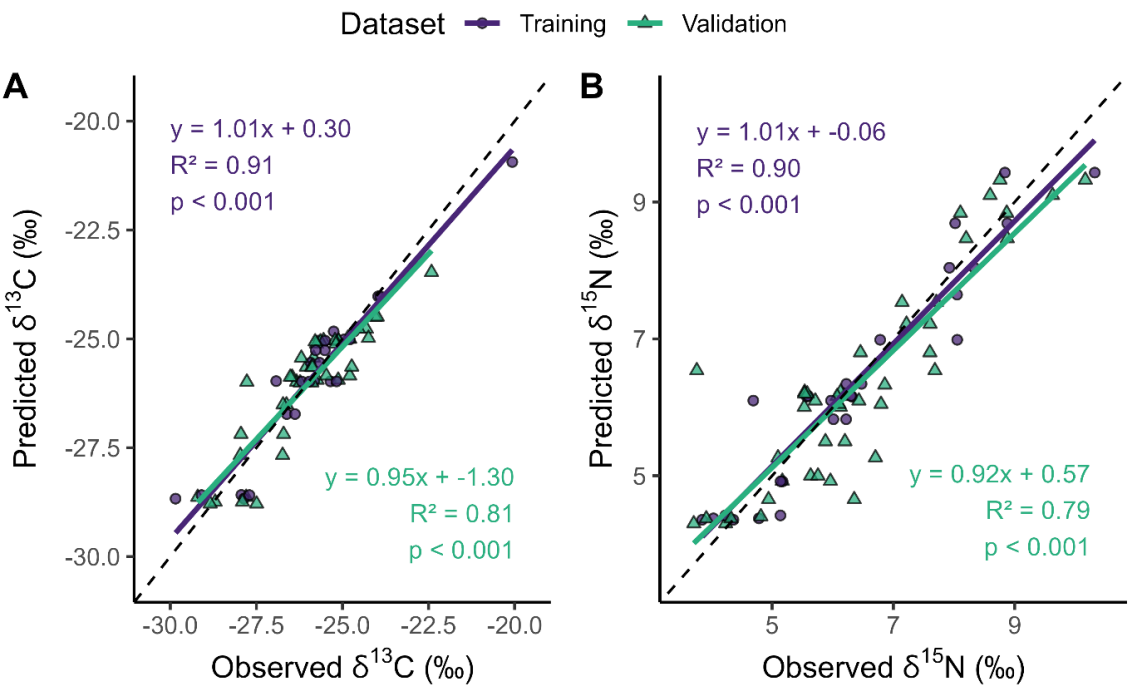

Figure 2.2: Linear relationship between observed and generalized additive model (GAM) predicted (A) $\delta^{13}C$ and (B) $\delta^{15}N$ values. Purple circles and lines indicate the dataset that GAMs were trained on, while green triangles and lines indicate the dataset that GAMs were validated on. Black dotted line is 1:1 line.

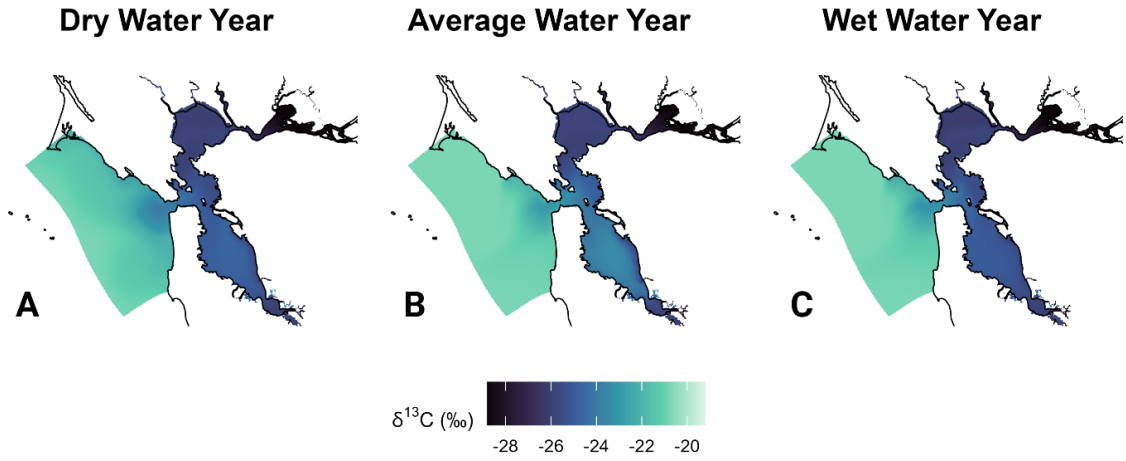

Figure 2.3: Annual $\delta^{13}C$ isoscapes of particulate organic matter in the San Francisco Bay Estuary across different hydrological conditions. (A) Dry water year (2013, SFEI model), (B) Average water year (2017, SFE model), and (C) Wet water year (2018, SFEI model). Colors represent the gradient of $\delta^{13}C$ values, reflecting spatial variability in carbon sources and biogeochemical processes across the estuary.

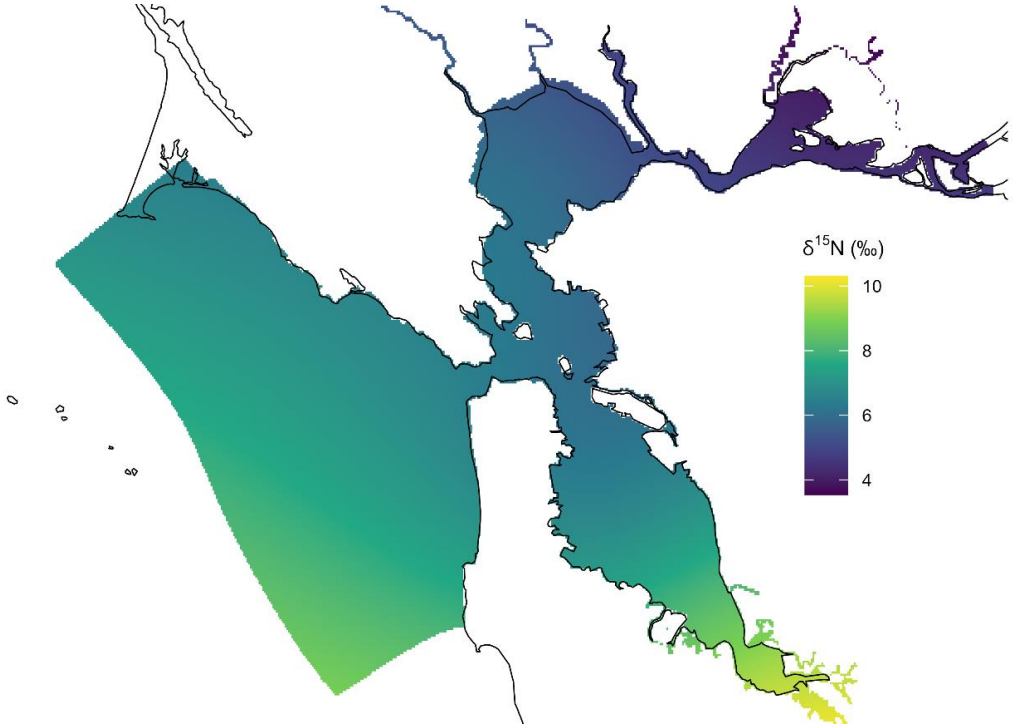

Figure 2.4: The $\delta^{15}N$ isoscape of particulate organic matter in the San Francisco Bay Estuary for water year 2024. Colors represent the gradient of $\delta^{15}N$ values, reflecting spatial variability in nitrogen sources and biogeochemical processes across the estuary.

3. Chapter 2: Leopard Shark (*Triakis semifasciata*) habitat use and foraging ecology based on multiple stable isotope approaches

3.1 Introduction:

The Leopard Shark (*Triakis semifasciata*) is an opportunistic mesopredator with a broad distribution along the Pacific coast of North America. It inhabits a variety of nearshore environments in coastal waters (Ebert, 2003; Ebert & Ebert, 2005), where it exhibits behavioral plasticity in response to shifting environmental conditions (Ackerman et al., 2000; Carlisle & Starr, 2010; Hopkins & Cech, 2003). Large aggregations are commonly observed (Hughes et al., 2014; Nosal et al., 2013, 2014; Smith, 2005) with both residential and seasonal migratory behaviors (Carlisle & Starr, 2009; Smith, 2001). Despite these observations, significant knowledge gaps remain regarding Leopard Shark life history, particularly how foraging strategies and seasonal movements vary within and among estuarine aggregations.

Leopard Sharks along California's coastline are divided into two genetically distinct populations, separated by Point Conception (Barker et al., 2015). Within the Northern genetic population, which spans Central to Northern California's coast, bays and estuaries play a critical role as foraging, gestating, pupping, and juvenile habitats (Carlisle & Starr, 2009; Cooper, 2022; Ebert, 2003; Ebert & Ebert, 2005; Hight & Lowe, 2007; Hughes et al., 2014). Patterns of genetic connectivity suggest complex population structure, with the two most geographically distant estuarine subpopulations—Humboldt Bay (North) and Elkhorn Slough (South)—having significant genetic divergence, indicating limited gene flow between them (Barker et al., 2015). In contrast, the San Francisco Estuary appears genetically similar to both, potentially serving as a transition zone that facilitates gene flow within this population (Barker et al., 2015). These patterns indicate that different populations—or even subpopulations within the Northern genetic group—may experience distinct ecological conditions that shape their foraging strategies, habitat use, and seasonal movements. Evidence suggests that subpopulations within this northern genetic population exhibit distinct life history strategies (Kuntz et al. in review), further emphasizing the need to consider fine-scale ecological variation.

While population-level differences provide insight into broader ecological patterns, less work has focused on how individual variation contributes to ecological dynamics. Beyond genetic and regional variation, recognizing differences in foraging and movement strategies at the individual level offers a deeper understanding of a species' adaptability to environmental stochasticity (Dulvy et al. 2008; Chin et al. 2010; Simpfendorfer et al. 2011). These behaviors, often explained by species-wide or population-level constraints such as gape size or temperature tolerance, can vary among individuals. Some exhibit generalist foraging strategies, while others specialize on

particular prey or habitats (Kim et al., 2012; Munroe et al., 2014). This spectrum of dietary variation underscores the need to consider individual-level variation when assessing the ecological role of Leopard Sharks across their range. Understanding how environmental conditions influence these differences is key to assessing the species' ecological resilience and adaptability.

Stable isotope analysis (SIA) of bulk tissue (i.e., whole tissue) has greatly advanced our understanding of shark ecological interactions. The stable isotope composition of carbon and nitrogen ($\delta^{13}C$ and $\delta^{15}N$) provides insights into foraging and movement ecology of sharks. Within ecosystems, $\delta^{13}C$ and $\delta^{15}N$ values reflect nutrient cycling and primary production at the food web's base. Baseline isotopic signatures propagate through the food web, but metabolic fractionation alters isotopic ratios at each trophic step due to differentiation between heavy and light isotope (e.g., $^{13}C/^{12}C$ and $^{15}N/^{14}N$) (DeNiro & Epstein, 1978; Post, 2002). This interplay between baseline and trophic isotope variation makes bulk isotope data a powerful yet generalized approach for inferring trophic and movement ecology, particularly in highly mobile species.

In contrast, compound-specific isotope analysis of amino acids (CSIA-AA) deconvolves a bulk tissue and provides a more precise tool for characterizing food web structure and function. The $\delta^{13}C$ values of essential amino acids (AAEss) provide a 'fingerprint' to distinguish primary production sources (e.g., phytoplankton, macroalgae, and plants) due to unique biosynthetic pathways and minimal trophic discrimination (Larsen et al., 2013; Vane et al., 2025). Meanwhile, $\delta^{15}N_{AA}$ values differentiate 'source' AAs (e.g., phenylalanine), which retain baseline nitrogen isotope signals, from 'trophic' AAs (e.g., glutamic acid), which become ^{15}N-enriched with each trophic transfer. The differentiation between trophic and source AAs $\delta^{15}N$ values provides an accurate estimate of trophic position, independent of baseline nitrogen isotope variation. While CSIA-AA allows for more precise investigations of food web structure and individual foraging strategies, its application to studying individual variation remains limited due to the high cost of analysis.

Understanding both population- and individual-level variation is essential for assessing ecological resilience, as species with diverse foraging strategies and movement patterns may be more adaptable to environmental change. In this study, we use CSIA-AA to investigate the trophic ecology and movement dynamics of Leopard Shark subpopulations in Central California. Specifically, we ask: (1) What basal resources support these subpopulations? (2) Do subpopulations differ in trophic ecology? (3) How does total niche width vary among subpopulations, and how does this relate to residency and transience of individuals? (4) What are the seasonal patterns in movement and foraging ecology across populations and individuals? By integrating these ecological dimensions, we aim to refine our understanding of Leopard Shark resilience and the factors shaping their foraging and movement strategies in dynamic coastal ecosystems.

3.2 Methods:

3.2.1 Sampling:

We collected sub-adult and adult Leopard Sharks from four sites—San Francisco Estuary (SFE; n = 9), Drakes Estero State Marine Conservation Area (Drakes Estero SMCA; n = 10), Tomales Bay (n = 10), and Bodega Bay (n = 9)—using hook and line, gill nets, and salvage donations from fishers (Fig. 3.1). Sharks were caught and euthanized following approved protocols (University of California Merced IACUC: #AUP20-0013; California Department of Fish & Wildlife permits: S-201820001-20182-001 and S-201840003-20196-001; National Park Service permit: #PORE-2020-SCI-0017) and transported on ice to UC Merced for dissection and analysis.

A muscle tissue sample was taken, followed by lipid and urea extraction using protocols from Kim & Koch (2012). Additionally, sequential teeth series were dissected from the lower jaw. Each tooth file (vertical column) in the jaw contained six to seven series (horizontal rows) of teeth. Because Leopard Shark tooth replacement occurs approximately every 55 days per series in a single file for adults (Zeichner et al., 2017), we back-calculated the day-of-year for each tooth series and assigned day-of-year for each series based on the individual's catch date. To account for small sample sizes and ensure consistency for SIA, teeth from the same series in the 2nd, 4th, 6th, and 8th files were pooled before demineralization with 0.1 M HCl for 24 hours following Trayler et al. (2023). Lipid and urea-extracted muscle samples and demineralized teeth samples were subsequently frozen for at least eight hours before lyophilization. Once fully dried, muscle samples were weighed and prepared for bulk SIA and CSIA-AA, while teeth dentin samples were weighed and prepared for only bulk SIA.

3.2.2 Stable Isotope Analysis

We analyzed $\delta^{13}C_{Bulk}$ and $\delta^{15}N_{Bulk}$ values in lipid and urea extracted muscle tissue, as well as tooth dentin at UC Merced's Stable Isotope Ecosystem Laboratory (SIELO) using an Elemental Analyzer coupled to a continuous-flow Isotope Ratio Mass Spectrometer with a conflo IV (EA-cf-IRMS). Stable isotope values are reported in delta notation (δ, ‰), with $\delta^{13}C$ referenced to Vienna Pee Dee Belemnite (VPDB) and $\delta^{15}N$ to V-AIR. Data were corrected for linearity and drift as well as normalized using calibrated reference materials (USGS 40: $\delta^{13}C_{Bulk}$ = -26.4 ± 0.2 ‰, $\delta^{15}N_{Bulk}$ = -4.5 ± 0.1 ‰, n = 39; USGS 41a: $\delta^{13}C_{Bulk}$ = 36.5 ± 0.2 ‰, $\delta^{15}N_{Bulk}$ = 47.5 ± 0.1 ‰, n = 23) and verified with an internal standard (Mb Squid: $\delta^{13}C_{Bulk}$ = -18.8 ± 0.1 ‰, $\delta^{15}N_{Bulk}$ = 12.0 ± 0.2 ‰, n = 13).

We used linear regression models (LMs) to investigate the correlation between bulk muscle and bulk teeth stable isotope values ($\delta^{13}C_{Bulk}$ and $\delta^{15}N_{Bulk}$), while Bayesian generalized linear mixed models (GLMMs) were applied to teeth data to assess total niche width (TNW) and individual contributions within each region. we applied LMs using the *stats* package (R Core Team, 2023). For teeth data specifically, we used a bivariate Bayesian GLMM from the *MCMCglmm* package (Hadfield, 2010). Each Bayesian GLMM included a random effect structure with unstructured covariance to account for between-individual variation (BIC) and residual covariance to model the relationship between isotopic dimensions, capturing within-individual variation (WIC).

Subpopulation 95% confidence interval ellipses were generated from the posterior covariance matrices to model regional ellipses using teeth isotope values. Each model incorporated a random effect structure with unstructured covariance to account for between-individual variation (BIC) and residual covariance to capture within-individual variation (WIC) across isotopic dimensions. Subpopulation 95% confidence interval ellipses were derived from the posterior covariance matrices. To assess individual contributions to the total niche width (TNW) within each region, we first ran the Bayesian GLMM for the entire subpopulation. We then sequentially removed one individual at a time, rerunning the model, replacing the individual, and repeating this process for each individual in each region, following the methods outlined by Garrido-de León et al. (2024).

To analyze non-linear seasonal variation in stable isotope values over time, we implemented hierarchical generalized additive models (HGAMs) with a cyclic cubic spline using the *mgcv* package (Wood, 2017). We followed Pedersen et al. (2019) with a 'GI' structured HGAM, using stable isotope values as the response variable and age as a global smoother. We included group-level smoothers of age by region, as well as region- and Fish ID-specific intercepts as random smooth effects to account for regional and individual variation. Model assumptions were validated using the *DHARMa* package (Hartig, 2022).

3.2.3 Compound Specific Stable Isotope Analysis of Amino Acids

Following lipid extraction, muscle tissue underwent acid hydrolysis in 6 M HCl at 150°C for 70 minutes under a nitrogen headspace. The resulting amino acids were derivatized as N-acetyl methyl esters (NACME; Corr et al., 2007) and analyzed using a Gas Chromatography Combustion Isotope Ratio Mass Spectrometer (GC-C-IRMS) at the University of California Davis Stable Isotope Facility. Separation was achieved with an Agilent DB-35 column (60 m, 0.32 mm, 1.5 μm). Stable isotope values were quantified for a suite of amino acids, including alanine (Ala), aspartic acid and asparagine (Asx), glutamic acid and glutamine (Glx), glycine (Gly), isoleucine (Ile), leucine (Leu), lysine (Lys), methionine (Met), phenylalanine (Phe), proline (Pro), threonine (Thr), and valine (Val). Calibration, scale normalization, and quality control adhered to Yarnes & Herszage (2017). Analytical precision was assessed through duplicate or triplicate analyses, depending on measurement variability. Across all amino acids, mean standard deviations for $\delta^{13}C$ were ± 0.1 ‰ for replicate samples and ± 0.3 ‰ for reference materials, while $\delta^{15}N$ values had standard deviations of ± 0.3 ‰ and ± 0.6 ‰, respectively.

3.2.3.1 CSIA-AA Fingerprinting

To characterize basal resources utilization by Leopard Sharks, we used essential $\delta^{13}C_{AA}$ fingerprinting following the approach of Larsen et al. (2013). We first compiled an ecosystem-specific library of previously published essential $\delta^{13}C_{AA}$ values for primary producers (Supplemental 3.8.1, Table 3.1), including phytoplankton (Pacific Ocean, California; n = 39; Stahl et al., 2023), macroalgae (California coastline; n = 21; Larsen et al., 2013), and plants (California coastline and San Francisco Estuary; n = 47; Larsen et al., 2013; Tipple et al., 2021). We then established $\delta^{13}C_{AA}$ 'fingerprints' using Linear Discriminant Analysis (LDA), training the model on this compiled basal resource library.

Although essential $\delta^{13}C_{AA}$ values undergo minimal transformation from basal resources to consumer tissues, recent studies suggest that gut microbiome synthesis of essential AAs can contribute to isotopic fractionation, potentially skewing predictive assignments(Larsen et al., 2009; Mcmahon et al., 2010). To date, no studies have incorporated microbial contributions to essential $\delta^{13}C_{AA}$ fingerprinting a priori. Therefore, before integrating Leopard Shark $\delta^{13}C_{AA}$ values into the LDA, we accounted for potential microbial influences by applying AA-specific trophic discrimination factors (TDFs) derived from a long-term Leopard Shark feeding experiment (unpublished TDFs, Supplemental 3.8.2; Whiteman et al., 2018). These TDFs adjusted $\delta^{13}C_{AA}$ values to better represent basal resource assimilation. To incorporate natural variability when accounting for individual AA TDFs, we implemented a bootstrapping approach, generating 10 resampled $\delta^{13}C_{AA}$ values per individual. Each bootstrapped value was adjusted by subtracting the corresponding TDF and incorporating a randomly generated value from a normal distribution, scaled by its standard deviation to account for measurement uncertainty in downstream analyses. Finally, to visualize basal resource use within niche space, we modeled regional ellipses using a bivariate Bayesian GLMM, with subpopulation ellipses generated from the posterior covariance matrices.

3.2.3.2 CSIA-AA Trophic Position

We used CSIA-AA δ15N values to calculate trophic position independent of baseline variation, following Chikaraishi et al. (2009):

$$Trophic\ Position = TP_{Glx/Phe} = \frac{\delta^{15}N_{Glx} - \delta^{15}N_{Phe} - \beta}{TDF_{Glx-Phe}} + 1, \textbf{(\textit{Equation 3.1})}$$

where $\delta^{15}N_{Phe}$ (source amino acid) and $\delta^{15}N_{Glx}$ (trophic amino acid) were measured, β represents the $\delta^{15}N$ offset from Phe to Glx in the primary producer (3.3 ‰; Ramirez et al., 2021), and $TDF_{Glx\text{-}Phe}$ is the $\delta^{15}N$ offset between diet and consumer for the trophic amino acid (7.6 ‰; Chikaraishi et al., 2009). Although lower TDFs have been explored for Leopard Sharks specifically (e.g., 2.6–3.2 ‰; Hoen et al., 2014; Whiteman et al., 2018, unpublished) but when applied to our data, these values resulted in trophic position estimates that exceeded ecologically plausible limits (see Supplemental 3.8.3). Additional captive feeding studies in other fishes (e.g., Atlantic killifish) highlight how TDFs can vary widely depending on diet quality, with values ranging from 5.1–10.4 ‰ (Mcmahon et al., 2015). Given this variability and the risk of biologically unrealistic estimates, we applied the original 7.6‰ TDF to avoid overestimation of trophic position and maintain consistency with the established framework. We conducted all statistical analyses using R version 4.3.1 (R Core Team, 2023).

3.3 Results

3.3.1 CSIA-AA Fingerprinting

Basal resource utilization by Leopard Sharks, as inferred from $\delta^{13}C$ fingerprinting, revealed distinct isotopic signatures corresponding to primary producer endmembers. The Linear Discriminant Analysis (LDA) successfully classified $\delta^{13}C$ values, with posterior probabilities indicating strong separation among phytoplankton, macroalgae, and plant-derived sources. The classification model performed well, with

high precision (≥ 0.80) and recall (≥ 0.90) across all categories, achieving the highest accuracy for plant-derived carbon sources (F-score = 0.98), followed by phytoplankton (F-score = 0.92) and macroalgae (F-score = 0.87). Misclassifications were minimal, with only a few phytoplankton samples classified as macroalgae and vice versa, supporting the robustness of the model in distinguishing among basal resources.

Prior to applying amino acid–specific TDFs, all Leopard Sharks across sites were uniformly classified as relying exclusively on phytoplankton (see Supplemental 3.8.2). However, after accounting for gut microbial contributions to $\delta^{13}C$ values using AA-specific TDFs, regional differences in basal resource assimilation emerged. Leopard Sharks still relied most heavily on phytoplankton across all sites, but contributions from macroalgae and plant-derived carbon varied by region. Bodega Bay Leopard Sharks showed the highest reliance on phytoplankton (87.5%), with 12.5% classified as utilizing macroalgae and 0% as relying on plant-derived carbon. Similarly, Drakes Estero SMCA exhibited 0% plant classifications, with 74.0% of individuals classified as phytoplankton-based and 26.0% associated with macroalgae. In contrast, Leopard Sharks in the San Francisco Estuary exhibited more diverse basal resource use, with 64.4% classified as phytoplankton-reliant, 32.2% as plant-derived carbon users, and 3.3% as macroalgae users. Tomales Bay Leopard Sharks showed the second highest reliance on phytoplankton (78.0%), with 15.0% classified as plant-derived carbon users and 7.0% associated with macroalgae.

Bayesian GLMM quantified regional variation in isotopic discrimination, revealing distinct spatial patterns. In all four regional models, fixed effects indicated significant differences in LD1 and LD2 scores (pMCMC < 0.001 for both). Total niche width (TNW) in LDA space varied among regions, with Drakes Estero exhibiting the highest TNW (0.54), followed by Bodega Bay (0.48), San Francisco Estuary (0.47), and Tomales Bay (0.42). Variance in LDA scores was partitioned at both the individual (G-structure) and residual (R-structure) levels. Sharks in Bodega Bay and Drakes Estero had higher LD2 values, reflecting stronger reliance on macroalgae, while those in Tomales Bay and the San Francisco Estuary had higher LD1 values, indicating more reliance on plant-derived carbon (Fig. 3.2).

3.3.2 CSIA-AA Source and Trophic

Mean $\delta^{15}N$ values of the source amino acid phenylalanine (Phe) varied across regions (Fig. 3.3A), with the San Francisco Estuary exhibiting a mean of 10.3 ± 1.4 ‰, the widest standard deviation among all sites. Drakes Estero had the highest mean source $\delta^{15}N$ at 10.6 ± 0.6 ‰, while Tomales Bay exhibited a slightly lower mean of 10.1 ± 0.7 ‰. Bodega Bay had the lowest mean source $\delta^{15}N$ at 9.7 ± 0.8 ‰. Trophic position, quantified with source and trophic AAs, also varied regionally (Fig. 3.3B), with the San Francisco Estuary exhibiting the highest mean at 3.3 ± 0.3. Drakes Estero had a mean trophic position of 3.2 ± 0.1, showing the lowest standard deviation among regions. Similarly, Bodega Bay had a trophic position of 3.2 ± 0.2. Finally, Tomales Bay had the lowest mean trophic position of 3.0 ± 0.3.

3.3.3 Muscle to Teeth Comparison

To test the assumption that muscle and teeth series represent similar isotopic timescales, we utilized simple linear models for both bulk $\delta^{13}C$ and $\delta^{15}N$. We found muscle $\delta^{13}C$ values to be strongly correlated with mean teeth $\delta^{13}C$ values ($R^2 = 0.89$, $p < 0.001$; Fig. 3.4A). Similarly, muscle $\delta^{15}N$ values were significantly and positively correlated with mean teeth $\delta^{15}N$ values ($R^2 = 0.74$, $p < 0.001$; Fig. 3.4B). This indicates consistency in isotopic incorporation between tissue types.

3.3.4 Bayesian GLMM

We used Bayesian bivariate mixed-effects models to assess variation in Leopard Shark tooth dentin $\delta^{13}C$ and $\delta^{15}N$ values across four regions, revealing differences in isotopic niche width and overlap among regions (Fig. 3.5A). In all four regional models, both $\delta^{13}C$ and $\delta^{15}N$ exhibited significant fixed effects (pMCMC < 0.001 for both isotope systems). We found that TNW varied among regions, with Drakes Estero exhibiting the broadest TNW (4.2), followed by the San Francisco Estuary (3.9), Tomales Bay (2.9), and Bodega Bay (2.8). Regional ellipses displayed varying degrees of niche overlap, reflecting differences in movement and foraging strategies. Quantifying each individual's contribution to its region's TNW revealed that contributions were highly unequal (Fig. 3.5B)—only a few individuals expanded their region's TNW, while the inclusion of most individuals actually reduced it (Fig 3.5C). This pattern suggests that a small subset of individuals plays a disproportionate role in broadening the overall locality's niche .

3.3.5 Dental Series represent seasonal variation

Seasonal $\delta^{13}C$ and $\delta^{15}N$ patterns from Leopard Shark tooth stable isotope composition reveal regional differences in isotopic variability across Central California. The $\delta^{13}C$ HGAM explained a substantial portion of the variance ($R^2 = 0.87$) and showed a significant seasonal trend across all regions, with $\delta^{13}C$ values reaching a trough from summer into fall ($p = 0.02$; Fig. 3.6). Among individual regions, only Drake's Estero exhibited a significant $\delta^{13}C$ trend across the year ($p = 0.001$), while other localities showed some seasonal variability, though non-significant (Fig. 3.6A,B). The $\delta^{15}N$ HGAM ($R^2 = 0.74$) showed no significant global seasonal trend ($p = 0.60$), but $\delta^{15}N$ values in the San Francisco Estuary exhibited a significant seasonal peak during summer ($p < 0.001$), whereas other regions showed no clear seasonal pattern (Fig. 3.6C,D). Random smooth effects for both models suggest regional differences played a key role in shaping seasonal isotopic trends ($\delta^{13}C$: $p < 0.001$; $\delta^{15}N$: $p = 0.005$). While Fish ID was not significant in either model, the individual with the highest contribution to TNW is well outside HGAM smooth 95% confidence intervals for either $\delta^{13}C$ or $\delta^{15}N$.

3.4 Discussion

Our study demonstrates that Leopard Shark subpopulations exhibit distinct patterns of resource use, trophic positioning, seasonal movements, and individual residence versus transience, underscoring the dynamic nature of their foraging ecology across estuarine habitats. The $\delta^{13}C$ CSIA-AA revealed that while all subpopulations primarily relied on phytoplankton-derived carbon, the contributions of secondary sources varied regionally, reflecting differences in freshwater inflow and tidal dynamics. The

$\delta^{15}N$ CSIA-AA further highlighted variation in trophic structure, with the San Francisco Estuary supporting the highest trophic complexity, likely driven by anthropogenic nitrogen inputs. Seasonal isotopic patterns suggest movement into estuarine interiors during summer, while individual-level variation in $\delta^{13}C$ identified transient versus resident individuals, reinforcing the role of estuarine connectivity in shaping population structure. Collectively, these findings illustrate how environmental factors and individual movement strategies contribute to the ecological flexibility of Leopard Sharks in northern California's estuaries.

3.4.1 Basal Resources Supporting Subpopulations

Utilizing $\delta^{13}C$ CSIA-AA, we found basal resource utilization varied between subpopulations. For $\delta^{13}C$, amino acids are classified as either 'essential' or 'non-essential,' which influences the extent of isotope alteration during metabolism between a consumer and its diet. Essential amino acids cannot be synthesized by consumers and must be obtained from the diet or gut microbes; therefore, they exhibit minimal $^{13}C/^{12}C$ fractionation during protein synthesis. In contrast, non-essential amino acids can be biosynthesized from other amino acids, leading to selective retention of ^{13}C due to the preferential loss of ^{12}C along metabolic pathways, resulting in higher $\delta^{13}C$ values in non-essential amino acids (Besser et al., 2022; Mcmahon et al., 2010). Because essential amino acids are directly derived from basal resources of a given food web (e.g., plants, algae, bacteria) and generally experience minimal fractionation during metabolic routing—aside from potential modifications by the gut microbiome—they serve as reliable tracers for identifying the basal resources that support a given consumer's food web (Larsen et al., 2013; Vane et al., 2025).

Prior to accounting for the gut microbiota, all Leopard Sharks in this study were classified as having macroalgal dominated carbon sources (Supplemental 3.8.2). After accounting for gut microbiome contributions using individual amino acid TDFs, all Leopard Shark subpopulations exhibited a strong reliance on phytoplankton-derived carbon food webs, though the contributions of secondary and tertiary sources varied regionally (Fig. 3.2). In Bodega Bay and Drakes Estero—both low-inflow estuaries with minimal freshwater input—there was no classification of plant-derived carbon sources. Instead, these subpopulations relied heavily on phytoplankton, with macroalgae as a secondary source, likely subsidized by tidal fluxes transporting organic material into the system. Given the extreme tidal dynamics and small estuarine size, Leopard Sharks in these localities are likely foraging along the estuarine boundary, moving with the tides between estuarine and coastal waters.

In Tomales Bay and the San Francisco Estuary, Leopard Sharks primarily relied on phytoplankton-derived food webs, but plant-derived carbon served as a secondary resource. This pattern was especially pronounced in the San Francisco Estuary, where a third of sampled individuals were classified as plant-based carbon basal resource users. The high freshwater inflow in these systems likely drives this reliance, as it delivers terrestrial plant detritus that fuels detritivore-based food webs (Simenstad & Wissmar, 1985). Additionally, the availability of tidal refugia in these estuaries allows for prolonged residence times, further increasing exposure to C_3-derived food sources.

Notably, the San Francisco Estuary has the highest freshwater input of any estuary in California (Emmett et al., 2000), reinforcing its influence on basal resource assimilation. The variation in carbon sources among subpopulations highlights the Leopard Shark's role as a generalist mesopredator (Cortés, 1999; Ebert & Ebert, 2005), an adaptation that supports their persistence across dynamic habitats, from brackish estuarine waters to coastal marine environments.

3.4.2 Baseline and Trophic Patterns of Subpopulations

Leopard Shark subpopulations exhibited varying baseline and trophic positions, regardless of baseline trends between localities. For $\delta^{15}N$, amino acids are categorized based on isotopic fractionation during deamination and transamination reactions. 'Source' amino acids do not undergo these metabolic processes, meaning their amine group remains intact with minimal alteration and resulting in little to no fractionation. As a result, source amino acids (*e.g.*, Phe) preserve baseline $\delta^{15}N$ values and directly reflect nitrogen sources such as N_2 fixation or nitrate assimilation (Chikaraishi et al., 2009). In contrast, 'trophic' amino acids experience substantial ^{15}N enrichment due to deamination and transamination, which increases $\delta^{15}N$ values by several ‰ per trophic level (Mcmahon & Mccarthy, 2016).

Regional differences in trophic position further highlight variation in food web complexity across estuaries; however, the trophic positions observed align closely with Cortés (1999) predicted trophic level of 3.7 for Leopard Sharks based on diet content analysis (Fig. 3.3), reinforcing their role as mid-to-upper level predators within estuarine food webs. The San Francisco Estuary exhibited the highest mean trophic position and largest standard deviation; given the Leopard Shark's opportunistic foraging strategy, this variation may be driven by anthropogenic nitrogen inputs supporting a more isotopically complex and heterogenous food web through increased primary production and prey diversity (Liu et al., 2018). Another possibility is that individual Leopard Sharks in this system exhibit bimodal foraging, with some specializing on higher trophic level prey and others on lower trophic level prey. Alternatively, bacterial reworking of detrital materials in the San Francisco Estuary may be resulting in $\delta^{15}N$ fractionation (McCarthy et al., 2007), inflating trophic position estimates.

This pattern of trophic variability was not uniform across all subpopulations, highlighting differences in niche diversity and food web structure among estuaries. For example, Tomales Bay's lower mean trophic position suggests a more direct energy pathway with fewer trophic transfers, potentially reflecting differences in prey availability or foraging strategies. Yet, it also exhibited the largest standard deviation in trophic position—echoing patterns seen in the San Francisco Estuary—where the broader range of available estuarine habitats, including additional tidal refugia, appears to support a wider variety of isotopic niches. The Bodega Bay subpopulation displayed intermediate trophic variability, hinting at a balance between resource specialization and flexible foraging strategies. Conversely, Leopard Sharks in Drakes Estero had the smallest standard deviation in trophic position, mirroring the low baseline variability observed in this system. This lack of variation in both baseline and trophic position suggests that

individuals in Drakes Estero are specializing on a specific resource, likely one that is consistently available in this restored marine protected area.

3.4.3 Localized Seasonal Movements Within Estuarine Subpopulations

Leopard Shark teeth have previously been used as continuous time series to determine TDFs and isotopic incorporation rates during captive feeding experiments (Zeichner et al., 2017). Teeth series have also been theorized to record seasonal isotopic patterns linked to baseline variation (Shipley et al., 2021). Using this method, we found that Leopard Sharks from different localities exhibit similar $\delta^{13}C$ patterns across the DOY (Fig. 3.6A,B), with higher values in winter, a decline in spring reaching a trough in summer, and an increase again in fall and winter. This pattern likely reflects seasonal movement into the inner estuary during the warmer summer months, a behavior observed in pregnant females that enhances gestation. In these inner estuarine areas, $\delta^{13}C$ baselines are lower due to a greater influence of C_3 plant detritus from terrestrial sources (Simenstad & Wissmar, 1985).

Meanwhile, Leopard Sharks from Bodega Bay, Tomales Bay, and Drakes Estero show relatively stable $\delta^{15}N$ trends across DOY (Fig. 3.6C,D), supporting the idea that baseline variation between coastal and estuarine waters in these systems is minimal. In contrast, $\delta^{15}N$ values in the San Francisco Estuary exhibit a distinct summer spike (Fig. 3.6C,D), likely driven by Leopard Sharks moving into areas with high anthropogenic eutrophication from wastewater treatment and prolonged residence times in the lower South San Francisco Estuary (Cloern et al., 2020; Liu et al., 2018), which elevate baseline $\delta^{15}N$ at the base of the food web (McClelland et al., 1997). Notably, this $\delta^{15}N$ increase in the San Francisco Estuary subpopulation coincides with shifts in $\delta^{13}C$ values (Fig. 3.6C,D), further reinforcing the hypothesis that Leopard Sharks migrate into the estuary's inner reaches during summer, linking seasonal movement to isotopic variation.

3.4.4 Residence vs Transience of Individuals

Understanding individual variation in resource and habitat use is essential for assessing population resilience. In this system, isotopic variation between estuarine subpopulations is primarily driven by baseline differences, shaping the overall niche space of each group (Fig. 3.5A,B). To assess individual contributions to this structure, we applied the 'Keystone niche individual' approach from Garrido-de León et al. (2024) to identify the individual with the highest contribution to its subpopulation's TNW (Fig. 3.5C). This allowed us to pinpoint individuals exhibiting the greatest niche breadth within their subpopulation, reflecting the influence of baseline variation at the individual level. Notably, in each of Bodega Bay, Tomales Bay, and Drakes Estero, the individuals with the highest contribution had $\delta^{13}C$ values consistently lower than those of others in the same locality (Fig. 3.6B). This could suggest recent movement from another location, with insufficient time for the isotopic baseline of the new environment to be incorporated into the most recently formed tooth. Given the isotopic incorporation rate for $\delta^{13}C$ in Leopard Shark teeth, movement into the novel system likely occurred within the last ~ 48 days (Zeichner et al., 2017). We classified these as transient individuals, whereas those whose isotopic values closely followed seasonal patterns and contributed minimally to the isotopic niche were considered residents. Interestingly, the individual contributing

most to the San Francisco Estuary's isotopic niche exhibited consistently higher $\delta^{15}N$ values across DOY while also having the lowest $\delta^{13}C$ values recorded in the estuary (Fig. 3.6B,D). One explanation is more time was spent in the lower reaches of the South San Francisco Estuary, where $\delta^{15}N$ values are likely elevated due to high anthropogenic nitrogen inputs and $\delta^{13}C$ values are likely the lowest due to high freshwater flow in the system supplying terrestrial C_3 detritus (McClelland et al., 1997; Simenstad & Wissmar, 1985). Collectively, these patterns of movement between estuarine systems support the metapopulation theory for Leopard Sharks in the northern population (Kuntz et al., in review), indicating connectivity among localities and potential population structuring across the region.

3.5 Conclusion

This study provides new insights into the foraging ecology of Leopard Sharks across four estuarine subpopulations in Northern California, revealing distinct regional patterns in basal resource use, trophic position, and isotopic variation. Our use of $\delta^{13}C$ CSIA-AA fingerprinting demonstrated that while all subpopulations primarily rely on phytoplankton-derived carbon, the contributions of secondary resources such as macroalgae and plant material varied significantly by region, reflecting local environmental dynamics, such as freshwater inflow and tidal influences. These findings highlight the importance of estuarine connectivity in shaping the ecological flexibility and movement patterns of Leopard Sharks. Regional differences in trophic complexity and isotopic niche width further suggest that anthropogenic factors, such as nitrogen inputs in the San Francisco Estuary, may influence the trophic structure of these sharks. The significant individual-level variation in resource use and isotopic signatures also points to the presence of both resident and transient individuals within each subpopulation, suggesting that Leopard Sharks exhibit a range of movement strategies in response to seasonal and environmental changes. Ultimately, these findings emphasize the dynamic nature of Leopard Shark ecology and the need to consider both environmental factors and individual variation when assessing their conservation and management in coastal ecosystems.

3.6 References

Ackerman, J. T., Kondratieff, M. C., Matern, S. A., & Cech, J. J. (2000). Tidal influence on spatial dynamics of leopard sharks, Triakis semifasciata, in Tomales Bay, California. Environmental Biology of Fishes, 58(1), 33–43. https://doi.org/10.1023/A:1007657019696

Barker, A. M., Nosal, A. P., Lewallen, E. A., & Burton, R. S. (2015). Genetic structure of leopard shark (Triakis semifasciata) populations along the Pacific coast of North America. Journal of Experimental Marine Biology and Ecology, 472, 151–157. https://doi.org/10.1016/j.jembe.2015.06.020

Besser, A. C., Elliott, E. A., & Newsome, S. D. (2022). Assessing the Potential of Amino Acid δ13C and δ15N Analysis in Terrestrial and Freshwater Ecosystems. Journal of Ecology, 110(January), 935–950. https://doi.org/10.1111/1365-2745.13853

Carlisle, A. B., & Starr, R. M. (2009). Habitat use, residency, and seasonal distribution of female leopard sharks Triakis semifasciata in Elkhorn Slough, California. Marine Ecology Progress Series, 380(2001), 213–228. https://doi.org/10.3354/meps07907

Carlisle, A. B., & Starr, R. M. (2010). Tidal movements of female leopard sharks (Triakis semifasciata) in Elkhorn Slough, California. Environmental Biology of Fishes, 89(1), 31–45. https://doi.org/10.1007/s10641-010-9667-0

Chikaraishi, Y., Ogawa, N. O., Kashiyama, Y., Takano, Y., Suga, H., Tomitani, A., Miyashita, H., Kitazato, H., & Ohkouchi, N. (2009). Determination of aquatic food-web structure based on compound-specific nitrogen isotopic composition of amino acids. Limnology and Oceanography: Methods, 7(NOV), 740–750. https://doi.org/10.4319/lom.2009.7.740

Cloern, J. E., Schraga, T. S., Nejad, E., & Martin, C. (2020). Nutrient status of San Francisco Bay and its management implications. Estuaries and Coasts, 43(6), 1299–1317. https://doi.org/10.1007/s12237-020-00737-w

Cooper, A. A. B. (2022). Demography , Diet , and Habitat Use of Leopard Sharks (Triakis semifasciata) in a Protected Estuarine Environment By. Sanoma State University.

Cortés, E. (1999). Standardized diet compositions and trophic levels of sharks. ICES Journal of Marine Science, 56(5), 707–717. https://doi.org/10.1006/jmsc.1999.0489

Ebert, D. A. (2003). Sharks, rays and chimaeras of California. In University of California Press, Berkely, CA.

Ebert, D. A., & Ebert, T. B. (2005). Reproduction, diet and habitat use of leopard sharks, Triakis semifasciata (Girard), in Humboldt Bay, California, USA. Marine and Freshwater Research, 56(8), 1089–1098. https://doi.org/10.1071/MF05069

Emmett, R., Llansó, R., Newton, J., Thom, R., Hornberger, M., Morgan, C., Levings, C., Copping, A., & Fishman, P. (2000). Geographic signatures of north american west coast estuaries. Estuaries and Coasts, 23(6), 765–792. https://doi.org/10.2307/1352998

Garrido-de León, F., Franco-Trecu, V., & Costa-Pereira, R. (2024). Keystone niche individuals: some are more unequal than others. Trends in Ecology and Evolution, 40(1), 14–17. https://doi.org/10.1016/j.tree.2024.11.006

Hadfield, J. D. (2010). MCMCglmm: MCMC Methods for Multi-Response GLMMs in R. Journal of Statistical Software, 33(2), 1–22. https://www.jstatsoft.org/v33/i02/

Hartig, F. (2022). DHARMa: Residual Diagnostics for Hierarchical (Multi-Level / Mixed) Regression Models. http://florianhartig.github.io/DHARMa/

Hight, B. V., & Lowe, C. G. (2007). Elevated body temperatures of adult female leopard sharks, Triakis semifasciata, while aggregating in shallow nearshore embayments: Evidence for behavioral thermoregulation? Journal of Experimental Marine Biology and Ecology, 352(1), 114–128. https://doi.org/10.1016/j.jembe.2007.07.021

Hoen, D. K., Kim, S. L., Hussey, N. E., Wallsgrove, N. J., Drazen, J. C., & Popp, B. N. (2014). Amino acid 15N trophic enrichment factors of four large carnivorous fishes.

Journal of Experimental Marine Biology and Ecology, 453, 76–83. https://doi.org/10.1016/j.jembe.2014.01.006

Hopkins, T. E., & Cech, J. J. (2003). The influence of environmental variables on the distribution and abundance of three elasmobranchs in Tomales Bay, California. Environmental Biology of Fishes, 66(3), 279–291. https://doi.org/10.1023/A:1023907121605

Hughes, B. B., Levey, M. D., Brown, J. A., Fountain, M. C., Carlisle, A. B., Litvin, S. Y., Greene, C. M., Heady, W. N., & Gleason, M. G. (2014). Nursery functions of U.S. West Coast estuaries: The state of knowledge for juveniles of focal invertebrates and fish species. 168.

Kim, S. L., & Koch, P. L. (2012). Methods to collect, preserve, and prepare elasmobranch tissues for stable isotope analysis. Environmental Biology of Fishes, 95(1), 53–63. https://doi.org/10.1007/s10641-011-9860-9

Kim, S. L., Tinker, M. T., Estes, J. A., & Koch, P. L. (2012). Ontogenetic and Among-Individual Variation in Foraging Strategies of Northeast Pacific White Sharks Based on Stable Isotope Analysis. PLoS ONE, 7(9). https://doi.org/10.1371/journal.pone.0045068

Larsen, T., Lee Taylor, D., Leigh, M. B., & O'Brien, D. M. (2009). Stable isotope fingerprinting: A novel method for identifying plant, fungal, or bacterial origins of amino acids. Ecology, 90(12), 3526–3535. https://doi.org/10.1890/08-1695.1

Larsen, T., Ventura, M., Andersen, N., Brien, D. M. O., Piatkowski, U., & Mccarthy, M. D. (2013). Tracing Carbon Sources through Aquatic and Terrestrial Food Webs Using Amino Acid Stable Isotope Fingerprinting. PLoS ONE, 8(9). https://doi.org/10.1371/journal.pone.0073441

Liu, Q., Chai, F., Dugdale, R., Chao, Y., Xue, H., Rao, S., Wilkerson, F., Farrara, J., Zhang, H., Wang, Z., & Zhang, Y. (2018). San Francisco Bay nutrients and plankton dynamics as simulated by a coupled hydrodynamic-ecosystem model. Continental Shelf Research, 161(March), 29–48. https://doi.org/10.1016/j.csr.2018.03.008

McCarthy, M. D., Benner, R., Lee, C., & Fogel, M. L. (2007). Amino acid nitrogen isotopic fractionation patterns as indicators of heterotrophy in plankton, particulate, and dissolved organic matter. Geochimica et Cosmochimica Acta, 71(19), 4727–4744. https://doi.org/10.1016/j.gca.2007.06.061

McClelland, J. W., Valiela, I., & Michener, R. H. (1997). Nitrogen-stable isotope signatures in estuarine food webs: A record of increasing urbanization in coastal watersheds. Limnology and Oceanography, 42(5 I), 930–937. https://doi.org/10.4319/lo.1997.42.5.0930

Mcmahon, K. W., Fogel, M. L., Elsdon, T. S., & Thorrold, S. R. (2010). Carbon Isotope Fractionation of Amino Acids in Fish Muscle Reflects Biosynthesis and Isotopic Routing from Dietary Protein. Journal of Animal Ecology, D, 1132–1141. https://doi.org/10.1111/j.1365-2656.2010.01722.x

Mcmahon, K. W., & Mccarthy, M. D. (2016). Embracing Variability in Amino Acid δ15N Fractionation: Mechanisms, Implications, and Applications for Trophic Ecology. Ecosphere, 7(December), 1–26. https://doi.org/10.1002/ecs2.1511

Mcmahon, K. W., Thorrold, S. R., Elsdon, T. S., & Mccarthy, M. D. (2015). Trophic discrimination of nitrogen stable isotopes in amino acids varies with diet quality in a marine fish. Limnology and Oceanography, 60(3), 1076–1087. https://doi.org/10.1002/lno.10081

Munroe, S. E. M., Simpfendorfer, C. A., & Heupel, M. R. (2014). Defining shark ecological specialisation: Concepts, context, and examples. Reviews in Fish Biology and Fisheries, 24(1), 317–331. https://doi.org/10.1007/s11160-013-9333-7

Nosal, A. P., Caillat, A., Kisfaludy, E. K., Royer, M. A., & Wegner, N. C. (2014). Aggregation behavior and seasonal philopatry in male and female leopard sharks Triakis semifasciata along the open coast of southern California , USA. 499, 157–175. https://doi.org/10.3354/meps10632

Nosal, A. P., Cartamil, D. C., Long, J. W., Lührmann, M., Wegner, N. C., & Graham, J. B. (2013). Demography and movement patterns of leopard sharks (Triakis semifasciata) aggregating near the head of a submarine canyon along the open coast of southern California, USA. Environmental Biology of Fishes, 96(7), 865–878. https://doi.org/10.1007/s10641-012-0083-5

Pedersen, E. J., Miller, D. L., Simpson, G. L., & Ross, N. (2019). Hierarchical generalized additive models in ecology: An introduction with mgcv. PeerJ, 7(e6876). https://doi.org/10.7717/peerj.6876

R Core Team. (2023). R: A Language and Environment for Statistical Computing. https://www.r-project.org/

Ramirez, M. D., Mcmahon, K. W., Besser, A. C., & Newsome, S. D. (2021). Meta-analysis of primary producer amino acid δ15N values and their influence on trophic position estimation. Methods in Ecology and Evolution, 12, 1750–1767. https://doi.org/10.1111/2041-210X.13678

Shipley, O. N., Henkes, G. A., Gelsleichter, J., Morgan, C. R., Schneider, E. V, Talwar, B. S., Frisk, M. G., & Shipley, O. N. (2021). Shark Tooth Collagen Stable Isotopes (δ15N and δ13C) as Ecological Proxies. Journal of Animal Ecology, 90(March), 2188–2201. https://doi.org/10.1111/1365-2656.13518

Simenstad, C. a, & Wissmar, R. C. (1985). δ13C evidence of the origins and fates of organic carbon in estuarine and nearshore food webs. Marine Ecology, 22, 141–152.

Smith, S. E. (2001). Leopard Shark. California's Marine Living Resources: A Status Report. Status of the Fisheries Report - An Update through 2006, February, 14-1-14–17.

Smith, S. E. (2005). Leopard shark mating observed off La Jolla, California. California Fish and Game, 91(2), 128–135.

Stahl, A. R., Rynearson, T. A., & Mcmahon, K. W. (2023). Amino acid carbon isotope fingerprints are unique among eukaryotic microalgal taxonomic groups. 68, 1331–1345. https://doi.org/10.1002/lno.12350

Tipple, B. J., Christensen, S., Ianiri, H. L., McCarthy, M. D., & Vokhshoori, N. L. (2021). A new molecular isotopic toolkit to examine estuarine food webs and biogeochemistry: Compound specific isotope analyses of amino acids from aquatic and terrestrial plants of the Sacramento-San Joaquin Delta, California [dataset bundled publication]. PANGAEA. https://doi.org/https://doi.org/10.1594/PANGAEA.938300

Trayler, R. B., Landa, P. V., & Kim, S. L. (2023). Evaluating the efficacy of collagen isolation using stable isotope analysis and infrared spectroscopy. Journal of Archaeological Science, 151(September 2022), 105727. https://doi.org/10.1016/j.jas.2023.105727

Vane, K., Cobain, M. R. D., & Larsen, T. (2025). The power and pitfalls of amino acid carbon stable isotopes for tracing the use and fate of basal resources in food webs. Ecological Monographs, 95(1), e1647. https://doi.org/10.1002/ecm.1647

Whiteman, J. P., Kim, S. L., McMahon, K. W., Koch, P. L., & Newsome, S. D. (2018). Amino acid isotope discrimination factors for a carnivore: physiological insights from leopard sharks and their diet. Oecologia, 188(4), 977–989. https://doi.org/10.1007/s00442-018-4276-2

Wood, S. N. (2017). Generalized Additive Models: An Introduction with R (Second).

Yarnes, C. T., & Herszage, J. (2017). The relative influence of derivatization and normalization procedures on the compound-specific stable isotope analysis of nitrogen in amino acids. Rapid Communications in Mass Spectrometry, 31(8), 693–704. https://doi.org/10.1002/rcm.7832

Zeichner, S. S., Colman, A. S., Koch, P. L., Polo-Silva, C., Galván-Magaña, F., & Kim, S. L. (2017). Discrimination factors and incorporation rates for organic matrix in shark teeth based on a captive feeding study. Physiological and Biochemical Zoology, 90(2), 257–272. https://doi.org/10.1086/689192

3.7 Figures

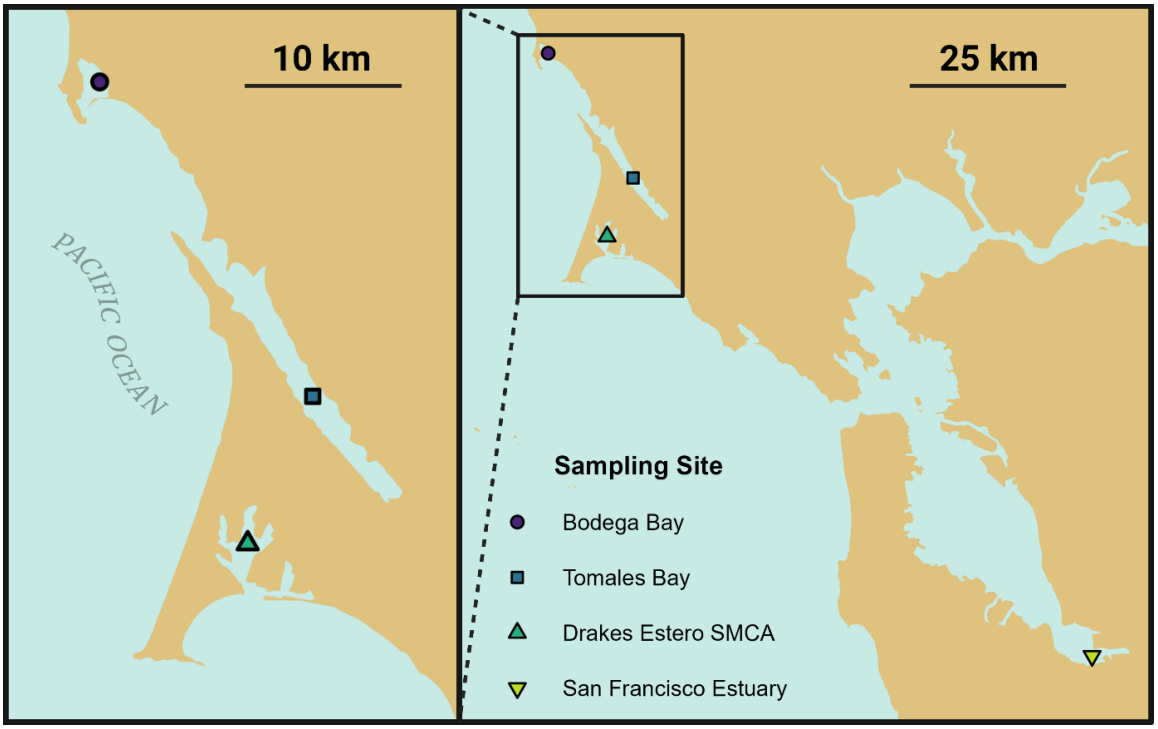

Figure 3.1: Leopard Shark sampling sites: Bodega Bay = purple circle; Tomales Bay = blue square; Drakes Estero SMCA = green triangle; the San Francisco Estuary = yellow upside-down triangle.

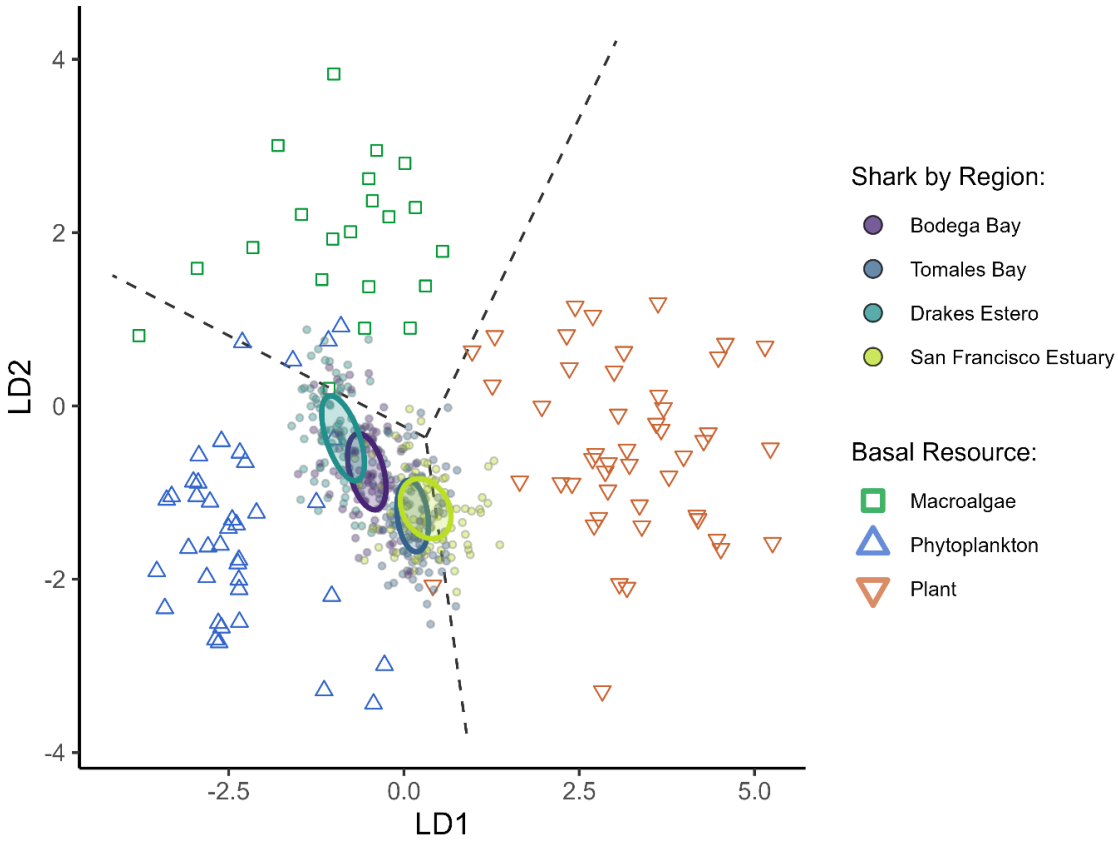

Figure 3.2: Linear discriminant analysis (LDA) of carbon sources and Leopard Sharks from coastal communities relevant to the sampled subpopulations. Carbon sources used to inform the LDA model included phytoplankton (blue triangles; n = 39), macroalgae (green squares; n = 21), and plants (brown upside-down triangles; n = 47). Predicted Leopard Shark LDA values are represented by circles, color-coded by region. Bayesian generalized linear mixed model-derived 95% confidence interval ellipses are shown for each region (Bodega Bay = purple, Tomales Bay = blue, Drakes Estero = green, San Francisco Estuary = yellow).

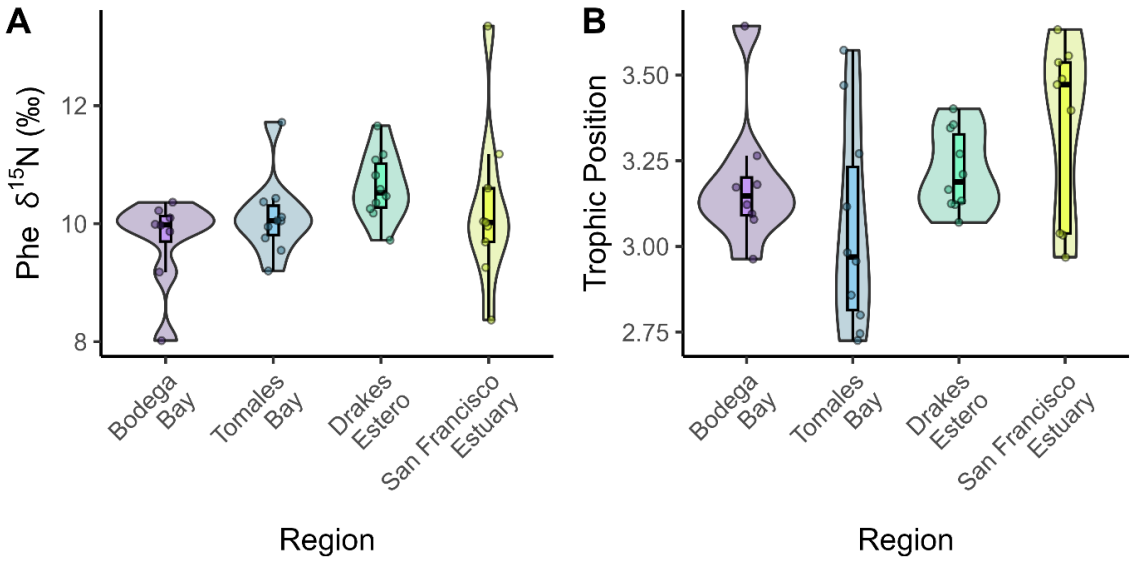

Figure 3.3: Regional variation in compound-specific $\delta^{15}N$ values from amino acid analysis (CSIA-AA). (A) $\delta^{15}N$ values of the source amino acid phenylalanine (Phe) and (B) $\delta^{15}N$-derived trophic levels, showing the distribution and variability across regions. Colors indicate region: purple = Bodega Bay, blue = Tomales Bay, green = Drake's Estero, and yellow = San Francisco Estuary.

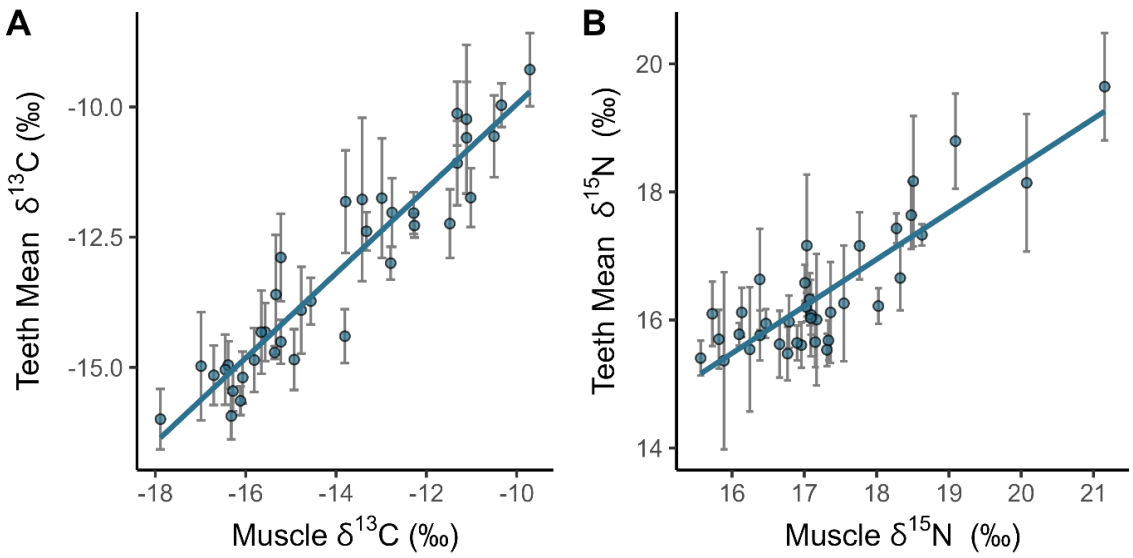

Figure 3.4: Relationship between isotopic values in muscle tissue and mean values from Leopard Shark tooth series. (A) Muscle $\delta^{13}C$ values are strongly correlated with mean tooth $\delta^{13}C$ values ($R^2 = 0.89$, $p < 0.001$), with standard deviation error bars representing intra-individual variation. (B) Muscle $\delta^{15}N$ values are significantly correlated with mean tooth $\delta^{15}N$ values ($R^2 = 0.74$, $p < 0.001$).

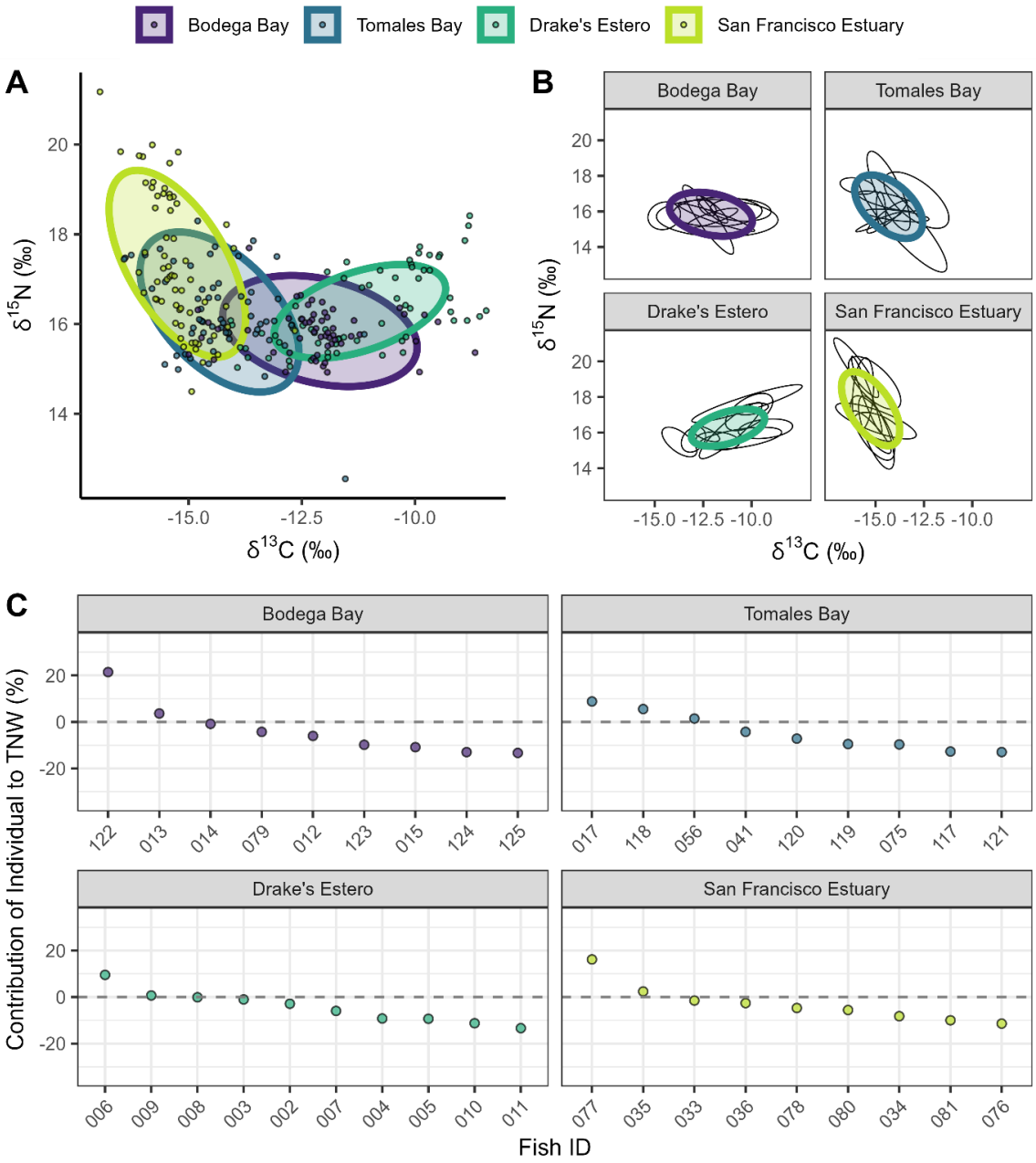

Figure 3.5: Isotopic niche and individual contribution of Leopard Sharks based on tooth dentin $\delta^{13}C$ and $\delta^{15}N$ values. (A) Seasonal regional isospace with 95% confidence intervals from Bayesian bivariate generalized linear models. (B) Subpopulation and individual niche ellipses by region. (C) Percent contribution of each individual to its region's total niche width (TNW). Regional ellipses and point colors denote sampled subpopulations: purple (Bodega Bay), blue (Tomales Bay), green (Drake's Estero), and yellow (San Francisco Estuary), while individual ellipses are outlined in black.

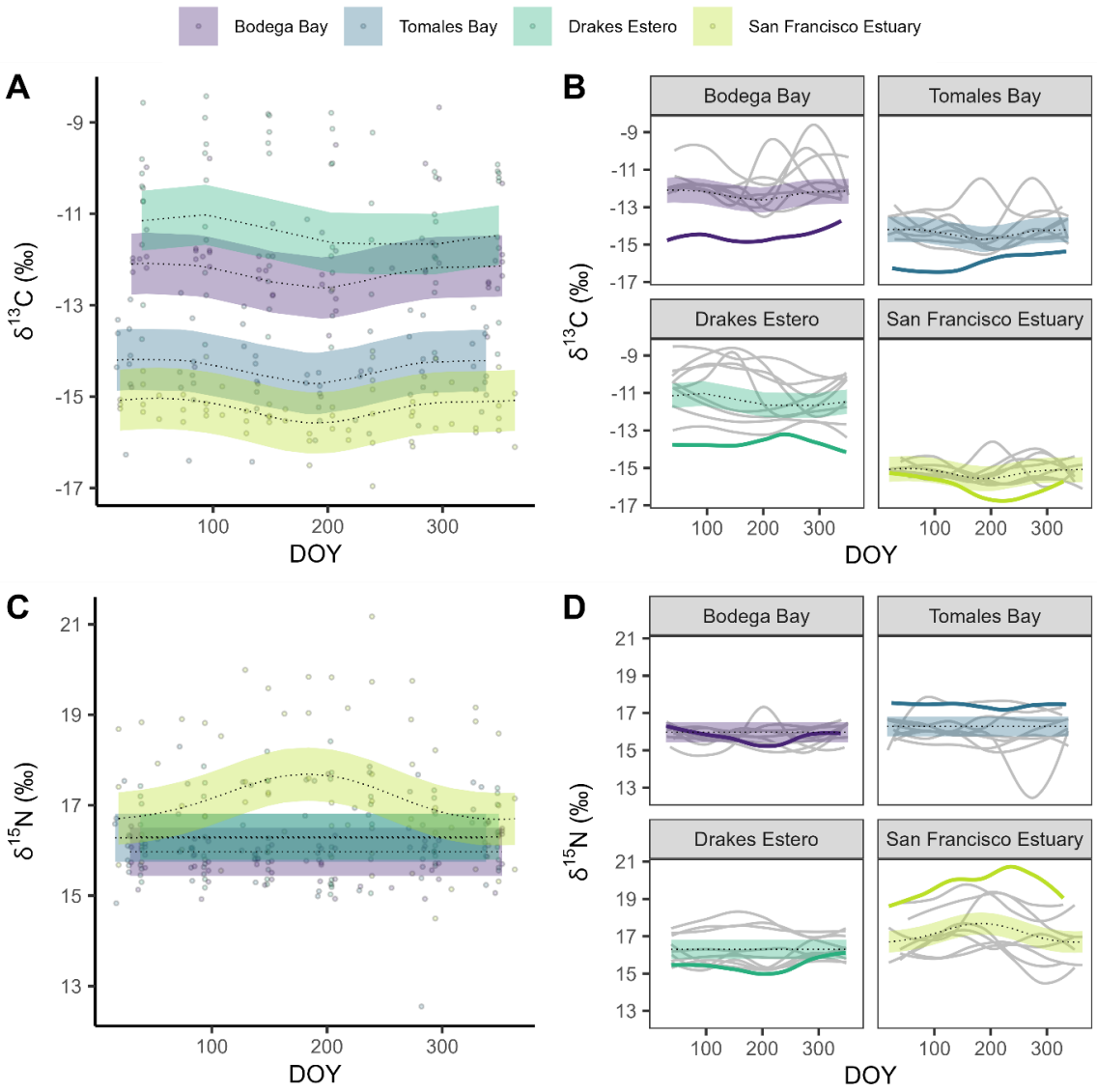

Figure 3.6: Hierarchical generalized additive model (HGAM) cyclic cubic spline smooths of (A) $\delta^{13}C$ and (C) $\delta^{15}N$ across day-of-year (DOY) for teeth isotope values, illustrating seasonal isotope variation. Subpopulation HGAM smooths for (B) $\delta^{13}C$ and (D) $\delta^{15}N$ are shown separately by region. Each dotted line represents the mean fit of the smooth for that region, while shaded regions around the smooth curves indicate 95% confidence intervals. Grey loess smooth lines represent individual trajectories, while colored loess smooth lines highlight the individual contributing most to its region's total niche width (TNW) and corresponds to the individual highlighted in Figure 5B. Regions are distinguished by color: purple (Bodega Bay), blue (Tomales Bay), green (Drake's Estero), and yellow (San Francisco Estuary).

3.8 Supplemental

3.8.1 Amino Acid $\delta^{13}C$ Fingerprinting

3.8.1.1 Basal Resource Values for Essential Amino Acids

Table 3.1: Essential Amino Acid $\delta^{13}C$ values for macroalgae, phytoplankton, and plant samples from California, USA.

Classification	Type	ID	Location	Ile	Leu	Lys	Phe	Thr	Val	Publication
Macroalgae	Rhodophyta	R1	Santa Cruz, CA	-17.3	-20.2	-10.9	-19.2	-6.4	-17.3	Larsen et al., 2013
Macroalgae	Rhodophyta	R2	Santa Cruz, CA	-15.4	-19.5	-13.0	-20.7	-4.8	-15.4	Larsen et al., 2013
Macroalgae	Rhodophyta	R3	Santa Cruz, CA	-21.7	-25.8	-16.4	-25.3	-9.2	-21.7	Larsen et al., 2013
Macroalgae	Rhodophyta	R4	Santa Cruz, CA	-17.0	-21.9	-14.9	-23.7	-11.0	-17.0	Larsen et al., 2013
Macroalgae	Rhodophyta	R5	Santa Cruz, CA	-19.5	-22.5	-16.4	-25.3	-15.3	-19.5	Larsen et al., 2013
Macroalgae	Rhodophyta	R6	Santa Cruz, CA	-16.5	-21.0	-13.1	-21.1	-8.7	-16.5	Larsen et al., 2013
Macroalgae	Rhodophyta	R7	Santa Cruz, CA	-16.7	-21.0	-11.0	-21.1	-5.9	-16.7	Larsen et al., 2013
Macroalgae	Rhodophyta	R8	Santa Cruz, CA	-18.0	-23.5	-15.8	-22.0	-7.3	-18.0	Larsen et al., 2013
Macroalgae	Rhodophyta	R9	Santa Cruz, CA	-20.4	-23.4	-13.3	-22.5	-6.8	-20.4	Larsen et al., 2013
Macroalgae	Phaeophyceae	P1	Big Sur, CA	-17.6	-23.1	-11.1	-19.4	-3.6	-17.6	Larsen et al., 2013
Macroalgae	Phaeophyceae	P2	Big Sur, CA	-15.2	-21.5	-9.1	-19.1	-1.2	-15.2	Larsen et al., 2013
Macroalgae	Phaeophyceae	P3	Big Sur, CA	-19.6	-24.8	-12.7	-22.2	-5.5	-19.6	Larsen et al., 2013
Macroalgae	Phaeophyceae	P4	Big Sur, CA	-16.8	-20.0	-9.9	-18.9	-0.4	-16.8	Larsen et al., 2013
Macroalgae	Phaeophyceae	P5	Big Sur, CA	-21.4	-26.1	-14.1	-23.9	-6.4	-21.4	Larsen et al., 2013
Macroalgae	Phaeophyceae	P6	Santa Cruz, CA	-6.3	-13.3	-1.7	-12.8	-2.6	-6.3	Larsen et al., 2013
Macroalgae	Phaeophyceae	P7	Santa Cruz, CA	-15.6	-23.9	-9.2	-18.8	-1.2	-15.6	Larsen et al., 2013
Macroalgae	Phaeophyceae	P8	Santa Cruz, CA	-19.5	-25.5	-10.7	-20.4	-0.5	-19.5	Larsen et al., 2013
Macroalgae	Phaeophyceae	P9	Santa Cruz, CA	-10.9	-18.3	-8.2	-16.7	0.9	-10.9	Larsen et al., 2013
Macroalgae	Phaeophyceae	P10	Santa Cruz, CA	-16.9	-23.6	-10.8	-23.6	5.4	-16.9	Larsen et al., 2013
Macroalgae	Phaeophyceae	P11	Santa Cruz, CA	-7.3	-14.7	-4.5	-12.7	0.8	-7.3	Larsen et al., 2013
Macroalgae	Phaeophyceae	P12	Santa Cruz, CA	-17.6	-25.2	-9.1	-21.2	-8.6	-17.6	Larsen et al., 2013
Plant	Zosteraceae	S6	Santa Cruz, CA	-17.5	-21.4	-12.7	-17.0	-12.2	-17.5	Larsen et al., 2013

Classification	Type	ID	Location	Ile	Leu	Lys	Phe	Thr	Val	Publication
Plant	Zosteraceae	S7	Santa Cruz, CA	-19.8	-23.1	-13.0	-17.6		-19.8	Larsen et al., 2013
Phytoplankton	Dinoflagellate	X28.1	La Jolla, CA	-14.6	-29.1	-12.5	-23.2	-11.0	-14.6	Stahl et al., 2023
Phytoplankton	Dinoflagellate	X28.2	La Jolla, CA	-17.0	-31.5	-13.4	-23.0	-10.7	-17.0	Stahl et al., 2023
Phytoplankton	Dinoflagellate	X28.3	La Jolla, CA	-15.0	-31.2	-14.3	-22.6	-8.5	-15.0	Stahl et al., 2023
Phytoplankton	Dinoflagellate	X29.1	Monterey Bay, CA	-7.5	-20.6	-3.0	-12.5	-3.3	-7.5	Stahl et al., 2023
Phytoplankton	Dinoflagellate	X29.2	Monterey Bay, CA	-7.5	-21.7	-5.1	-12.9	-2.0	-7.5	Stahl et al., 2023
Phytoplankton	Dinoflagellate	X29.3	Monterey Bay, CA	-9.1	-21.5	-5.4	-13.6	-2.9	-9.1	Stahl et al., 2023
Phytoplankton	Dinoflagellate	X37.1	Monterey Bay, CA	-8.8	-19.2	-2.5	-13.5	-3.2	-8.8	Stahl et al., 2023
Phytoplankton	Dinoflagellate	X37.2	Monterey Bay, CA	-10.1	-19.9	-3.3	-14.3	-3.9	-10.1	Stahl et al., 2023
Phytoplankton	Dinoflagellate	X37.3	Monterey Bay, CA	-9.1	-18.1	-3.9	-11.9	-1.0	-9.1	Stahl et al., 2023
Phytoplankton	Dinoflagellate	X40.1	Monterey Bay, CA	-10.8	-22.3	-5.4	-16.8	-5.4	-10.8	Stahl et al., 2023
Phytoplankton	Dinoflagellate	X40.2	Monterey Bay, CA	-11.1	-24.3	-5.5	-17.1	-6.8	-11.1	Stahl et al., 2023
Phytoplankton	Dinoflagellate	X40.3	Monterey Bay, CA	-10.1	-23.4	-4.2	-15.5	-4.5	-10.1	Stahl et al., 2023
Phytoplankton	Prasinophyte	X48.1	Pacific Ocean, CA	-17.3	-23.7	-10.9	-22.4	-8.2	-17.3	Stahl et al., 2023
Phytoplankton	Prasinophyte	X48.2	Pacific Ocean, CA	-17.3	-23.6	-9.6	-23.4	-8.9	-17.3	Stahl et al., 2023
Phytoplankton	Prasinophyte	X48.3	Pacific Ocean, CA	-17.2	-23.7	-11.9	-22.5	-7.2	-17.2	Stahl et al., 2023
Plant	Water primrose	1A	Mildred Island, CA	-26.8	-33.6	-26.4	-27.2	-22.9	-26.8	Tipple et al., 2021
Plant	Azolla	2A	Mildred Island, CA	-29.3	-32.0	-26.8	-28.0	-23.5	-29.3	Tipple et al., 2021
Plant	Brazilian waterweed	3A	Mildred Island, CA	-27.0	-31.2	-24.0	-29.0	-20.1	-27.0	Tipple et al., 2021
Plant	Fanwort	4A	Mildred Island, CA	-35.1	-39.6	-28.5	-33.2	-27.5	-35.1	Tipple et al., 2021
Plant	Brazilian waterweed	5A	Mildred Island, CA	-29.1	-35.3	-27.2	-33.5	-24.7	-29.1	Tipple et al., 2021
Plant	Duckweed	6A	Mildred Island, CA	-30.4	-36.0	-25.4	-29.2	-22.1	-30.4	Tipple et al., 2021
Plant	Azolla	7A	Mildred Island, CA	-28.6	-37.3	-14.6	-33.2	-20.6	-28.6	Tipple et al., 2021
Plant	Coontail	8A	Mildred Island, CA	-24.6	-32.8	-21.4	-26.6	-19.9	-24.6	Tipple et al., 2021
Plant	Brazilian waterweed	9A	Mildred Island, CA	-24.2	-30.7	-24.5	-32.4	-19.7	-24.2	Tipple et al., 2021
Plant	Water primrose	10A	Mildred Island, CA	-24.9	-34.5	-23.6	-28.1	-17.7	-24.9	Tipple et al., 2021
Plant	Sponge plant	11A	Mildred Island, CA	-28.7	-36.6	-30.2	-28.4	-25.6	-28.7	Tipple et al., 2021

Classification	Type	ID	Location	Ile	Leu	Lys	Phe	Thr	Val	Publication
Plant	Water hyacinth	12A	Mildred Island, CA	-30.0	-33.7	-28.0	-27.1	-22.3	-30.0	Tipple et al., 2021
Plant	Willow	13A	Mildred Island, CA	-27.1	-34.9	-24.7	-27.7	-18.7	-27.1	Tipple et al., 2021
Plant	Willow	14A	Mildred Island, CA	-25.2	-35.6	-25.9	-30.0	-18.1	-25.2	Tipple et al., 2021
Plant	Tule	15A	Mildred Island, CA	-26.3	-34.4	-23.9	-27.3	-20.3	-26.3	Tipple et al., 2021
Plant	Tule	16A	Mildred Island, CA	-26.1	-35.7	-26.3	-27.4	-16.2	-26.1	Tipple et al., 2021
Plant	Pennywort	17A	Mildred Island, CA	-27.3	-32.0	-22.5	-27.8	-22.8	-27.3	Tipple et al., 2021
Plant	Pennywort	18A	Mildred Island, CA	-26.0	-32.8	-25.1	-30.0	-19.1	-26.0	Tipple et al., 2021
Plant	Iris	19A	Mildred Island, CA	-28.9	-33.3	-24.0	-27.1	-29.0	-28.9	Tipple et al., 2021
Plant	Lady fern	20A	Mildred Island, CA	-25.1	-31.0	-22.1	-22.7	-18.0	-25.1	Tipple et al., 2021
Plant	Giant reed	21A	Mildred Island, CA	-27.0	-35.5	-22.6	-28.5	-15.3	-27.0	Tipple et al., 2021
Plant	Coontail	1B	Liberty Island, CA	-33.3	-38.9	-26.4	-32.5	-25.2	-33.3	Tipple et al., 2021
Plant	Eurasian water milfoil	2B	Liberty Island, CA	-21.7	-26.5	-19.6	-21.7	-15.4	-21.7	Tipple et al., 2021
Plant	Canadian waterweed	4B	Liberty Island, CA	-26.2	-32.5	-26.0	-27.7	-19.3	-26.2	Tipple et al., 2021
Plant	Eurasian water milfoil	5B	Liberty Island, CA	-21.3	-26.2	-14.6	-20.7	-13.1	-21.3	Tipple et al., 2021
Plant	Phragmites	6B	Liberty Island, CA	-26.6	-33.3	-26.1	-28.1	-18.5	-26.6	Tipple et al., 2021
Plant	Curly leaf pondweed	7B	Liberty Island, CA	-29.6	-34.0	-24.0	-28.4	-24.4	-29.6	Tipple et al., 2021
Plant	Sago pondweed	8B	Liberty Island, CA	-24.4	-29.0	-23.0	-24.5	-17.7	-24.4	Tipple et al., 2021
Plant	Tule	9B	Liberty Island, CA	-28.7	-37.2	-27.9	-29.4	-23.1	-28.7	Tipple et al., 2021
Plant	Sago pondweed	10B	Liberty Island, CA	-22.0	-26.0	-20.4	-24.7	-19.5	-22.0	Tipple et al., 2021
Plant	Willow	11B	Liberty Island, CA	-24.7	-33.2	-24.5	-27.8	-20.0	-24.7	Tipple et al., 2021
Plant	Brazilian waterweed	12B	Liberty Island, CA	-27.9	-34.0	-25.3	-32.7	-21.6	-27.9	Tipple et al., 2021
Plant	North CA Walnut	D1	Big Break, CA	-24.4	-33.9	-23.0	-27.0	-15.8	-24.4	Tipple et al., 2021
Plant	Almond	D2	Big Break, CA	-29.1	-39.2	-29.1	-30.8	-20.3	-29.1	Tipple et al., 2021
Plant	Saltgrass	D4	Big Break, CA	-14.1	-22.2	-15.8	-15.4	-7.0	-14.1	Tipple et al., 2021
Plant	Coast Live Oak	D5	Big Break, CA	-25.2	-35.4	-25.0	-27.4	-11.9	-25.2	Tipple et al., 2021
Plant	Coast Live Oak	D7	Big Break, CA	-29.5	-34.9	-23.4	-28.1	-14.4	-29.5	Tipple et al., 2021
Plant	Coast Live Oak	D8	Big Break, CA	-25.5	-34.8	-22.3	-25.6	-12.1	-25.5	Tipple et al., 2021

Classification	Type	ID	Location	Ile	Leu	Lys	Phe	Thr	Val	Publication
Plant	Himalaya Blackberry	D9	Big Break, CA	-25.3	-35.9	-24.6	-29.0	-10.9	-25.3	Tipple et al., 2021
Plant	Woolly Firethorn	D10	Big Break, CA	-22.7	-36.3	-24.8	-27.5	-18.6	-22.7	Tipple et al., 2021
Plant	Seaside Heliotrope	D11	Big Break, CA	-26.3	-33.9	-22.8	-29.5	-11.9	-26.3	Tipple et al., 2021
Plant	Yerba Mansa	D12	Big Break, CA	-25.4	-34.9	-23.6	-27.7	-16.1	-25.4	Tipple et al., 2021
Plant	Japan Honeysuckle	D13	Big Break, CA	-25.1	-35.3	-26.0	-29.5	-19.9	-25.1	Tipple et al., 2021
Plant	Grass	D14	Big Break, CA	-26.2	-30.2	-22.8	-29.3	-14.4	-26.2	Tipple et al., 2021
Plant	Slender Peppergrass	D15	Big Break, CA	-28.3	-34.3	-23.6	-30.9	-11.7	-28.3	Tipple et al., 2021
Plant	California Wildrose	D16	Big Break, CA	-24.1	-31.9	-17.5	-26.6	-11.5	-24.1	Tipple et al., 2021
Plant	Forest Red Gum	D17	Big Break, CA	-26.1	-33.5	-22.0	-29.7	-18.1	-26.1	Tipple et al., 2021
Plant	Spanish clover	D18	Big Break, CA	-26.4	-33.3	-21.9	-28.1	-10.1	-26.4	Tipple et al., 2021
Plant	Rush	D19	Big Break, CA	-38.7	-29.0	-24.2	-31.4	-17.0	-38.7	Tipple et al., 2021
Plant	Fremont Cottonwood	D20	Big Break, CA	-30.2	-37.4	-27.0	-32.5	-16.5	-30.2	Tipple et al., 2021
Plant	Narrow-leaf Cattail	D21	Big Break, CA	-31.8	-34.7	-26.2	-29.6	-23.5	-31.8	Tipple et al., 2021
Plant	Urugary primrose	D22	Big Break, CA	-26.1	-36.4	-25.2	-29.4	-20.0	-26.1	Tipple et al., 2021
Plant	Sedge	D23	Big Break, CA	-31.4	-33.1	-25.1	-28.0	-15.5	-31.4	Tipple et al., 2021

3.8.1.2 References

Larsen, T., Ventura, M., Andersen, N., Brien, D. M. O., Piatkowski, U., & Mccarthy, M. D. (2013). Tracing Carbon Sources through Aquatic and Terrestrial Food Webs Using Amino Acid Stable Isotope Fingerprinting. PLoS ONE, 8(9). https://doi.org/10.1371/journal.pone.0073441

Stahl, A. R., Rynearson, T. A., & Mcmahon, K. W. (2023). Amino acid carbon isotope fingerprints are unique among eukaryotic microalgal taxonomic groups. 68, 1331–1345. https://doi.org/10.1002/lno.12350

Tipple, B. J., Christensen, S., Ianiri, H. L., McCarthy, M. D., & Vokhshoori, N. L. (2021). A new molecular isotopic toolkit to examine estuarine food webs and biogeochemistry: Compound specific isotope analyses of amino acids from aquatic and terrestrial plants of the Sacramento-San Joaquin Delta, California [dataset bundled publication]. PANGAEA. https://doi.org/https://doi.org/10.1594/PANGAEA.938300

3.8.2 Linear Discriminant Analysis Prior to TDFs

We applied Linear Discriminant Analysis (LDA) to essential amino acid $\delta^{13}C$ values from Leopard Shark muscle tissue prior to applying amino acid–specific trophic discrimination factors (TDFs). Across all sites, Leopard Sharks were uniformly classified as relying exclusively on macroalgal basal resources.

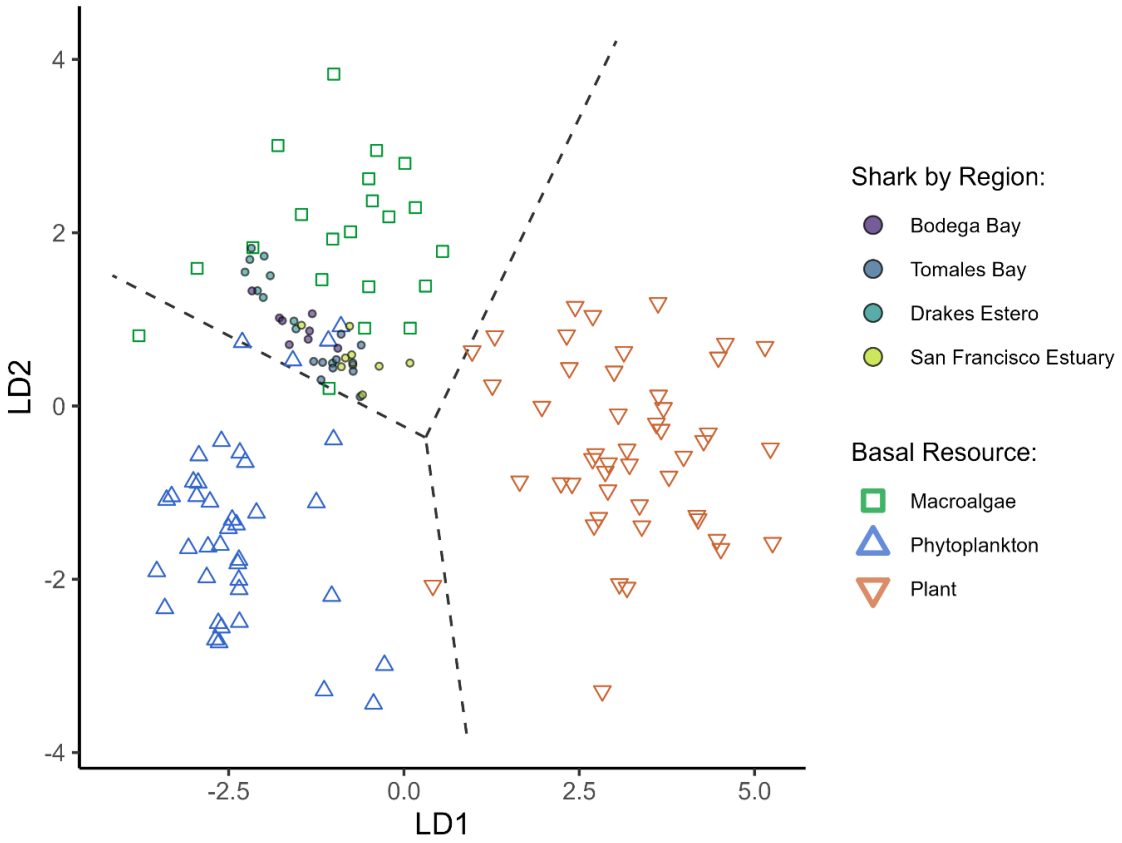

Figure 3.7: Linear discriminant analysis (LDA) of carbon sources and Leopard Sharks from coastal communities relevant to the sampled subpopulations. Carbon sources used to inform the LDA model included phytoplankton (blue triangles; n = 39), macroalgae (green squares; n = 21), and plants (brown upside-down triangles; n = 47). Predicted Leopard Shark LDA values are represented by circles, color-coded by region (Bodega Bay = purple, Tomales Bay = blue, Drakes Estero = green, San Francisco Estuary = yellow).

3.8.3 Amino Acid $\delta^{15}N$ Trophic Estimation

3.8.3.1 Use of different TDFs

To assess the sensitivity of trophic position (TP) estimates to variation in trophic discrimination factors ($TDF_{Glx\text{-}Phe}$), we applied a range of published and unpublished values, beginning with the original 7.6 ‰ value from Chikaraishi et al. (2009), which is widely used in compound-specific isotope analysis of amino acids (CSIA-AA). We also tested Mcmahon et al.'s (2015) squid diet value for Atlantic killifish (5.1 ‰), Whiteman

et al.'s (2018) unpublished Leopard Shark-specific estimate (3.2‰), Hoen et al.'s (2014) Leopard Shark-specific value (2.6‰), and their broader all-shark average (2.3‰). Theoretically, the Leopard Shark-specific TDFs derived from a four-year captive feeding study would be the most appropriate for this study; however, applying these lower TDFs produced trophic position estimates that were widely inflated and ecologically implausible (Fig. 3.8C,D). This outcome supports the hypothesis that Leopard Shark amino acid $\delta^{15}N$ values in the feeding study may not have reached isotopic steady state, limiting the reliability of those empirically derived TDFs (Whiteman et al., 2018). While both the 7.6 ‰ and 5.1 ‰ TDFs yielded more ecologically reasonable TP estimates (Fig. 3.8A,B) in line with previous work (Cortés, 1999), the 7.6 ‰ value—originally calibrated for herbivorous consumers—likely underestimates true trophic position in a carnivorous species like the Leopard Shark. Nonetheless, given the uncertainty surrounding elasmobranch TDFs, the 7.6 ‰ value was used here to ensure consistency with established analytical frameworks while minimizing the risk of biologically unrealistic estimates.

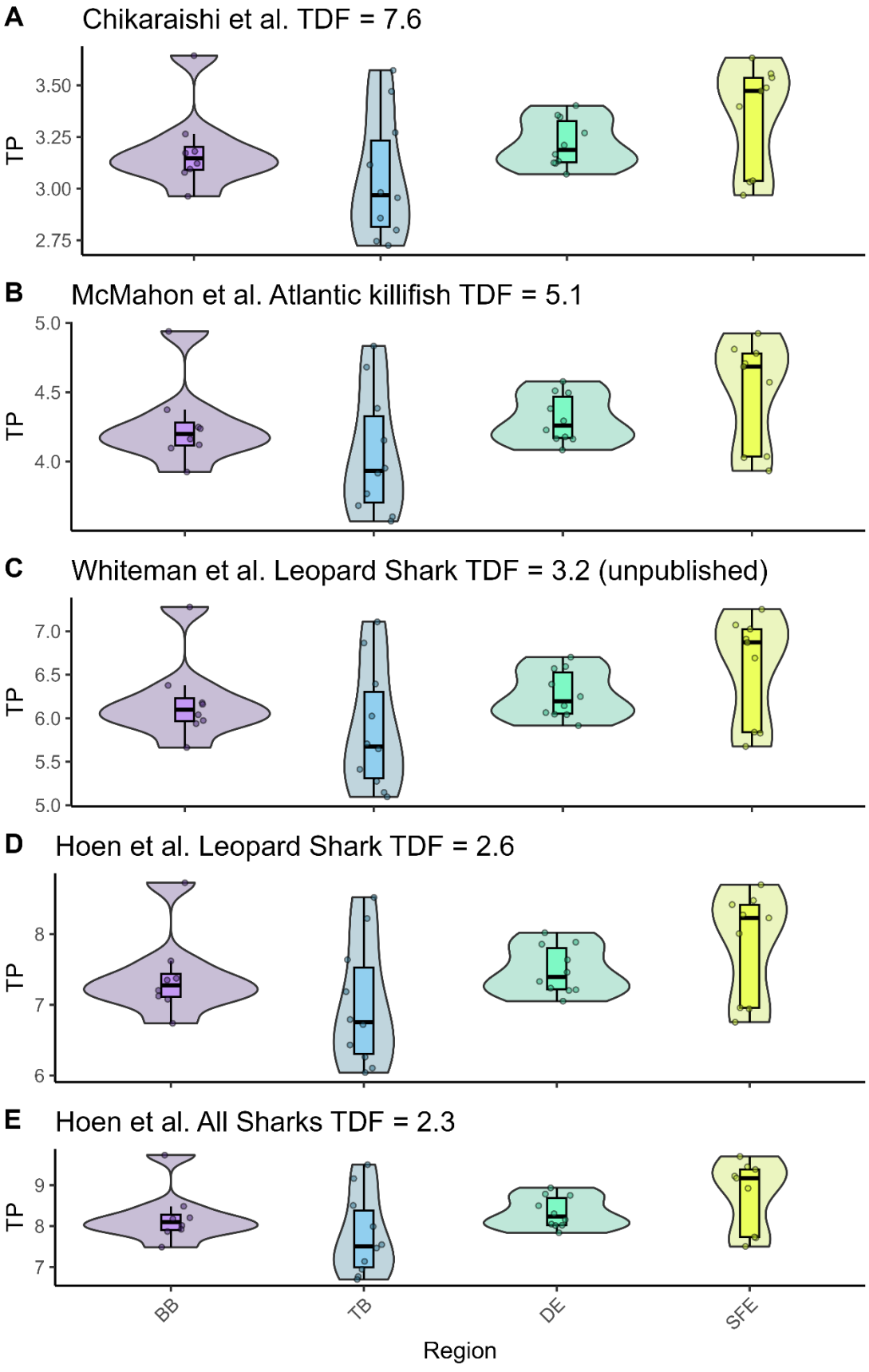
A
Chikaraishi et al. TDF = 7.6
TP
3.50
3.25
3.00
2.75
B
McMahon et al. Atlantic killifish TDF = 5.1
TP
5.0
4.5
4.0
C
Whiteman et al. Leopard Shark TDF = 3.2 (unpublished)
TP
7.0
6.5
6.0
5.5
5.0
D
Hoen et al. Leopard Shark TDF = 2.6
TP
8
7
6
E
Hoen et al. All Sharks TDF = 2.3
TP
9
8
7
BB
TB
DE
SFE
Region

Figure 3.8: Regional variation in trophic position (TP) estimated from compound-specific $\delta^{15}N$ values of amino acids (CSIA-AA), calculated using five different trophic discrimination factors (TDFs): (A) 7.6‰, (B) 5.1‰, (C) 3.2‰, (D) 2.6‰, and (E) 2.3‰. Each panel shows the distribution and variability of $\delta^{15}N$-derived TP across regions. Regions are distinguished by color: purple = Bodega Bay, blue = Tomales Bay, green = Drakes Estero, and yellow = San Francisco Estuary.

3.8.3.2 References

Chikaraishi, Y., Ogawa, N. O., Kashiyama, Y., Takano, Y., Suga, H., Tomitani, A., Miyashita, H., Kitazato, H., & Ohkouchi, N. (2009). Determination of aquatic food-web structure based on compound-specific nitrogen isotopic composition of amino acids. Limnology and Oceanography: Methods, 7(NOV), 740–750. https://doi.org/10.4319/lom.2009.7.740

Cortés, E. (1999). Standardized diet compositions and trophic levels of sharks. ICES Journal of Marine Science, 56(5), 707–717. https://doi.org/10.1006/jmsc.1999.0489

Hoen, D. K., Kim, S. L., Hussey, N. E., Wallsgrove, N. J., Drazen, J. C., & Popp, B. N. (2014). Amino acid 15N trophic enrichment factors of four large carnivorous fishes. Journal of Experimental Marine Biology and Ecology, 453, 76–83. https://doi.org/10.1016/j.jembe.2014.01.006

Mcmahon, K. W., Thorrold, S. R., Elsdon, T. S., & Mccarthy, M. D. (2015). Trophic discrimination of nitrogen stable isotopes in amino acids varies with diet quality in a marine fish. Limnology and Oceanography, 60(3), 1076–1087. https://doi.org/10.1002/lno.10081

Whiteman, J. P., Kim, S. L., McMahon, K. W., Koch, P. L., & Newsome, S. D. (2018). Amino acid isotope discrimination factors for a carnivore: physiological insights from leopard sharks and their diet. Oecologia, 188(4), 977–989. https://doi.org/10.1007/s00442-018-4276-2

4. Chapter 3: Investigating eye lens composition for Stable Isotope Analysis — A comparison between Chondrichthyan and Actinopterygian fishes

4.1 Introduction

Habitat use and trophic dynamics vary with ontogeny, but are difficult to discern for long-lived, mobile aquatic and marine organisms, such as Chondrichthyans (i.e., cartilaginous fishes; sharks, skates, rays, sawfish, and chimeras) and Teleosts (i.e., ray finned fishes). Many ecological studies serially sample inert inorganic accretionary tissues from fishes (e.g., otoliths in Teleost and cartilaginous vertebrae in Chondrichthyans) for stable isotope analysis (SIA), which provides a lifetime record of diet and/or habitat use. However, these inert and primarily inorganic structures are not present across all fishes and prevent comparisons between Chondrichthyans and Teleosts. An alternative inert, accumulative, and proteinaceous tissue is the eye lens and its layers (laminae). Most studies using eye lens laminae for SIA focus on Teleost fishes (Bell-Tilcock et al., 2020; Vecchio & Peebles, 2020; Wallace et al., 2014), but there is potential for using this archival tissue in Chondrichthyans (Quaeck-Davies et al., 2018; Simpson et al., 2019). However, differences in biomolecule levels, such as lipids and urea, can affect SIA and differ among Chondrichthyan and Teleost. For example, Chondrichthyans are neutrally buoyant with large, lipid-rich livers and osmoregulate by retaining urea (Gleiss et al., 2017; Hazon et al., 2003), which are different mechanisms than Teleost fishes. Thus, it is important to characterize the taxa-specific differences in elemental components of eye lenses to establish Chondrichthyan eye lens laminae as a chronological tissue for SIA.

Stable isotope composition ($\delta^{13}C$ and $\delta^{15}N$) can reveal the diet and habitat use of a consumer. The $\delta^{13}C$ and $\delta^{15}N$ values of an individual's tissues are dependent on its nutritional resources, which varies based on the isotopic composition of primary producers, and extent of differentiation with trophic level (DeNiro & Epstein, 1978; Post, 2002). Isotopic differentiation at each trophic step occurs with physiological processes that sort (i.e., fractionate) and change the isotopic ratio (e.g., $^{13}C/^{12}C$ and $^{15}N/^{14}N$). For example, organisms respire and excrete waste with the expelled CO_2 and N enriched in the light isotope (i.e., ^{12}C and ^{14}N), causing biomagnification of the heavy isotope (i.e., ^{13}C and ^{15}N) in consumer tissues (DeNiro & Epstein, 1978; Post, 2002). In addition, different consumer tissues uptake stable isotopes at different rates (i.e., incorporation rate; (Carleton & Del Rio, 2005; Kim et al., 2012b; Tieszen et al., 1983; Weidel et al., 2011) and have different offsets from diet based on a variety of factors (i.e., trophic discrimination factor; (Kim et al., 2012a), which are important for ecological interpretations. While most tissues allow for ecological interpretation based on a single point in time (e.g., muscle, liver, etc.), accretionary or accumulative structures, such as

otoliths, cartilaginous vertebrae, and eye lens laminae, continually deposit and provide a time series. In Teleost fishes, the SIA of eye lens laminae reflects a chronological record of diet and movement from early development until death (Bell-Tilcock et al., 2020; Quaeck-Davies et al., 2018; Vecchio & Peebles, 2022; Wallace et al., 2014). However, a key component to resolving spatial and dietary patterns with SIA is ensuring that biomolecular composition does not coincide with isotopic variation.

Proteinaceous tissues are often the preferred substrate for studying diet with SIA, but varying levels of biomolecules synthesized through various metabolic pathways, such as urea, can affect the isotopic composition. Chondrichthyes exhibit higher levels of urea ($C{=}O(N{-}H_2)_2$) and since this biomolecule has a higher proportion of nitrogen compared to other biomolecules, it leads to lower a C:N ratio than expected for protein (e.g., Leopard Shark pre-urea extracted shark muscle $C{:}N_{\text{weight \%}}$ ratio ≈ 2.7; Leopard Shark post urea-extracted shark muscle $C{:}N_{\text{weight \%}}$ ratio ≈ 3.2; Kim & Koch, 2012). During protein metabolism, it is energetically favorable to synthesize ^{14}N as a waste byproduct in urea while ^{15}N is retained in biomolecules such as amino acids. Although most organisms excrete this ^{14}N-enriched urea, the retention of urea in Chondrichthyes lowers the overall bulk tissue $\delta^{15}N$ value (Kim & Koch, 2012). In stable isotope ecology studies using muscle, the C:N ratio is often used as an indicator for urea and monitored for its effects on $\delta^{15}N$ values (Kim & Koch, 2012). However, to date, there remains no documented evidence of urea in the eye lenses of fishes.

The eye lens is a chronological tissue in the vertebrate eye (Fig. 4.1A) that forms laminae, similar to the layers of an onion, across the entire lifetime of the individual (Tzadik et al., 2017; Wallace et al., 2014). After formation of the outermost membrane (i.e., the lens capsule), a layer of cuboidal epithelial cells adjacent and medial to the capsule forms, divides and differentiates into lens fiber cells, which are primarily composed of crystallin protein (Fig. 4.1B-D; Andley, 2008; Berman, 1991; Horwitz, 2003; Nicol et al., 1989). Primary lens fiber cells are laid down during embryonic development (i.e., lens nucleus), while secondary lens fiber cells are stacked laterally to existing lens fiber cells, creating a layering of laminae (Fig. 4.1B; Andley 2008). During the transition from epithelial cell to secondary lens fiber cells, living organelles and their corresponding biomolecules are present for cellular function causing a hydrated laminae (i.e., pre-apoptotic laminae; Fig. 4.1B; Berman 1991). After a new suite of lens fiber cells are differentiated, previously established secondary lens fiber cells undergo partial apoptosis, removing living organelles and water molecules, leaving behind a rigid, inert, and tightly packed crystallin protein structure (i.e., post-apoptotic laminae; Fig. 4.1B,C). The eye lens can therefore be serially sampled from the most recently differentiated secondary lens fiber cells (e.g., outer laminae representing most recent time) to inner primary lens fiber cells (e.g., core representing embryonic development/early life). While most of the eye lens is easily sampled, there is a transition zone from rigid post-apoptotic laminae to more hydrated pre-apoptotic that are less distinguishable (Fig. 4.1B). Due to the eye lens being non-vascularized, it receives nutrients via diffusion of aqueous humor across the lens capsule (Berman 1991). In Chondrichthyans, these outer hydrated pre-apoptotic laminae adjacent to the capsule are also permeable (Quaeck-Davies et al.,

2018), and may be subject to the addition of uncharacterized biomolecules (Fig. 4.1B-D), such as urea

The SIA of Teleost eye lenses provides crucial insights to ecological patterns, such as movement, trophic interactions, and natal origin (Bell-Tilcock et al., 2020; Tzadik et al., 2017; Vecchio & Peebles, 2020, 2022; Wallace et al., 2014). Few studies have focused on Chondrichthyan ecology using eye lens laminae (Quaeck-Davies et al., 2018; Simpson et al., 2019); however, times series of SIA would be particularly useful for ecological studies of ontogeny given their large spatial and temporal ranges. One study to date noted challenges in sampling of outer pre-apoptotic eye lens laminae for Chondrichthyans (Quaeck-Davies et al., 2018). The difference in rigid post-apoptotic and hydrated pre-apoptotic laminae was likely representative of a compositional change at the biomolecular scale. While C:N ratio can provide an understanding of large-scale chemical changes, different biomolecular species within a tissue are made up of distinct functional groups. To characterize the biomolecular composition of Chondrichthyan eye laminae, we used Attenuated Total Reflectance (ATR) - Fourier Transform Infrared (FTIR) spectroscopy (Stuart, 2004), then quantified changes in urea concentration across eye laminae from post- to pre-apoptotic zones. Here we ask: 1) How do C:N ratios vary across eye lens laminae and among taxa, 2) Is urea presence correlated with changes in C:N ratios of Chondrichthyan eye lenses, and 3) Does urea affect stable isotope values in the Chondrichthyan eye lens? By investigating the chemical and biomolecular makeup of Chondrichthyes eye lens laminae across fish taxa, we aim to establish this substrate to investigate questions regarding ontogeny and life history.

4.2 Materials and Methods

4.2.1 Sampling Procedures

The biomolecular composition of eye lens was compared between three Chondrichthyan species and three Teleost species, with nine adult Leopard Sharks, one adult Sandbar Shark, and one adult Zebra Shark collected for Chondrichthyans, and twelve juvenile Black Sea Bass, twelve juvenile Red Grouper, and twelve adult Atlantic Salmon collected for Teleosts (Table 4.1). We dissected and measured eye lens laminae chronologically, offering a means to retroactively reconstruct the life and growth history of an individual fish. Eye lenses were dissected from whole eyes and serially sampled (i.e., delaminated), from the outer lamina, which represented most recent life history, to laminar core, which represented early development (Fig. 4.1B). For Chondrichthyans, serially sampled eye lenses were photographed at 10x magnification with an imaging camera (Amscope MU1803-HS) attached to stereoscope (Leica S8APO) to later record chronological eye lens laminar measurements. After each lamina was delaminated, we conducted measurements by selecting four evenly spaced directions or angles around the circumference of the eye lens to ensure a representative sampling of measurements for determining its diameter (mm; mean SD = ± 0.1 mm; subset individuals n = 2, laminae n = 31) via ImageJ (Schneider et al., 2012). The outer-most pre-apoptotic laminae, adjacent to the lens capsule, are hydrated and difficult to measure directly. Consequently, these outer-most pre-apoptotic laminae were not included for the Sandbar and Zebra Shark. For the outermost hydrated laminae of the Leopard Sharks, we calculated the laminar

midpoint following the method outlined by Vecchio and Peebles (2022). For Teleost fishes, Atlantic salmon eye lens laminae were also photographed and measured for diameter using an imaging camera (HiChrome HR4K) attached to a stereoscope (Leica S9D), following procedures outlined in Bell-Tilcock et al., (2020). Laminar sampling and manual measuring procedures for Red Grouper and Black Seabass were described in Vecchio and Peebles (2022).

We visually determined the pre- and post-apoptotic transition zones for each individual by recording the diameter of the last rigid post-apoptotic lamina. For species with multiple individuals, such as Leopard Sharks, Black Seabass, and Red Grouper, we estimated the mean pre- and post-apoptotic transition zone. Additionally, we normalized the diameter of each lamina to the capsule diameter for each individual, providing a relative proportion of the eye lens. This normalization allowed for anatomical comparisons both within and across taxa, accommodating fishes with varying eye lens sizes. In the case of Atlantic Salmon, eye lenses were normalized to the last semi-hydrated layer before the outermost hydrated laminae, so no pre- and post-apoptotic transition zone was determined. Eye lens laminae were either desiccated in a drying oven at 55 °C for 12 hours or frozen 8+ hours and then lyophilized overnight prior to weighing and preparing for SIA at their respective institutions.

4.2.2 Identification of Biomolecular Compounds

We evaluated the material composition of Chondrichthyan eye lenses using ATR-FTIR spectroscopy. In ATR-FTIR, infrared absorption bands identify and quantify organic functional groups and inorganic ions based on reflectance and vibrational movement of chemical bonds (Lee & Chapman, 1986). We collected ATR-FTIR spectra of Leopard Shark eye lens laminae (n individuals = 2; n laminae = 29) on a Bruker Vertex 70 Far-Infrared FTIR at the Nuclear Magnetic Resonance Facility of the University of California, Merced. Spectra were collected by smoothing 32 scans per sample from wavelength 400 – 4000 (cm^{-1}) at a resolution of 4 cm^{-1}. The FTIR spectra of isolated biomolecular compounds serve as a reference to determine individual compounds (Coates, 2000; Shurvell, 2006) and the size of absorbance of a band is proportional to the concentration of the associated compound (Grunenwald et al., 2014; Lebon et al., 2016).

Spectra were corrected by flattening expected baseline absorbance bands and fitting smooth spline curves to said baseline bands (Stuart, 2004; Trayler et al., 2023). We visually identified absorbance bands in ATR-FTIR spectra and detected each absorbance band's peak (Table 4.2). To compare shifts in specific absorption band peaks (i.e., amide I and amide II), we normalized each lamina's spectra to the maximum absorption value of the absorption band peak of interest. Additionally, due to the variability in the intensity of absorption band peaks (i.e., max absorbance) in raw FTIR spectra, peak-to-peak ratios are often used to standardize value comparisons between samples (Lebon et al., 2016). Because it was unclear which urea associated peak-to-peak ratio would be best to indicate urea concentration, we ratioed the urea absorbance band peak (~ wavelength 1449 cm^{-1}) to other individual identified peaks prominent in the spectra (e.g., amide III [1234 cm^{-1}], carboxylate [1392 cm^{-1}], amide II [1516 cm^{-1}], etc.) across all laminae. These potential

ratios were then compared to the C:N ratio and across the normalized diameter of the eye lens.

4.2.3 Effects of Urea Extraction

We investigated the impact of urea on stable isotope composition of eye lenses by analyzing samples before and after urea extraction, selecting individual laminae with sufficient material for subsampling. The urea extraction methodology is modified from Kim & Koch (2012) for Chondrichthyan muscle. Approximately 1 mg of lamina sample was weighed into a 2 mL microcentrifuge vial, then 1.5 mL of deionized (DI) water was added and the vial was vortexed for 10 seconds, sonicated for 30 minutes, and centrifuged for 3 minutes. The supernatant was removed using a glass transfer pipette and this extraction process was repeated 3x per sample. Because we did not know the urea content of lamina prior to urea extraction and to confirm the efficacy of this method for eye lens laminae, we analyzed the DI water extract for the outer lamina of three individual Leopard Sharks at two different sample sizes (5 and 10 mg). The DI water used to extract urea for each of the three rinses was transferred to a new microcentrifuge tube and stored at -20°C until analysis of urea concentration. The first, second, and third rinses were thawed overnight and individually analyzed at room temperature in triplicate via an EnzyChrom^{TM} urea assay kit III on a 96-well plate BioTek Synergy HTX Multimode Reader at the University of California, Merced. The urea concentrations of the samples (in μM) were determined using a calibration curve ($y = 0.0009x + 0.2818$) based on optical density measurements of urea standard solutions (0 μM, 300 μM, 600 μM, and 1000 μM) for each plate analysis, and then converted to ppm. Post-urea extracted laminae samples were frozen, then lyophilized overnight prior to SIA.

4.2.4 Stable Isotope Analysis

We analyzed eye lens laminae for carbon to nitrogen ratios by weight % (C:N), $\delta^{13}C$ values, and $\delta^{15}N$ values via continuous-flow Isotope Ratio Mass Spectrometer coupled to an Elemental Analyzer (EA-cf-IRMS) via Conflo IV. The $\delta^{13}C$ values are reported relative to Vienna Pee Dee Belemnites (VPDB; ‰) and $\delta^{15}N$ values are reported relative to V-AIR (‰). Leopard Shark, Sandbar Shark, and Zebra Shark laminae were analyzed at the Stable Isotope Ecosystem Laboratory of (SIELO) the University of California, Merced where data were corrected for linearity and drift using calibrated reference materials (USGS 40 [C:N mean = 4.28 ± 0.05 SD; $\delta^{13}C$ mean = -26.4 ± 0.1 ‰ SD, $\delta^{15}N$ mean = -4.5 ± 0.1 ‰ SD, n = 40]; USGS 41a [C:N mean = 4.30 ± 0.04 SD, $\delta^{13}C$ mean = 36.6 ± 0.1 ‰ SD, $\delta^{15}N$ mean = 47.6 ± 0.1 ‰ SD, n = 22]) and cross validated using an internal reference material (Mb Squid [C:N mean = 3.71 ± 0.05 SD, $\delta^{13}C$ mean = -18.8 ± 0.1 ‰ SD, $\delta^{15}N$ mean = 11.8 ± 0.1 ‰ SD, n = 14]). Red Grouper and Black Seabass laminae were analyzed at the University of South Florida College of Marine Science, where NIST 8573 and NIST 8574 L-glutamic acid standard reference materials were used for linearity and drift correction, while analytical precision was obtained using NIST 1577b bovine liver (C:N mean = 5.63 ± 0.05 SD, n = 28). Atlantic Salmon laminae were analyzed at the University of Southampton SEAPORT Stable Isotope Ratio Mass Spectrometry Laboratory, and data were corrected for linearity and

drift using calibrated reference materials (USGS 40 [C:N mean = 4.30 ± 0.07 SD, n = 26]; USGS 41a [C:N mean = 4.32 ± 0.04 SD, n = 25]).

4.2.5 Statistical Analyses

In this study, we performed all statistical analyses in R version 4.3.1 (R Core Team, 2023). We determined the effects of lipids and urea on the chemical composition of eye lens laminae with generalized additive models (GAMs) using the "mgcv" package (Wood, 2017). This approach was chosen due to nonlinear relationships between response variables (i.e., C:N ratio, FTIR peak ratio, estimated urea concentration, $\delta^{13}C$ difference, and $\delta^{15}N$ difference) and the two explanatory variables of normalized diameter (smooth term) and fish ID (random smooth effect). GAM assumptions were assessed via the "DHARMa" package (Hartig, 2022). In addition, we used a combination of linear regression models (LMs) in the "stats" package (R Core Team, 2023) and linear mixed models (LMMs) in the "lme4" package (Bates et al., 2015) to explore data with linear relationships, such as C:N ratio to urea peak-to-peak ratio and C:N ratio to urea concentration. Marginal (fixed effect only) and conditional (fixed and random effect) variance explained (R^2) was calculated for LMMs using the "Mumin" package (Bartoń, 2023). We tested assumptions of LMMs via the "DHARMa" package (Hartig, 2022) and found that for the C:N ratio to urea peak-to-peak ratio models of Urea:Carboxylate, Urea:Amide III, and Urea:Secondary Amide met the assumptions of normality and homoscedacity, whereas the models for Urea:Amide II and Urea:Saturated (both CH_2 and CH_3) did not. The model evaluations of C:N ratio to urea peak-to-peak ratio LMMs used Akaike Information Criterion (AIC) and the likelihood ratio test (LRT) via the "lmerTest" package (Kuznetsova et al., 2017). The Urea:Carboxylate, Urea:Amide III, and Urea:Secondary Amide models exhibited the best AIC scores (Supplemental 4.9.1, Table 4.4). The Urea:Amide II and Urea:Saturated models displayed low AIC scores alongside deviations from normality and homoscedasticity, prompting their exclusion from further analysis. Despite incorporating a random effect to accommodate multiple values per individual (i.e., fish ID), the best C:N ratio to urea peak-to-peak ratio model in terms of AIC included only fixed effects (Supplemental 4.9.1, Table 4.4). Consequently, we elected to solely present LM comparison results here (Table 4.3). Lastly, we used pairwise t-tests with a Bonferroni correction in the "stats" package (R Core Team, 2023) to compare means of urea concentration between DI water extract sample weight groups (i.e., 5 mg and 10 mg) for each rinse level (i.e., 1, 2, or 3). We also used pairwise t-tests to compare means of urea concentration between each combination of rinse pair (i.e., 1 vs 2, 2 vs 3, and 1 vs 3) for each level of DI water extract and sample weight groups (i.e., 5 mg or 10 mg).

4.3 Results

4.3.1 Elemental Composition Across the Lens

To our knowledge, there is no inter-taxa comparison of eye lens composition across laminae, which is a critical step in establishing SIA for comparative ecological studies. We observed clear differences in aqueous composition during laminar sampling across the eye lens, delineated by the inner, well-defined laminae (post-apoptotic zone) and the outer, yet-to-be-formed, hydrated laminae (pre-apoptotic zone; see Fig. 4.1). In

addition, there was a gradient of hydration observed for pre-apoptotic laminae from more to less hydration moving from outer to inner laminae (Fig. 4.1). For Leopard Sharks, the mean transition zone from post-apoptotic to pre-apoptotic occurred at 53% (± 4% SD) of the normalized eye diameter (Fig. 4.2A; dashed line). For Red Grouper and Black Seabass, the mean transition zone occurred at 68 % (± 8 % SD) and 71 % (± 9 % SD) of the eye lens, respectively (Fig. 4.2B; dashed lines). An accurate transition zone for the Atlantic Salmon eye lens was not calculated due to the data collected during sampling; the normalizing diameter was from the first rigid lamina for each individual rather than total capsule. The transition zone between pre- and post-apoptotic laminae may represent a change in the primary supply of biomolecules across the eye lens (Fig. 4.1C,D).

In this study, we observed a linear and slightly increasing trend in Teleost C:N ratios across laminae (no extraction or treatment; Fig. 4.2B). Explanatory variables accounted for some of the variance in the response variable (C:N ratio) for Red Grouper and Atlantic Salmon GAMs (R^2 = 0.65 and R^2 = 0.33, respectively). For both models, the explanatory variables of normalized diameter (smooth term) and fish ID (random smooth effect) were significant ($p < 0.001$ and $p < 0.001$, respectively). For Black Seabass, the explanatory variables explained a low amount of variance in the GAM (R^2 = 0.04), where the smooth term of normalized diameter was significant ($p < 0.001$), but fish ID (random smooth effect) was not significant ($p = 0.14$).

Conversely, Chondrichthyan C:N ratios in pre-urea extracted laminae exhibited a decreasing trend, notably at the pre- and post-apoptotic transition zone. A large extent of C:N ratio variance corresponded to explanatory variables in the Leopard Shark pre-extracted GAM (R^2 = 0.83; Fig. 4.2A). The smooth term of normalized diameter was significant ($p < 0.001$), but the random smooth effect of fish ID was not significant (p = 0.11). Following urea extractions, Leopard Shark C:N ratios resembled the Teleost trend, with explanatory variables accounting for a greater extent of variance (R^2 = 0.93; Fig. 4.2A). The Leopard Shark post-extracted GAM results indicated significance for both explanatory variables of normalized diameter (smooth term; $p < 0.001$) and fish ID (random smooth effect; $p < 0.001$). These findings highlight distinct patterns in C:N ratios between taxa and effects of urea extraction methods for Chondrichthyes.

4.3.2 ATR-FTIR of Eye Lens Laminae

We identified eight key absorption bands related to amino acids and urea in the ATR-FTIR spectra (Table 4.2). Each absorption band was exhibited across all laminae (Fig. 4.3A), but at varying intensities (i.e., peak). We found a shift in the normalized amide I absorption peak to lower wavelengths toward the outer pre-apoptotic laminae of the eye lens (Fig. 4.3B). Similarly, we found the formation of a doublet absorption peak for normalized amide II toward the outer pre-apoptotic laminae (Fig. 4.3C). These subtle changes in the amide I and II functional groups represent structural and biomolecular changes across eye lens laminae.

Peak-to-peak ratios can be an indicator for biomolecular concentration variability within tissues, such as urea levels across eye lens laminae, where the peak ratio of urea:carboxylate yielded the lowest AIC value (Table 4.3). The resulting LM depicted a robust negative linear trend between C:N and urea:carboxylate peak ratio (R^2 = 0.88, df =

27, $p < 0.001$; Fig. 4.4A). Informed by these outcomes, we opted to use the urea:carboxylate peak ratio in our GAM across the normalized diameter. Our analyses revealed an increase in urea:carboxylate absorbance peak ratio following the post- and pre-apoptotic transition zone (Fig. 4.4B). For the urea:carboxylate peak ratio GAM, the explanatory variables accounted for a large portion of the variance ($R^2 = 0.84$), with the smooth term of normalized diameter being statistically significant ($p < 0.001$) and the random smooth effect of fish ID was not significant ($p = 0.411$).

4.3.3 Urea Extraction and Quantification

Urea contains nitrogen and is known to affect nitrogen isotope composition in Chondrichthyan soft tissues; therefore, we quantified urea content to determine possible effects on eye laminae. Urea content was determined from assays on the first, second, and third DI water rinse extract of three individual Leopard Shark outer laminae samples with repetitions at two sample weights. There was no significant difference in pairwise t-tests between sample weight groups (i.e., 5 mg versus 10 mg) for rinses 1 and 3 ($p = 0.72$ and $p = 0.61$, respectively), but rinse 2 did indicate a significant mean difference ($p = 0.045$; Fig. 4.5A). The amount of urea removed with each sequential DI water rinse varied for both sample weights (Fig. 4.5A). We also found significant differences in means for the 5 mg sample weight group we between rinse 1 vs 2 ($p < 0.001$) and rinse 1 vs 3 ($p < 0.001$), but no significant difference between rinse 2 vs 3 ($p = 0.83$; Fig. 4.5A). Similarly, for the 10 mg sample weight group we found significant differences in means between rinse 1 vs 2 ($p = 0.02$) and rinse 1 vs 3 ($p = 0.01$), but no significant difference between rinse 2 vs 3 ($p = 0.07$; Fig. 4.5A).

We used the pre- and post- urea extracted laminae results to correlate urea content and C:N ratio, then estimate urea concentration across the normalized diameter of Chondrichthyan eye lenses. There was a linear relationship between urea concentration of DI water rinses (pre-extracted = 1st rinse urea concentration; post-urea extracted = 3rd rinse urea concentration) and C:N ratio (pre- and post-urea extracted eye laminae; Fig. 4.5B). For the urea concentration (ppm) LMM, the fixed effect (C:N ratio) and random effect (fish ID) explained a high proportion of variance (*marginal* $R^2 = 0.94$; *conditional* $R^2 = 0.96$). The estimated intercept (312.228) and C:N ratio coefficient (-93.728) from the LMM was then used to estimate urea content (ppm) for all Leopard Shark eye lens laminae based on pre-extraction C:N ratio (Fig. 4.5C). For the estimated urea (ppm) GAM, there was a high amount of variance explained by the response variables ($R^2 = 0.83$) with a significant effect of normalized diameter (smooth term; $p < 0.001$), but no significance of fish ID (random smooth effect; $p = 0.113$). These results are only estimate and should be interpreted with caution as urea assay concentrations for rinse 1 (5 mg sample mean = 1123.9 ± 155.0 μM; 10 mg sample mean = 1170.3 ± 247.0 μM) fell slightly outside of the range of calibration curve (0 – 1000 μM) in determining urea concentration.

4.3.4 Urea Effect on Stable Isotopes

We tested if urea presence in eye lens laminae of Chondrichthyans affects stable isotope values and found no effects for $\delta^{13}C$ values and negligible differences for $\delta^{15}N$ values. The $\delta^{13}C$ differences of post-urea extracted minus pre-urea extracted samples

resulted in a linear trend near zero, with the GAM fit falling within the 95% confidence interval of $\delta^{13}C$ instrument error (± 0.2 ‰; Fig. 4.6A). In addition, the explanatory variables for the $\delta^{13}C$ difference GAM accounted for little variance in C:N ratio (R^2 = 0.03), and neither the smooth term of normalized diameter and random smooth effect of fish ID had a significant effect (p = 0.275 and p = 0.226, respectively). The $\delta^{15}N$ difference of post- urea extracted minus pre-urea extracted samples increased at the pre- and post-apoptotic transition zone, but the GAM fit also fell within the 95% confidence interval of $\delta^{15}N$ instrument error (± 0.2 ‰; Fig. 4.6B). The $\delta^{15}N$ difference GAM results indicate the explanatory variables accounted for low variance in C:N ratio (R^2 = 0.03), similar to the $\delta^{13}C$ difference GAM. The explanatory variables of normalized diameter and random smooth effect of fish ID also did not have a significant effect (p = 0.079 and p = 0.089, respectively). Although the $\delta^{15}N$ difference GAM fit increases across the post- and pre-apoptotic transition zone, the magnitude of change is muted compared to what is observed without urea extraction (Fig. 4.6B) and the C:N ratio pattern is similar between Teleost eye laminae and Chondrichthyan eye laminae after urea extraction.

4.4 Discussion

Eye lens laminae are continually synthesized throughout an organism's lifetime and recent studies analyzed the stable isotope composition of this proteinaceous substrate from fish to elucidate lifetime patterns of diet and movement. Unlike Teleost fishes, the body tissues of Chondrichthyans contain urea, which has high nitrogen content and can affect $\delta^{15}N$ values (Kim & Koch, 2012). Here, we found that patterns of C:N ratios for Chondrichthyan eye lens laminae differed from those of several Teleost species, with substantially lower C:N ratios in the outer laminae of Chondrichthyan eye lenses. Concurrently, we observed a hydrated pre-apoptotic region in Leopard Shark eye lens laminae between the ocular capsule and first rigid laminae (~ 50% of eye lens diameter) with structural and biochemical differences in the pre-and post-apoptotic zones. Finally, our results indicate that although urea is present, primarily within the pre-apoptotic zone, there is a negligible effect on stable isotope values and DI water rinses minimize potential interference with C:N ratio. These results support the use of eye lenses in fishes as a chronological tissue for SIA, as well as highlighting the potential of Chondrichthyan eye lenses in future ecological studies of life history.

4.4.1 Chondrichthyes C:N Patterns Differ from Teleost

The eye lenses of Teleost fishes, across a range of habitats and life-history patterns, exhibit remarkably constant C:N ratios. All sampled Teleost species demonstrated two distinct sections of the eye lens, a pre-apoptotic and a post-apoptotic section, but the C:N ratios remained relatively consistent from inner to outer laminae (Fig. 4.2B). This result contrasts sharply with the three Chondrichthyan species tested, in which C:N ratio declined precipitously across the diameter, with the most recently formed, outer-most layers having the lowest C:N ratios (Fig. 4.2A).

The content of various organic biomolecules (i.e., amino acids, urea, lipids, etc.) affects the elemental and isotopic composition of substrates. For example, lipids have high carbon content from the glycerol group (CH_2OH-$CHOH$-CH_2OH) and fatty acid tails (i.e., carboxylic acid [-CO_2H] attached to aliphatic chain [-CH_3, -C_2H_5, -C_3H_7, etc.]).

In addition, the metabolic process of lipogenesis (i.e., fatty acid and subsequent triglyceride synthesis) discriminates against ^{13}C and therefore lipids are ^{12}C- enriched relative to protein; consequently higher lipid content affects the C:N ratio and $\delta^{13}C$ values of tissue (Post et al., 2007). While lipids makeup ~ 2 % of the pre-apoptotic portion of the eye lens (by weight) in some fish (Kiss et al., 2010), we did not observe an increase in eye lens laminae C:N ratios greater than $3.87_{\text{weight \%}}$ ($> 3.32_{\text{atomic mass}}$), which is the threshold for lipid effect on $\delta^{13}C$ values (Post et al., 2007). Therefore, lipids are unlikely to be present in high enough concentrations to affect elemental and isotopic composition of the eye lens of fishes.

Originating primarily as a waste byproduct of protein metabolism in the liver, urea serves an additional role in Chondrichthyans by aiding in osmotic balance regulation (Hazon et al., 2003). In contrast to the lipid-related increase in C:N ratio, the C:N ratio of proteinaceous tissues decreases with high urea content. This effect stems from urea's high nitrogen content, characterized by two amino groups ($-NH_2$) for every carbonyl group (-C=O) (Kim & Koch, 2012). Our results show decreasing C:N ratio across the normalized diameter of the eye lens in Chondrichthyans with a sharp decline near the pre- and post-apoptotic transition zone. This pattern suggests urea presence in the living pre-apoptotic tissue before it undergoes partial apoptosis, and subsequent removal of living organelles. In contrast, there was no such change observed in any of the Teleost species sampled, regardless of life history strategy (i.e., anadromy). The change in C:N ratio between pre- and post- urea extracted Leopard Shark laminae confirms the removal of some free nitrogenous biomolecular species, which is likely urea. Although urea has not been documented in the eye lenses of any species, its prevalence in shark tissues, including plasma and muscle (Kim & Koch, 2012), suggests it may be ubiquitous in soft tissues. Given the likelihood of urea being present in the eye lens laminae of Chondrichthyans in concentrations sufficient enough to alter C:N ratios, there is potential for urea to also influence isotopic values.

4.4.2 Structural Makeup of Chondrichthyes Eye Lens Laminae

The primary component of eye lens laminae is crystallin protein (α or $\beta\gamma$ superfamily) with a beta-sheet secondary structures (Slingsby et al., 1999). The presence of crystallin protein in the beta-sheet secondary structure of Chondrichthyes eye laminae were confirmed with ATR-FTIR spectroscopy of the amide I absorption band ~ 1630 cm^{-1} (between 1620 and 1640 cm^{-1}; Fatima et al., 2010; Surewicz et al., 1993) and observed throughout the normalized diameter of the Leopard Shark eye lens (Fig. 4.3A,B). Additionally, the primarily proteinaceous beta-sheet secondary structure was reaffirmed with amide III absorption band ~ 1240 cm^{-1} (Fig. 4.3A; Singh et al., 1993). The presence of these functional groups confirms the presence of crystallin protein across both pre- and post-apoptotic laminae, including hydrated portions in the pre-apoptotic laminae.

During laminar sampling, we found a distinct difference in degree of hydration between the outer hydrated pre-apoptotic laminae and the inner rigid post-apoptotic laminae. The degree of hydration coincided with a shift in the amide I peak; inner post-apoptotic laminae occurring at higher wavenumbers (~ 1630 cm^{-1}), while outer pre-apoptotic laminae occurring at lower wavenumbers (~ 1620 cm^{-1}; Fig. 4.3B). This shift in

amide I is attributed to changes in protein secondary structure from more complex twisted sheets (longer and fewer strands) to more planar sheets (shorter and more strands; Fatima et al., 2010). In addition, the unfolding of eye lens crystallin proteins from complex and twisted to more planar sheets corresponds with a double, bimodal peak (~ 1517 and 1535 cm^{-1}) in the amide II region of FTIR spectra (Fatima et al., 2010), similar to what we observe in the outer pre-apoptotic laminae (Fig. 4.3C). While crystallin protein across the eye lens laminae is primarily in the form of beta-sheets, the outer pre-apoptotic laminae likely have a higher proportion of shorter and more planar sheets. These shorter structures may not be able to form compact bonds with adjacent lens fibers, allowing both water molecules and small biomolecules to disperse between the crystallin protein chains. This relationship would explain the correlation between high degree of hydration and changes to C:N ratio in the outer pre-apoptotic laminae.

Beyond the shift in protein secondary structure and interstitial spacing across the eye lens, the change in C:N ratio suggests differences in biomolecular composition. As indicators of compositional shift, absorption band peak-to-peak ratios were coupled with C:N ratios to serve as a proxy for urea concentration within the eye lens. We confirmed urea presence with ATR-FTIR spectroscopy (absorption band peak ~ 1447 $cm^{-1}$and observed a significant negative linear relationship between the urea:carboxylate peak ratio and C:N ratio (Fig. 4.4A). The best peak-to-peak ratio model of urea to carboxylate ($-COO^-$) normalizes the relative amount of urea to the ionized form of carboxylic acids (-COOH), which is consistently present in amino acids, the primary constituents of crystallin proteins. The peak-to-peak ratio of urea to amide III is similar in terms of AIC and variance explained, likely because of the Amide III peak's association with proteins (Singh et al., 1993). The correlation between the urea:carboxylate peak ratio and C:N ratio suggests that higher urea concentrations are associated with lower C:N ratios in eye lens laminae (Fig. 4.4A). Consequently, we observed an increase in the urea:carboxylate peak ratio (i.e., urea concentration proxy) in pre-apoptotic laminae (Fig. 4.4B), suggesting that higher concentrations of urea are accommodated by the expansion of interstitial spacing across the eye lens. Thus, urea is likely diffused from the aqueous humor, crossing the capsule, where it accumulates in the pre-apoptotic interstitial space, and the majority of urea is subsequently forced out of the interstitial space as crystallin protein chains become tightly compact during partial apoptosis in the eye lens of Chondrichthyes (Fig. 4.1B-D).

4.4.3 Urea removal and effects on laminae elemental composition

Urea is water soluble and published extraction methods from proteinaceous tissues are relatively straightforward with rinses in DI water. The high C:N ratio and ATR-FTIR results in the outermost laminae confirmed the presence of urea, which we reaffirmed with urea assays of DI water from rinses. The effectiveness of sonication and rinses in DI water to remove urea is attributed to its chemical composition of two amino groups that are hydrophilic. The multiple sonication and rinses with DI water significantly reduced urea concentration in both laminae sample weight groups (i.e., 5 mg and 10 mg) (Fig. 4.5A). Our results suggest that one rinse is needed to adequately remove urea from Chondrichthyan eye lens laminae samples at 5 mg or less, while at least two rinses are needed for 10 mg samples. Because the outermost pre-apoptotic laminae have

the highest concentration of urea, post-apoptotic laminae may need less rinses to remove urea.

The concentration of urea likely varies across Chondrichthyan eye lens laminae. Although urea assays were only conducted on DI rinses of the outermost pre-apoptotic laminae, we found a strong negative linear relationship between the C:N ratio and the corresponding urea concentration of these laminae (Fig. 4.5B). Having previously established the correlation between the urea:carboxylate peak ratio and C:N ratio (Fig. 4.4A,B), we can infer the urea concentration (in ppm) for all pre-urea extracted Leopard Shark laminae through the linear relationship: estimated urea (ppm) = 312.228 – [93.728 * C:N ratio](Fig. 4.5B). This estimation revealed a doubling in urea concentration from post-apoptotic laminae (~ 30 ppm) to pre-apoptotic laminae (~ 70 ppm; Fig. 4.5C). We note this pattern may be specific to Leopard Sharks as the urea content within Chondrichthyan tissues vary with physiological factors influenced by biological and environmental conditions (Hazon et al., 2003). Pelagic Chondrichthyans, such as the Sandbar and Zebra Shark in this study, inhabit more saline environments and often exhibit higher urea concentrations in their tissues to retain water for osmotic balance. In contrast, Chondrichthyans inhabiting estuaries, such as Leopard Sharks, may regulate their urea concentration depending on the seasonal or tidal oscillations of salinity (Hazon et al., 2003). However, the Sandbar and Zebra Shark eye lens C:N ratios decreased similarly across the eye diameter compared to the Leopard Shark (Fig. 4.2A). We suggest additional species should be tested to ensure that the patterns of urea incorporation hold for a wide variety of Chondrichthyan taxa, but our results confirm the presence of urea and influence on C:N ratio in Chondrichthyan laminae.

4.4.4 Urea Levels Too Small for Isotopic Effect

High concentrations of urea in Chondrichthyan tissues have previously resulted in altered $\delta^{15}N$ values (Kim & Koch, 2012). Urea is a waste byproduct enriched in ^{14}N and has lower $\delta^{15}N$ values compared to proteinaceous tissues. In Chondrichthyan eye lens laminae, we observed the concentration of urea to differ between pre- and post-apoptotic sections. Urea assays on DI water rinses of Leopard Shark eye lenses indicate urea levels of ~ 30 – 70 ppm, which are high enough to affect C:N ratios; however, the $\delta^{15}N$ difference between post- and pre-urea extracted samples across the normalized diameter was minor, with the model fit falling within the 95 % confidence interval of mean analytical error (Fig. 4.6B). While we observe an increase in the $\delta^{15}N$ difference at the pre- and post-apoptotic transition zone, similar to what we would expect with the removal of urea from pre-apoptotic laminae, the concentration of urea is too low to have a meaningful isotopic effect. Additionally, the $\delta^{13}C$ difference between post- and pre-urea extracted samples across the normalized diameter was also negligible, with the model fit also falling within the 95 % confidence interval of mean analytical error (Fig. 4.6A). It is important to note that although the model fits fell within the 95% confidence interval of analytical error for both $\delta^{13}C$ and $\delta^{15}N$ difference, individual values displayed variability beyond the 95% confidence interval of analytical error for both parameters (Fig. 4.6A,B). The C:N ratios of post-urea extracted laminae suggest adequate urea removal and the variation is likely due to isotopic variation of individual lens fibers within the larger lamina analyzed. Therefore, the removal of urea from Chondrichthyan eye lens laminae

may not be necessary for accurate stable isotope analyses. It is also important to emphasize that our stable isotope results before and after urea extraction pertain exclusively to Leopard Sharks captured in estuarine waters, which could potentially have lower urea concentrations compared to other pelagic Chondrichthyans (Hazon et al., 2003). Thus, we suggest future Chondrichthyan eye lens laminae studies perform similar tests to determine species specific urea concentration effects on stable isotope values. Urea extraction from Chondrichthyan eye lens laminae is suggested to foster inter taxa comparison (i.e., Chondrichthyan vs Teleost) so material of common chemical composition is analyzed for SIA.

4.5 Conclusion

Eye lens laminae have been validated as a viable tissue type for SIA in Teleost fishes, but our study is the first to examine eye lens laminae series from Chondrichthyans that span post- and pre-apoptotic layers. Our study collected eye lens laminae from three Chondrichthyan and three Teleost fish species to compare C:N ratio. We showed that the two groups differed in C:N ratio trends across the eye lens. While Teleost fishes of varying life histories showed consistent, linear trends in C:N ratio across the eye lens, three species of Chondrichthyans showed precipitous declines. Urea in the Chondrichthyan pre-apoptotic portion of the eye lens is likely the cause of differing chemical composition, with intercellular urea responsible for the observed C:N ratios. Although DI water rinses are an effective urea removal method from Chondrichthyan eye lens laminae, we did not observe a meaningful isotopic effect in Leopard Shark, which inhabits estuarine waters. We suggest testing pre- and post-extracted laminae in pelagic sharks, as well as urea extracting Chondrichthyan eye lens laminae when comparing between taxa. Our findings highlight the importance of understanding the taxa-specific differences in elemental components of eye lens laminae for confidence in ecological interpretation using SIA.

4.6 References

Andley, U. P. (2008). The Lens Epithelium: Focus on the expression and function of the alpha-crystallin chaperones. Int J Biochem Cell Biol, 40(3), 317–323. https://www.ncbi.nlm.nih.gov/pmc/articles/PMC3624763/pdf/nihms412728.pdf

Bartoń, K. (2023). MuMIn: Multi-Model Inference (1.47.5). The Comprehensive R Archive Network.

Bates, D., Mächler, M., Bolker, B., & Walker, S. (2015). Fitting Linear Mixed-Effects Models Using lme4. Journal of Statistical Software, 67(1), 1–48. https://doi.org/10.18637/jss.v067.i01

Bell-Tilcock, M., Jeffres, C. A., Rypel, A. L., Sommer, T. R., Katz, J. V. E., Whitman, G., & Johnson, R. C. (2020). Advancing diet reconstruction in fish eye lenses. Methods in Ecology and Evolution, February 2021. https://doi.org/10.1111/2041-210X.13543

Berman, E. R. (1991). Biochemistry of the Eye. Plenum Press, 476.

Carleton, S. A., & Del Rio, C. M. (2005). The effect of cold-induced increased metabolic rate on the rate of 13C and 15N incorporation in house sparrows (Passer domesticus). Oecologia, 144(2), 226–232. https://doi.org/10.1007/s00442-005-0066-8

Coates, J. (2000). Infrared spectral interpretation: A systematic approach. In Encyclopedia of Analytical Chemistry (pp. 10815–10837). https://doi.org/10.1201/9780203750841

DeNiro, M. J., & Epstein, S. (1978). Influence of diet on the distribution of carbon isotopes in animals. Geochemica et Cosmochimica Acta, 42, 495–506. https://doi.org/10.1002/mop.25285

Fatima, U., Sharma, S., & Guptasarma, P. (2010). Structures of Differently Aggregated and Precipitated Forms of γB Crystallin: An FTIR Spectroscopic and EM Study. Protein & Peptide Letters, 17(9), 1155–1162. https://doi.org/10.2174/092986610791760414

Gleiss, A. C., Potvin, J., & Goldbogen, J. A. (2017). Physical trade-offs shape the evolution of buoyancy control in sharks. Proceedings of the Royal Society B: Biological Sciences, 284(1866). https://doi.org/10.1098/rspb.2017.1345

Groen, H., & Roberts, K. J. (2004). An examination of the crystallization of urea from supersaturated aqueous and aqueous-methanol solutions as monitored in-process using ATR FTIR spectroscopy. Crystal Growth and Design, 4(5), 929–936. https://doi.org/10.1021/cg030038y

Grunenwald, A., Keyser, C., Sautereau, A. M., Crubézy, E., Ludes, B., & Drouet, C. (2014). Revisiting carbonate quantification in apatite (bio)minerals: A validated FTIR methodology. Journal of Archaeological Science, 49(1), 134–141. https://doi.org/10.1016/j.jas.2014.05.004

Hartig, F. (2022). DHARMa: Residual Diagnostics for Hierarchical (Multi-Level / Mixed) Regression Models. http://florianhartig.github.io/DHARMa/

Hazon, N., Wells, A., Pillans, R. D., Good, J. P., Anderson, W. G., & Franklin, C. E. (2003). Urea based osmoregulation and endocrine control in elasmobranch fish with special reference to euryhalinity. Comparative Biochemistry and Physiology - B Biochemistry and Molecular Biology, 136(4), 685–700. https://doi.org/10.1016/S1096-4959(03)00280-X

Horwitz, J. (2003). Alpha-crystallin. Experimental Eye Research, 76(2), 145–153. https://doi.org/10.1016/S0014-4835(02)00278-6

Kim, Sora L., & Koch, P. L. (2012). Methods to collect, preserve, and prepare elasmobranch tissues for stable isotope analysis. Environmental Biology of Fishes, 95(1), 53–63. https://doi.org/10.1007/s10641-011-9860-9

Kim, Sora Lee, Casper, D. R., Galván-Magaña, F., Ochoa-Díaz, R., Hernández-Aguilar, S. B., & Koch, P. L. (2012). Carbon and nitrogen discrimination factors for elasmobranch soft tissues based on a long-term controlled feeding study. Environmental Biology of Fishes, 95(1), 37–52. https://doi.org/10.1007/s10641-011-9919-7

Kim, Sora Lee, Del Rio, C. M., Casper, D., & Koch, P. L. (2012). Isotopic incorporation rates for shark tissues from a long-Term captive feeding study. Journal of Experimental Biology, 215(14), 2495–2500. https://doi.org/10.1242/jeb.070656

Kiss, A. J., Devries, A. L., & Morgan-Kiss, R. M. (2010). Comparative analysis of crystallins and lipids from the lens of Antarctic toothfish and cow. Journal of Comparative Physiology B: Biochemical, Systemic, and Environmental Physiology, 180(7), 1019–1032. https://doi.org/10.1007/s00360-010-0475-9

Kuznetsova, A., Brockhoff, P. B., & Christensen, R. H. B. (2017). lmerTest Package: Tests in Linear Mixed Effects Models. Journal of Statistical Software, 82(13), 1–26. https://doi.org/10.18637/jss.v082.i13

Lebon, M., Reiche, I., Gallet, X., Bellot-Gurlet, L., & Zazzo, A. (2016). Rapid quantification of bone collagen content by ATR-FTIR spectroscopy. Radiocarbon, 58(1), 131–145. https://doi.org/10.1017/RDC.2015.11

Lee, D. C., & Chapman, D. (1986). Infrared spectroscopic studies of biomembranes and model membranes. Bioscience Reports, 6(3), 235–256. https://doi.org/10.1007/BF01115153

Lin, S. Y., Li, M. J., Liang, R. C., & Lee, S. M. (1998). Non-destructive analysis of the conformational changes in human lens lipid and protein structures of the immature cataracts associated with glaucoma. Spectrochimica Acta - Part A: Molecular and Biomolecular Spectroscopy, 54(10), 1509–1517. https://doi.org/10.1016/S1386-1425(98)00175-9

Nicol, J., Colin, A., & Somiya, H. (1989). The Eyes of Fishes. Oxford University Press.

Parker, F. S. (1971). Applications of Infrared Spectroscopy in Biochemistry, Biology, and Medicine. Plenum Press. https://doi.org/10.1007/978-1-4684-1872-9

Post, D. M. (2002). Using stable isotopes to estimate trophic position: Models, methods, and assumptions. Ecology, 83(3), 703–718. https://doi.org/10.1890/0012-9658(2002)083[0703:USITET]2.0.CO;2

Post, D. M., Layman, C. A., Arrington, D. A., Takimoto, G., Quattrochi, J., & Montaña, C. G. (2007). Getting to the fat of the matter: Models, methods and assumptions for dealing with lipids in stable isotope analyses. Oecologia, 152(1), 179–189. https://doi.org/10.1007/s00442-006-0630-x

Quaeck-Davies, K., Bendall, V. A., MacKenzie, K. M., Hetherington, S., Newton, J., & Trueman, C. N. (2018). Teleost and elasmobranch eye lenses as a target for life-history stable isotope analyses. PeerJ, 2018(6), 1–26. https://doi.org/10.7717/peerj.4883

R Core Team. (2023). R: A Language and Environment for Statistical Computing. https://www.r-project.org/

Schneider, C. A., Rasband, W. S., & Eliceiri, K. W. (2012). NIH Image to ImageJ: 25 years of image analysis. Nature Methods, 9(7), 671–675. https://doi.org/10.1038/nmeth.2089

Shurvell, H. F. (2006). Spectra– Structure Correlations in the Mid- and Far-Infrared. In Handbook of Vibrational Spectroscopy. https://doi.org/10.1002/0470027320.s4101

Simpson, S. J., Sims, D. W., Trueman, C. N., Simpson, S. J., Sims, D. W., & Trueman, C. N. (2019). Ontogenetic trends in resource partitioning and trophic geography of sympatric skates (Rajidae) inferred from stable isotope composition across eye lenses. 624.

Singh, B. R., Deoliveira, D. B., Fu, F., & Fuller, M. P. (1993). Fourier transform infrared analysis of amide III bands of proteins for the secondary structure estimation. SPIE, Biomolecular Spectroscopy III, 1890, 47–55.

Slingsby, Christine; Clout, N. J. (1999). Structure of the crystallins. Eye, 13, 395–402. https://doi.org/https://doi.org/10.1038/eye.1999.113

Stuart, B. H. (2004). Infrared Spectroscopy: Fundamentals and Applications. In Infrared Spectroscopy: Fundamentals and Applications (Vol. 8). https://doi.org/10.1002/0470011149

Surewicz, W. K., Mantsch, H. H., & Chapman, D. (1993). Determination of Protein Secondary Structure by Fourier Transform Infrared Spectroscopy: A Critical Assessment. Biochemistry, 32(2), 389–394.

Tieszen, L. L., Boutton, T. W., Tesdahl, K. G., & Slade, N. A. (1983). Fractionation and turnover of stable carbon isotopes in animal tissues: Implications for δ13C analysis of diet. Oecologia, 57(1–2), 32–37. https://doi.org/10.1007/BF00379558

Trayler, R. B., Landa, P. V., & Kim, S. L. (2023). Evaluating the efficacy of collagen isolation using stable isotope analysis and infrared spectroscopy. Journal of Archaeological Science, 151(September 2022), 105727. https://doi.org/10.1016/j.jas.2023.105727

Tzadik, O. E., Curtis, J. S., Granneman, J. E., Kurth, B. N., Pusack, T. J., Wallace, A. A., Hollander, D. J., Peebles, E. B., & Stallings, C. D. (2017). Chemical archives in fishes beyond otoliths: A review on the use of other body parts as chronological recorders of microchemical constituents for expanding interpretations of environmental, ecological, and life-history changes. Limnology and Oceanography: Methods, 15(3), 238–263. https://doi.org/10.1002/lom3.10153

Vecchio, J. L., & Peebles, E. B. (2020). Spawning origins and ontogenetic movements for demersal fishes: An approach using eye-lens stable isotopes. Estuarine, Coastal and Shelf Science, 246(September), 107047. https://doi.org/10.1016/j.ecss.2020.107047

Vecchio, J. L., & Peebles, E. B. (2022). Lifetime-scale ontogenetic movement and diets of red grouper inferred using a combination of instantaneous and archival methods. Environmental Biology of Fishes, 105(12), 1887–1906. https://doi.org/10.1007/s10641-022-01210-2

Wallace, A. A., Hollander, D. J., & Peebles, E. B. (2014). Stable isotopes in fish eye lenses as potential recorders of trophic and geographic history. PLoS ONE, 9(10). https://doi.org/10.1371/journal.pone.0108935

Weidel, B. C., Carpenter, S. R., Kitchell, J. F., & Vander, M. J. (2011). Rates and components of carbon turnover in fish muscle : insights from bioenergetics models and a whole-lake 13 C addition. Canadian Journal of Fisheries and Aquatic Sciences, 399, 387–399. https://doi.org/10.1139/F10-158

Wood, S. N. (2017). Generalized Additive Models: An Introduction with R (Second).

4.7 Tables

Table 4.1: List of all species, number of individuals, and locality sampled in Chapter 3.

Common Name	Scientific Name	Taxonomic Group	Individuals	Locality
Leopard Shark	*Triakis semifasciata*	Chondrichthyes	9	South San Francisco Estuary, California, USA
Sandbar Shark	*Carcharhinus plumbeus*	Chondrichthyes	1	Captive; Mississippi Aquarium, Mississippi, USA
Zebra Shark	*Stegostoma tigrinum*	Chondrichthyes	1	Captive; Mississippi Aquarium, Mississippi, USA
Black Seabass	*Centropristis striata*	Teleostei	12	Eastern Gulf of Mexico, Florida, USA
Red Grouper	*Epinephelus morio*	Teleostei	12	Eastern Gulf of Mexico, Florida, USA
Atlantic Salmon	*Salmo salar*	Teleostei	12	Six rivers in the United Kingdom – Tweed, North Tyne, Shin, Oykel, Deveron, and Frome

Table 4.2: Attenuated total reflectance fourier transform infrared (ATR-FTIR) spectroscopy absorption bands identified.

Functional Group	Mean Peak Wavenumber (cm^{-1})	Literature Wavenumber Range (cm^{-1})	Description	Citation
Amide III	1234	1200 – 1350	N–H bending with C–N stretching; C–H and N–H deformation	(Singh et al., 1993)
Carboxylate	1392	1310 – 1410	COO^- symmetric stretch	(Lin et al., 1998; Parker, 1971; Shurvell, 2006)
Urea	1450	1446 – 1468	Possible N–H bending	(Groen & Roberts, 2004)
Amide II	1516	1480 – 1580	C–N stretch coupled to N–H bending; $N–H_3^+$ deformation	(Shurvell, 2006; Singh et al., 1993)
Amide I	1628	1630 – 1680	C=O stretch coupled to C–N stretch and N–H bending	(Shurvell, 2006)
Saturated Compounds	2931 and 2966	~ 2930 – 2960	Doublet peak: $C–H_2$ stretch and $C–H_3$ antisymmetric stretch	(Shurvell, 2006)
Secondary Amide	3262	3250 – 3300	Broad band N–H stretch; proteins and polypeptides	(Shurvell, 2006)

Note: Meak Peak wavenumber is the mean wavenumber at maximum absorbance across all laminae. The saturated compounds functional group has two linked absorption bands (doublet) in the same region.

Table 4.3: C:N ratio versus peak-to-peak ratio linear regression model selection.

Model	AIC	Edf	R^2	P value
C:N ~ Peak Ratio (Urea:Carboxylate)*	-124.8	27	0.88	< 0.001
C:N ~ Peak Ratio (Urea:Amide III)	-124.2	27	0.88	< 0.001
C:N ~ Peak Ratio (Urea:Secondary Amide)	-80.3	27	0.43	0.001

Note: Akaike Information Criterion (AIC) was used to determine model of best fit (*).

4.8 Figures

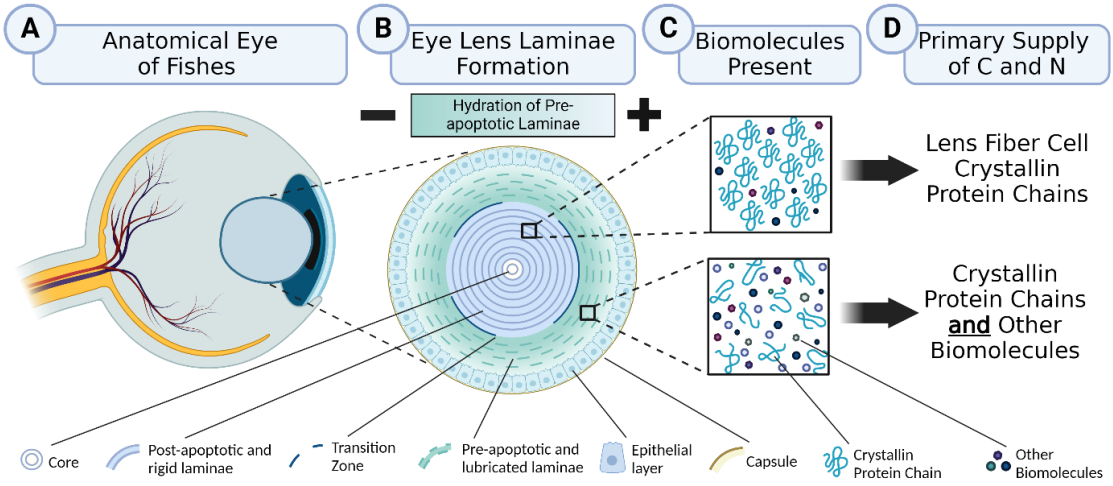

Figure 4.1: Diagram of eye lens layer (laminae) formation and possible biomolecular supply of carbon and nitrogen to tissue structure: A) Generalized anatomical fish eye, with spherical eye lens; B) Eye lens laminae formation with labeled anatomical features from inward to outward (eye lens core, post-apoptotic laminae, pre- and post-apoptotic transition zone, gradient of hydration in pre-apoptotic laminae, epithelial layer, and capsule); C) Labeled biomolecules present in the pre-apoptotic laminae and post-apoptotic laminae (crystallin protein chains and other biomolecules); D) Primary supply of carbon and nitrogen in the pre-apoptotic laminae (Lens fiber cell crystallin protein chains) and post apoptotic laminae (crystallin protein chains and other biomolecules).

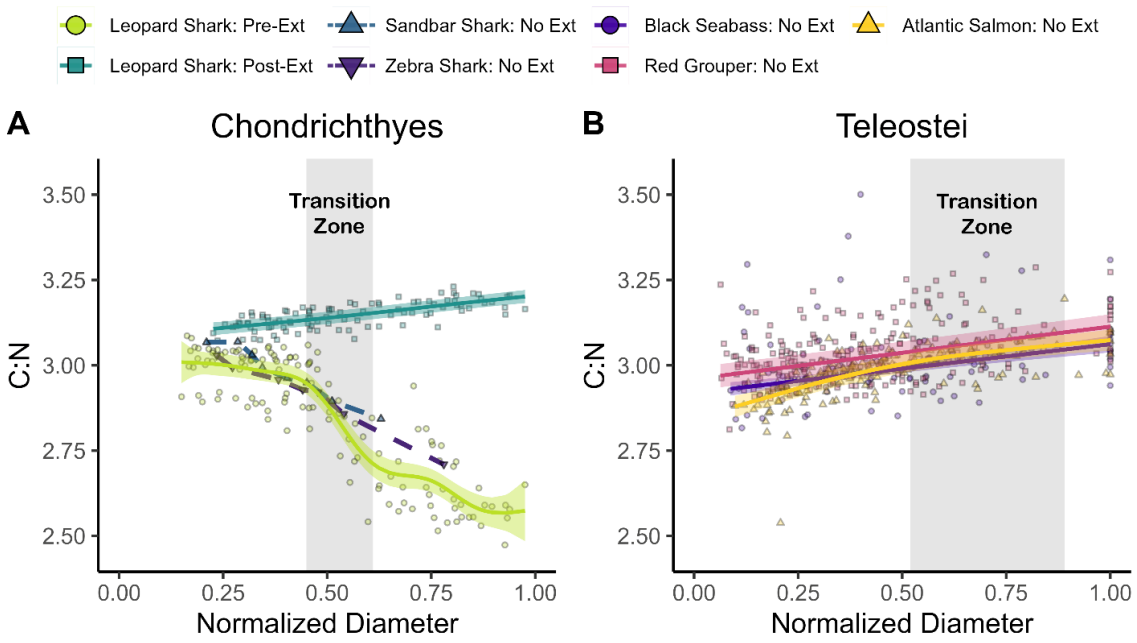

Figure 4.2: Carbon to nitrogen ratios (C:N) vary across the normalized diameter of (A) Chondrichthyan and (B) Teleost fishes eye lens laminae. For Leopard Sharks, "Pre-Ext" indicated C:N ratios pre-urea extraction, while "Post-Ext" indicates C:N ratio post-urea extraction. All colored solid lines are GAM smooth mean fit and colored shaded region is the 95 % confidence intervals around the fit for each species. Dashed lines represent line plots of species with one individual (e.g., Sandbar and Zebra Shark). Grey shaded region indicates 95 % confidence interval around mean pre- and post-apoptotic transition zone (A = Leopard Sharks only; B = min and max of both Black Seabass and Red Grouper).

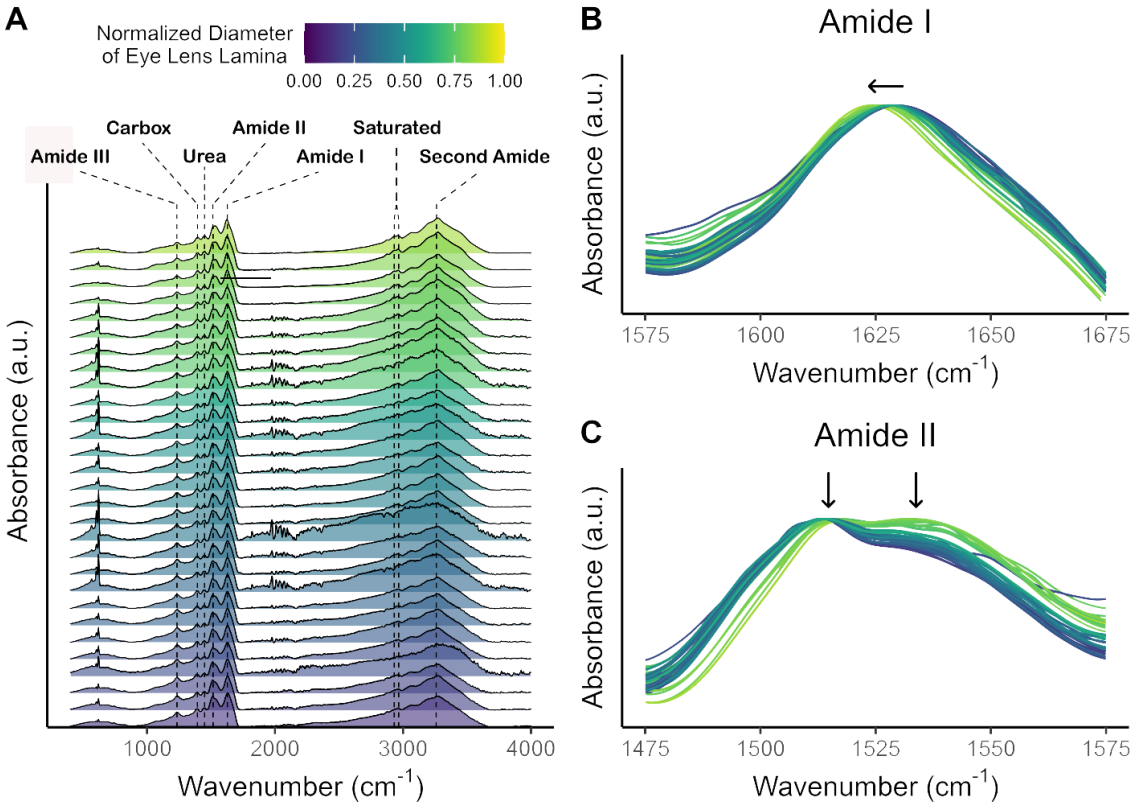

Figure 4.3: Amino acid and urea peak absorption bands identified with ATR-FTIR spectra of eye lens laminae from the core (purple) to outer (yellow) laminae. A) Absorption spectra in arbitrary units (Absorption a.u.) across wavelengths (400 – 4000 cm^{-1}), with dashed line indicating mean wavelength at absorption band peak for all laminae analyzed. B) Amide I absorption band spectra in arbitrary units (Absorption a.u.) across wavelengths (1575 – 1675 cm^{-1}) normalized to the maximum absorption value of the amide I peak for each lamina, with arrow indicating a shift from higher to lower wavelengths at the amide I peak. C) Amide II absorption band spectra in arbitrary units (Absorption a.u.) across wavelengths (1475 – 1575 cm^{-1}) normalized to the maximum absorption value of the amide II peak for each lamina, with arrows indicating doublet formation in outer pre-apoptotic laminae. Individual laminae of two Leopard Sharks are represented here.

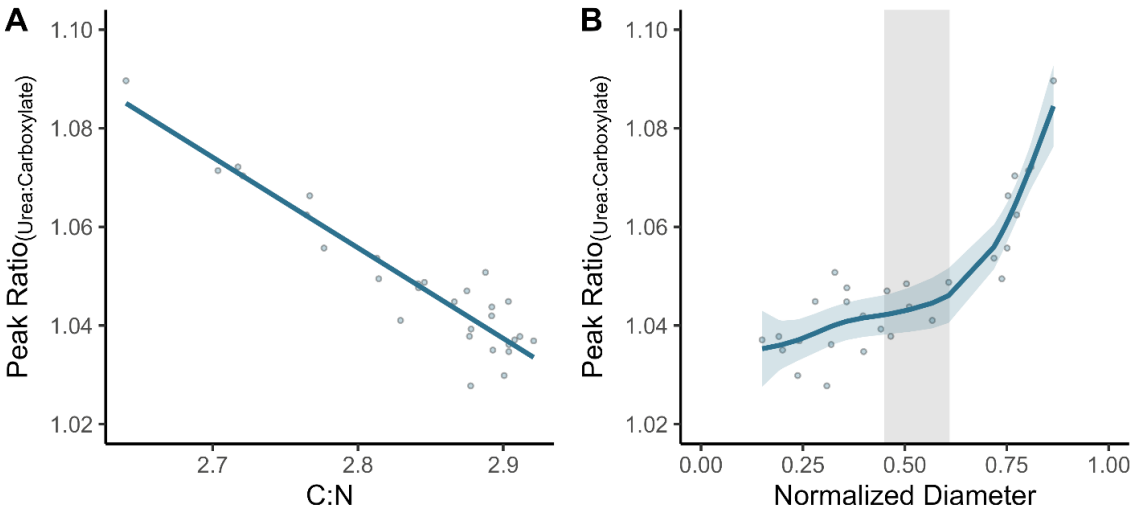

Figure 4.4: Leopard Shark laminae (A) Linear regression of the urea:carboxylate peak ratio versus carbon to nitrogen ratio (C:N; R^2 = 0.88) and (B) GAM smooth curve of the urea:carboxylate peak ratio across the normalized diameter of eye lens laminae. Grey shaded region representing the 95 % confidence interval around the pre- and post-apoptotic transition zone.

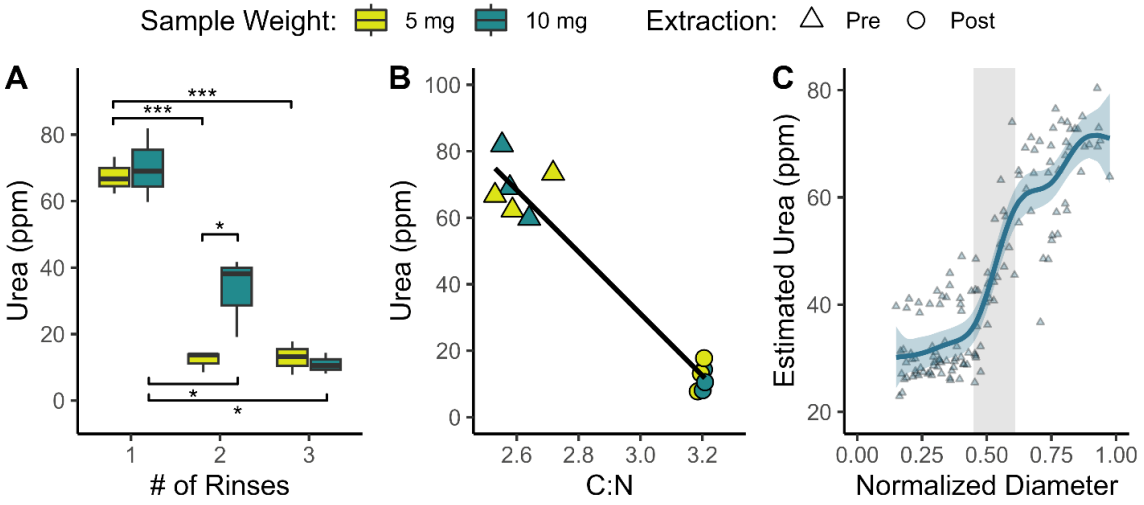

Figure 4.5: Boxplots of urea (ppm) in DI water extract post rinse (3x) for different sample weights are shown for the Leopard Shark (A). Significant pairwise t-tests are denoted with asterisks (i.e., '*≤ 0.001', '≤ 0.01',* '≤ 0.05'). Linear regression of urea (ppm) versus C:N ratio for pre- and post-urea extracted outer laminae of six individuals is depicted for the Leopard Shark (B), with a marginal R2 value of 0.94. Estimated urea (ppm) GAM mean fit and 95% confidence interval surrounding fit for all pre-urea extracted eye lens laminae across the normalized diameter of the eye lens are shown for the Leopard Shark (C). The estimates were obtained via plot B linear mixed model intercept and C:N ratio coefficient. Grey shaded region representing the 95 % confidence interval around the pre- and post-apoptotic transition zone.

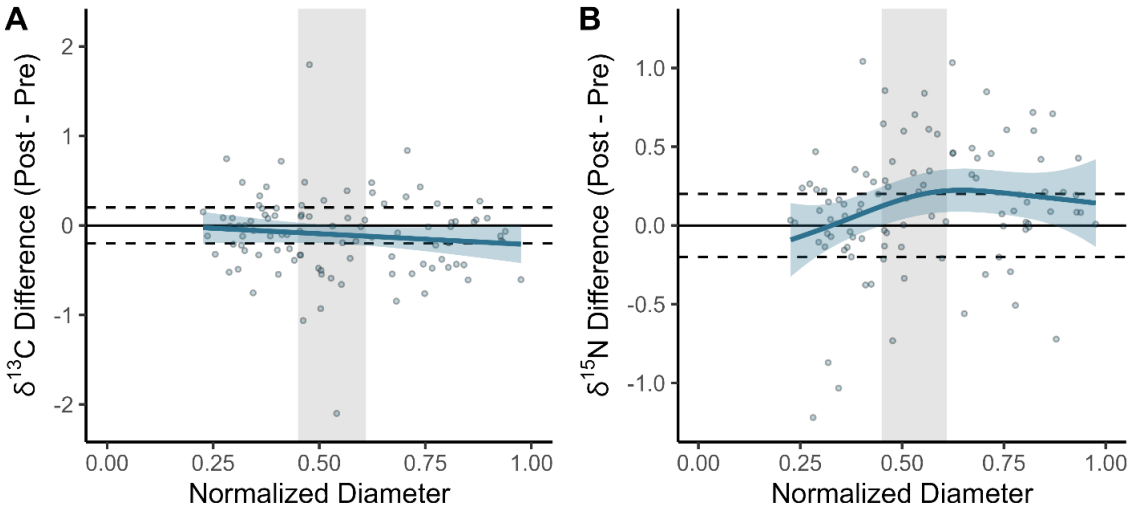

Figure 4.6: Leopard Shark GAM smooth curves of (A) $\delta^{13}C$ difference and (B) $\delta^{15}N$ difference (post-extracted minus pre-extracted in both systems) across the normalized diameter of eye lens. Black line indicates zero change, with dashed lines representing 95% confidence interval around average analytical error. Grey shaded region representing the 95 % confidence interval around the pre- and post-apoptotic transition zone.

4.9 Supplemental

4.9.1 Linear Mixed Model Results

We used linear mixed models (LMMs) in the "lme4" package (Bates et al., 2015) to explore data with linear relationships (i.e, urea peak-to-peak ratio versus C:N ratio). All models included C:N ratio as the response variable, as well as explanatory variables a different peak-to-peak ratios (fixed effect) for each model and fish ID (random effect). The explained variance (R^2) was computed using the "Mumin" package (Bartoń, 2023), based on the variables included in the comparison, which comprised "fixed" effects only and "fixed + random" effects. In this context, "fixed" R^2 refers to the marginal R^2, accounting solely for fixed effects, whereas "fixed + random" R^2 corresponds to the conditional R^2, encompassing both fixed and random effects. The Akaike Information Criterion (AIC), log likelihood (logLik), likelihood ratio test (LRT), and associated chi-squared values (ChiSq) were determined via the "lmerTest" package, where each random effect is removed in a dropwise fashion and LRT of model reductions are presented. We found that although incorporating the random effect proved significant in all peak ratio models meeting assumptions, model iterations with only fixed effects consistently yielded the lowest AIC values across each peak ratio model. For this reason, we only included results of linear regression models in the main text.

Table 4.4: C:N ratio versus peak-to-peak ratio linear mixed model (LMM) comparison.

Model (Peak Ratio)	Variables	R^2	AIC	logLik	LRT	ChiSq
C:N ~ Urea:Carboxylate	Fixed	0.85	-117.52	62.76		
C:N ~ Urea:Carboxylate	Fixed + Random	0.90	-115.57	60.79	3.94	0.05
C:N ~ Urea:Amide III	Fixed	0.85	-114.27	61.13		
C:N ~ Urea:Amide III	Fixed + Random	0.90	-111.26	58.63	5.01	0.03
C:N ~ Urea:Secondary Amide	Fixed	0.44	-73.91	40.95		

Model (Peak Ratio)	Variables	R^2	AIC	logLik	LRT	ChiSq
C:N ~ Urea:Secondary Amide	Fixed + Random	0.63	-71.75	38.87	4.16	0.04
C:N ~ Urea:Amide II*	Fixed	0.15	-60.02	34.01		
C:N ~ Urea:Amide II*	Fixed + Random	0.15	-62.02	34.01	0.00	1.00
C:N ~ Urea:Amide I*	Fixed	0.05	-57.08	32.54		
C:N ~ Urea:Amide I*	Fixed + Random	0.05	-59.08	32.54	0.00	1.00
C:N ~ Urea:Saturated (CH_2)*	Fixed	0.02	-53.59	30.79		
C:N ~ Urea:Saturated (CH_2)*	Fixed + Random	0.09	-55.38	30.69	0.20	0.65
C:N ~ Urea:Saturated (CH_3)*	Fixed	0.00	-53.15	30.58		
C:N ~ Urea:Saturated (CH_3)*	Fixed + Random	0.02	-55.13	30.57	0.02	0.89

Note: Asterisk (*) delineates models that did not meet assumptions.

5. Chapter 4: Validation of Eye Lens Laminae for Stable Isotope Analysis in Chondrichthyans — An Ecological Case Study on the Leopard Shark (*Triakis semifasciata*)

5.1 Introduction

Documenting life history events in highly mobile aquatic organisms is critical for informing policy and management decisions in conservation ecology but is often hindered by the difficulty of direct observation due to their vast movement ranges, the challenges of studying underwater environments, and technological constraints in long-term tracking. Across aquatic taxa, the stable isotope analysis (SIA) of various hard, accretionary tissues—such as otoliths in Actinopterygii (*i.e.*, ray-finned fishes; Reis-Santos et al., 2023), skeletal growth layers in Chelonioidea (*i.e.*, marine turtles; Turner Tomaszewicz et al., 2016), beak layers in Cephalopoda (*i.e.*, cephalopods; Xavier et al., 2022), as well as tooth series and vertebral bands in Chondrichthyes (*i.e.*, cartilaginous fishes; Kim, Tinker, et al., 2012; Zeichner et al., 2017)—have revealed key characteristics of diet, physiology, and movement through ontogeny. Calcified accretionary tissues, which vary in protein content, often require time-intensive sampling and demineralization to isolate collagen (Schlacher & Connolly, 2014), where the resulting carbon ($\delta^{13}C$) and nitrogen ($\delta^{15}N$) isotopic compositions provide critical insights into diet, trophic position, habitat use, and migratory patterns (Fry, 2006). An alternative approach gaining momentum in stable isotope ecology involves the use of chronological soft tissues, such as eye lens layers (*i.e.,* laminae; Fig. 5.1A, B – C), which accumulate inert protein throughout an organism's lifetime (Tzadik et al., 2017; Wallace et al., 2014). However, the accuracy of using eye lens laminae to interpret ecology has yet to be validated in Chondrichthyes.

Ecological interactions of consumers can be interpreted from $\delta^{13}C$ and $\delta^{15}N$ values (*i.e.*, $^{13}C/^{12}C$ and $^{15}N/^{14}N$, respectively), which originate from the consumer's diet and are incorporated into its tissues. Spatiotemporal shifts in biogeochemical processes (*e.g.*, carbon and nitrogen cycling) influence the isotopic composition of primary producers. The mode of carbon or nitrogen fixation in primary producers differentiates heavy versus light isotopes (*i.e.*, fractionation), creating baseline isotopic variation that propagates throughout an ecosystem's food web. As consumers assimilate carbon and nitrogen through their diet, metabolic processes such as respiration and waste excretion result in the preferential loss of lighter isotopes (*e.g.*, ^{12}C and ^{14}N) in the form of expelled CO_2 and urea/urine (DeNiro & Epstein, 1978; Post, 2002). This selective loss of lighter isotopes results in an isotopic offset between diet and consumer as energy transfers with trophic level, leading to the enrichment—or biomagnification—of heavier isotopes (*e.g.*, ^{13}C and ^{15}N) in consumer tissues (DeNiro & Epstein, 1978; Post, 2002). The magnitude of this fractionation is much greater in $^{15}N/^{14}N$ and thus, $\delta^{15}N$ values are more widely

used as an indicator of trophic position if the baseline can be accounted for (Post, 2002). Movement and trophic interactions are tracked in the $\delta^{13}C$ and $\delta^{15}N$ values of chronological tissues, capturing shifts in diet and trophic position across an individual's lifetime.

The accuracy of ecological inferences using $\delta^{13}C$ and $\delta^{15}N$ values rely on a comprehensive understanding of two fundamental processes: trophic discrimination factors (TDFs) and isotopic incorporation rates. There are tissue-specific TDFs that represent the estimated offset in stable isotope values between a consumer and its diet due to trophic fractionation, while isotopic incorporation refers to the rate at which isotopes from the diet are assimilated into consumer tissues. Different tissues integrate isotopic signals over varying timescales, with tissue specific incorporation rates representing the time required for tissue remodeling that incorporates recent dietary nutrients. Although time-consuming and resource-intensive, captive feeding studies are essential for determining tissue-specific TDFs and incorporation rates, providing a foundation for more accurate ecological interpretations. For instance, a captive feeding study on Leopard Sharks (*Triakis semifasciata*) revealed distinct TDFs and incorporation rates for muscle, red blood cells, and blood plasma, which reflect dietary inputs integrated over a specific time period (Kim, Casper, et al., 2012; Kim, Del Rio, et al., 2012). However, because these tissues only capture a single point in time, it is necessary to sample many individuals across different life stages to fully investigate ontogeny.

Chronological tissues like tooth series and vertebral bands are widely used to study life history ecology of elasmobranchs and both are validated using the Leopard Shark as a model organism (Carlisle et al., 2015; Estrada et al., 2006; Estupiñán-Montaño et al., 2019, 2021; Kim, Tinker, et al., 2012; Shipley et al., 2021). A series of teeth within the jaw provides fine-scale resolution of $\delta^{13}C$ and $\delta^{15}N$ values (*e.g.*, ~50 days; Zeichner et al., 2017), enabling the interpretation of seasonal movement and trophic patterns. In contrast, vertebral bands track isotopic values over an individual's entire lifetime (Fig. 5.1A, D – E; Carlisle et al., 2015; Estupiñán-Montaño et al., 2019; Kim, Tinker, et al., 2012). However, vertebrae presents challenges for precise sampling, particularly in smaller species, and collagen isolation is time-intensive (Kim, Tinker, et al., 2012; Kim & Koch, 2012). These limitations have prompted the exploration of alternative tissues in elasmobranchs, with eye lens laminae holding great promise, as they are widely used in fishes where it is assumed they represent lifetime records with minimal preparation and no need for specialized equipment (Bell-Tilcock et al., 2020; Kuntz et al., 2024; Quaeck-Davies et al., 2018; Vecchio & Peebles, 2022; Wallace et al., 2014).

In this study, we compare $\delta^{13}C$ and $\delta^{15}N$ values from eye lens laminae and vertebral bands of wild Leopard Sharks to validate the eye lens for stable isotope ecology. We address three key questions: 1) Do eye lens laminae reflect similar isotopic patterns to vertebral bands? 2) What are the TDFs of Leopard Shark eye lens laminae? 3) How can eye lens laminae be applied to an ecological case study to assess the movement and isotopic niche of Leopard Sharks through ontogeny? By evaluating the accuracy and reliability of these tissues, we aim to establish eye lens laminae as a substrate for investigating elasmobranch ontogeny and life history ecology.

5.2 Materials and Methods

5.2.1 Sampling

To validate the use of eye lens laminae in elasmobranchs, we compared the SIA of muscle, eye lenses, and vertebrae in Leopard Sharks. Then, we used eye lenses to study their ecology through life history in central California. Here, we collected sub-adult and adult Leopard Sharks across four sites (San Francisco Estuary [SFE; n = 9], Drake's Estero State Marine Conservation Area [hereby after referred to Drake's Estero; n = 10], Tomales Bay [n = 10], and Bodega Bay [n = 9]) via hook and line, set gill nets, and salvage donation from fishers (Fig. 5.2). Individuals were caught and euthanized with methods approved by the Institutional Animal Care and Use Committee of the University of California, Merced (protocol # AUP20-0013), California Department of Fish & Wildlife (permit S-201820001-20182-001 and S-201840003-20196-001), and the National Park Service (#PORE-2020-SCI-0017). Leopard Sharks were then transported on ice to the University of California, Merced for dissection and further analyses. In addition, post necropsy we coincidentally and opportunistically collected Leopard Shark fetuses (n = 15) of a single near-term pregnant individual collected from Tomales Bay, specifically used for aging methodology (Supplemental 5.7.1).

We dissected and serially sampled eye lens laminae and vertebral bands chronologically to reconstruct the past isotopic life history of each sub-adult/adult Leopard Shark (n = 38), while also subsampling muscle tissue. Muscle tissue was lipid and urea extracted following Kim & Koch (2012) prior to lyophilization and preparation for SIA. For eye lenses, laminae were measured for diameter (mm) following procedures outlined in Kuntz et al. (2024), while laminar midpoints were calculated following Vecchio and Peebles (2022). In addition, the total eye lens diameter (capsule diameter) was measured for each individual (n = 53) to compare with total length and facilitate back-calculation of age (Supplemental 5.7.1). Eye lens laminae were desiccated in a drying oven at 55 °C for 12 hours before weighing and preparation for SIA. If urea effects were identified post SIA (C:N ratio ≤ 2.47; Kuntz et al., 2024), that sample was removed from further analyses (laminae removed, n = 5).

To establish eye lenses as life history recorders, vertebrae from Leopard Sharks were also analyzed. The 15th thoracic vertebra was dissected from six individuals across three sites (SFE [n = 3], Drake's Estero [n = 1], and Tomales Bay [n = 2]). Each vertebral centrum was mounted in epoxy resin, and two parallel sagittal sections were taken via diamond saw. The first 1-mm section was polished to identify annual bands for age determination under dissecting microscope, while the second 2-mm section was sampled for SIA. The small size of Leopard Shark vertebrae required combining multiple annual bands in some sections to achieve the minimum sample size for SIA. Early, wider annual bands could be segmented and analyzed individually, whereas later, smaller bands were segmented and later combined. Similarly to eye lens laminar measurements described in Kuntz et al. (2024), images were taken on a dissecting microscope of the vertebral section after removal of each segmented sample, and a vertebral band midpoint was measured (mm) to compare with eye lens laminae. Aging of vertebral bands is described in Supporting Information 5.7.1. Each vertebral section was demineralized using

ethylenediaminetetraacetic acid (EDTA) following Kim & Koch (2012). Demineralized vertebral section samples were frozen 8+ hours and then lyophilized overnight prior to weighing and preparation for SIA.

5.2.2 Stable Isotope Analysis

We analyzed eye lens laminae and vertebral banding sections for $\delta^{13}C$ and $\delta^{15}N$ values with an Elemental Analyzer coupled to a continuous-flow Isotope Ratio Mass Spectrometer (EA-cf-IRMS) via Conflo IV at the Stable Isotope Ecosystem Laboratory of (SIELO) the University of California, Merced. Findings are presented in standard delta notation (δ, ‰), with $\delta^{13}C$ values relative to Vienna Pee Dee Belemnites (VPDB) and $\delta^{15}N$ values relative to V-AIR. Data were corrected for linearity and drift with calibrated reference materials (USGS 40 [$\delta^{13}C = -26.4 \pm 0.1$ ‰ and $\delta^{15}N = -4.5 \pm 0.1$ ‰, n = 40]; USGS 41a [$\delta^{13}C = 36.6 \pm 0.1$ ‰ and $\delta^{15}N = 47.6 \pm 0.1$ ‰, n = 22]) and checked with an internal reference material (Mb Squid [$\delta^{13}C = -18.8 \pm 0.1$ ‰ and $\delta^{15}N = 11.8 \pm 0.1$ ‰, n = 14]).

5.2.3 Eye Lens Trophic Discrimination Factor Determination

To determine eye lens laminae TDFs, we compared methods across tissues to validate our results. First, we compared vertebral band and eye lens lamina $\delta^{13}C$ and $\delta^{15}N$ values. Although vertebral bands and eye lens laminae represent the same timeframes, their sampling is uneven. To address this, we performed two separate comparisons between serially sampled vertebral bands and eye lens laminae. In the first method, we matched each eye lens lamina to its nearest neighbor (NN) among the vertebral bands based on $\delta^{13}C$ and $\delta^{15}N$ values. In the second method, we interpolated both vertebral bands and eye lens laminae to generate evenly spaced sampling across 100 time points and applied dynamic time warping (DTW) to align points optimally over time (see Supplemental 5.7.2). To check the validity of these results, we compared $\delta^{13}C$ and $\delta^{15}N$ values between muscle tissue and the most recent eye lens lamina for each individual. After calculating the mean and standard deviation differences between tissues in each of these scenarios, we compared these values to known Leopard Shark TDFs for cartilaginous vertebral collagen ($\delta^{13}C = 4.2 \pm 0.7$ ‰; $\delta^{15}N = 2.5 \pm 1.1$ ‰; Kim, Tinker, et al., 2012) and muscle tissue ($\delta^{13}C = 1.7 \pm 0.5$ ‰; $\delta^{15}N = 3.7 \pm 0.4$ ‰; Kim, Casper, et al., 2012). We then calculated eye lens laminae TDFs and propagated the associated error by comparing the observed tissue offset with the previously published TDF values.

5.2.4 Statistical Analyses

We conducted statistical analyses using R version 4.3.1 (R Core Team, 2023). Dynamic time warping (DTW) was applied using the "dtw" package (Giorgino, 2009), as described above. Non-linear relationships, including stable isotope values over time, were analyzed with the "mgcv" package (Wood, 2017) using generalized additive models (GAMs). In these models, the difference in stable isotope values ($\delta^{13}C$ or $\delta^{15}N$) between eye lens laminae and vertebral bands was the response variable, with age as the explanatory variable (smooth term) and Fish ID as a random smooth effect. To examine isotopic life history variation across regions, we implemented a hierarchical GAM (HGAM) following Pedersen et al. (2019), with stable isotope values as the response

variable and age as a global smoother. Group-level smoothers of age by region and region-specific intercepts were included as random smooth effects, alongside Fish ID to account for individual variation. Model assumptions were validated using the "DHARMa" package (Hartig, 2022).

We also used a Bayesian bivariate generalized linear mixed model (GLMM) via the "MCMCglmm" package (Hadfield, 2010) to analyze total niche width (TNW) and regional isotopic niche space (δ13C and δ15N), following Ingram et al. (2018). Separate models were fitted for each region, incorporating random effects to estimate between-individual variation (BIC) and residual covariance to represent within-individual variation (WIC). Each model was run for 50,000 iterations with a thinning interval of 50. Subpopulation 95% confidence interval ellipses were generated from the posterior covariance matrices.

5.3 Results

5.3.2 Laminae to Vertebral Banding SIA Comparison

We observed similar trends in $\delta^{13}C$ and $\delta^{15}N$ values between eye laminae and vertebral bands across all individuals and ages (Fig. 5.3A-C ; Supplemental 5.7.1, Fig. 5.7). Because $\delta^{13}C$ and $\delta^{15}N$ patterns, as well as GAM results, were similar for NN and DTW approaches, we report only NN results below (age ≥ 0). The DTW results and analyses are provided in Supplemental 5.7.2. For the $\delta^{13}C$ GAM, age (smooth term) and fish ID explained little variance ($R^2 = 0.04$) and were not significant ($p = 0.91$ and $p = 0.17$, respectively), indicating no trend and a consistent offset in $\delta^{13}C$ between eye lens laminae and vertebral bands across age (Fig. 5.4A). In contrast, for the $\delta^{15}N$ GAM, age (smooth term) and fish ID explained slightly more variance ($R^2 = 0.23$) and were significant ($p = 0.02$ and $p = 0.05$, respectively), suggesting a slight increase in the $\delta^{15}N$ offset between eye lens laminae and vertebral bands with age (Fig. 5.3B).

The offset between eye lens laminae and vertebral bands for $\delta^{13}C$ values over the age of zero was substantial (Fig. 5.3; Supplemental 5.7.2, Fig. 5.8 and 5.10), indicating that eye lens crystallin consistently has lower $\delta^{13}C$ values than cartilaginous vertebrae collagen. Using the NN approach we found a mean difference between eye lens laminae and vertebral bands to be -1.7 ± 1.2 ‰ (Fig. 5.3A). With the previously validated $\delta^{13}C$ TDF for Leopard Shark cartilaginous vertebrae collagen being 4.2 ± 0.7 ‰ (Kim, Tinker, et al., 2012), these results indicate that the eye lens crystallin TDF for $\delta^{13}C$ is estimated to be 2.5 ± 1.4 ‰ (Fig. 5.3D). The same NN approach for $\delta^{15}N$ values estimated a less pronounced offset between eye lens laminae and vertebral bands over the age of zero (Fig. 5.3B), where we observed a mean offset of 0.2 ± 1.1 ‰. With the $\delta^{15}N$ TDF of Leopard Shark vertebrae having been found to be 2.5 ± 1.1 ‰ (Kim, Tinker, et al., 2012), we then estimate the eye lens TDF for $\delta^{15}N$ to be 2.7 ± 1.6 ‰ (Fig. 5.3D).

We also used an alternative approach to validate our estimation of eye lens TDFs by comparing eye lens laminae to muscle tissue in Leopard Sharks, as the TDF for muscle tissue has been more thoroughly investigated (Kim, Casper, et al., 2012). When compared to eye lens crystallin, the difference in means was found to be 1.0 ± 0.6 ‰, with eye lens crystallin being higher than muscle tissue. With the previously validated

$\delta^{13}C$ TDF for Leopard Shark muscle tissue being found to be 1.7 ± 0.5 ‰ (Kim, Casper, et al., 2012). We estimated the eye lens crystallin TDF for $\delta^{13}C$ to be 2.7 ± 0.8 ‰ (Fig. 5.3D). The $\delta^{15}N$ TDF for Leopard Shark muscle tissue is 3.7 ± 0.4 ‰ (Kim, Casper, et al., 2012). When compared to eye lens crystallin, the difference in means was found to be -1.1 ± 0.7 ‰, with eye lens crystallin being lower than muscle tissue (Fig. 5.3B). As a result, the eye lens crystallin TDF for $\delta^{15}N$ is estimated to be 2.6 ± 0.8 ‰ (Fig. 5.3D).

5.3.3 Case Study: Leopard Shark Ecology

5.3.3.1 Life History

The lifetime record of Leopard Sharks from eye lens stable isotope composition indicates subpopulation structure in Central California across the four localities here. A substantial portion of the $\delta^{13}C$ variance in eye lens laminae was explained by the carbon HGAM ($R^2 = 0.70$), indicating notable differences across regions (Fig. 5.4A,B). Significant explanatory variables included age (smooth term; $p < 0.001$), age-by-region interaction (smooth terms; $p < 0.001$ for Bodega Bay, Drake's Estero, and SFE; $p = 0.002$ for Tomales Bay), region (random smooth effect; $p < 0.001$), and fish ID (random smooth effect; $p = 0.001$). Predicted smooths from the $\delta^{13}C$ HGAM revealed that Leopard Sharks followed similar trends before birth with consistently decreasing values throughout embryonic development (Fig. 5.4A,B). Post-birth, $\delta^{13}C$ trends diverged between localities (Fig. 5.4A,B) and adult sharks from the SFE showed minimal changes in $\delta^{13}C$ values over their lifetime (Fig. 5.4A,B). In contrast, adults from Tomales Bay, Drake's Estero, and Bodega Bay started with similar $\delta^{13}C$ values as those from the SFE but shifted to progressively higher $\delta^{13}C$ values by ~ 3 years old (Fig. 5.4A,B).

Similarly, the $\delta^{15}N$ HGAM explained a large proportion of variance within eye lens laminae ($R^2 = 0.72$). Significant explanatory variables included age (smooth term; $p < 0.001$), age-by-region interaction (smooth term; $p = 0.004$ for Bodega Bay, $p = 0.010$ for Tomales Bay, $p = 0.035$ for Drake's Estero, and $p < 0.001$ for the SFE), region (random smooth effect; $p < 0.001$), and fish ID (random smooth effect; $p < 0.001$). Predicted smooth trends of $\delta^{15}N$ across all localities showed similar patterns, with values increasing throughout embryonic development until birth, followed by a decline to a steady state with the environment (Fig. 5.4C,D). However, while individuals from the SFE followed a similar pattern as other localities, this subpopulation stood out for having elevated $\delta^{15}N$ values (Fig. 5.4C,D). For both isotope systems, individual variation observed during embryonic development continued post-birth (Fig. 5.4B,D). These findings highlight distinct patterns in Leopard Shark life history ecology amongst and between localities.

5.3.3.2 Isotopic Niche

We used Bayesian bivariate mixed-effects models to assess variation in Leopard Shark eye lens $\delta^{13}C$ and $\delta^{15}N$ values across four regions, revealing substantial overlap between regional ellipses (Fig. 5.5A). In all four regional models, both $\delta^{13}C$ and $\delta^{15}N$ exhibited significant fixed effects (pMCMC < 0.001 for both isotope systems). Among the regions, $\delta^{13}C$ values ranged from -12.3 ± 0.8 ‰ in Bodega Bay to -16.0 ± 0.8 ‰ in San Francisco Bay, and $\delta^{15}N$ values from 16.0 ± 0.8 ‰ in Bodega Bay to 18.1 ± 1.2 ‰ in

San Francisco Bay. Variance in $\delta^{13}C$ and $\delta^{15}N$ was partitioned at both the individual (G-structure) and residual (R-structure) levels, with individual-level variance generally higher for $\delta^{15}N$ than $\delta^{13}C$ across all regions. Covariation between $\delta^{13}C$ and $\delta^{15}N$ remained consistently negative at the residual level. Additionally, total niche width (TNW) varied among regions, with Drake's Estero exhibiting the broadest TNW (11.1), followed by Bodega Bay (8.2), Tomales Bay (8.1), and San Francisco Bay (6.2). Individuals within each region exhibited a high degree of overlap in their isotopic niches, reflecting similar post-birth movement and foraging behaviors of Leopard Sharks within each subpopulation (Fig. 5.5B).

5.4 Discussion

This study establishes the use of eye lens laminae as a chronological tissue for SIA in elasmobranchs, providing an unprecedented opportunity to reconstruct individual isotopic life histories. By first comparing the biochemical composition of eye lens laminae and vertebral bands, we establish the foundation for interpreting isotopic offsets between these tissues. These offsets allowed us to determine the eye lens TDF for carbon and nitrogen stable isotopes, which will enable accurate ecological interpretation if prey data are available. Considering these factors, we found that isotopic patterns align extremely well between eye lens laminae and vertebral bands, validating the lens as a novel isotopic archive. Finally, we applied this framework to an ecological case study, demonstrating how eye lens laminae can track Leopard Shark movement and isotopic niche variation across ontogeny. This integrative approach enhances our ability to decipher elasmobranch life histories, opening new avenues for ecological and conservation research.

5.4.1 Comparison of Biochemical Composition

Biochemical differences between tissues influence stable isotope values due to variation in protein composition and fractionation processes. The eye lens, primarily composed of crystallin proteins, has the highest protein fraction among body tissues (~70% of its composition; Jaenicke, 1999), contrasting sharply with elasmobranch cartilaginous vertebrae (17.4%–26.8%; Porter et al., 2006). Elasmobranch cartilage consists mainly of a hyaline-like matrix with proteoglycan proteins and collagen fibers (e.g., types I, II, and X; Porter et al., 2006; Seidel et al., 2017; Shoulders & Raines, 2009), forming a flexible yet durable framework. This structure partially mineralizes during ontogeny to enhance rigidity and support (Seidel et al., 2017). However, the mineral components (~39.0%–55.1%) of elasmobranch cartilage must be removed to assess the organic component's stable isotope values accurately (Kim & Koch, 2012). In contrast to vertebrae, the eye lens is primarily composed of crystallin proteins (α- and βγ-families; Bloemendal, 1981; Bloemendal et al., 2004) that are integral to eye lens fiber cells and develop in concentric layers from the epithelial outer edge. Over time, these fibers transition from hydrated, pre-apoptotic laminae to rigid, post-apoptotic layers composed of tightly packed crystallins (Andley, 2008; Berman, 1991; Kuntz et al., 2024). This structure is crucial for maintaining lens transparency and refractive properties throughout an individual's life but also record stable isotope values across inert laminae

(Bell-Tilcock et al., 2020; Kuntz et al., 2024; Vecchio & Peebles, 2022; Wallace et al., 2014).

5.4.2 Isotopic Offsets

Fractionation of carbon isotopes occurs with transformations during amino acid metabolism and biosynthesis, where the selective loss of ^{12}C along the metabolic routing pathway elevates $\delta^{13}C$ values only in amino acids whose carbon chains are altered during synthesis, resulting in newly biosynthesized non-essential amino acids that retain more ^{13}C than their precursors (Vane et al., 2025). Consequently, the relative proportion of certain amino acids across protein types can drive isotopic offsets between tissues and impact TDFs. Consistent with this, we observed lower carbon TDFs in eye lens laminae compared to cartilaginous vertebrae. Elasmobranch cartilage is primarily made of type I and type II collagen that are rich in glycine—a non-essential amino acid with relatively high $\delta^{13}C$ values—and constitute ~35% of amino acids in both collagen types (Supplemental 5.7.3, Table 5.1; Mizuta et al., 2003). In contrast, the α- and γ-crystallin proteins of eye lens laminae exhibit a lower proportion of glycine (Supplemental 5.7.3, Table 1). This compositional difference between cartilaginous vertebrae and eye lens laminae remains consistent post-birth (Fig. 5.4A; Supplemental 5.7.2, Fig. 5.8 and 5.10) and therefore carbon TDFs for the eye lens are consistent throughout the Leopard Shark's lifetime.

During amino acid metabolism, deamination and transamination reactions modify and fractionate nitrogen isotopes (Chikaraishi et al., 2009). Deamination removes ^{15}N-depleted amino groups, which are excreted as urea in most organisms but retained in chondrichthyans for osmoregulation (Hazon et al., 2003). This retained urea has been shown to lower the $\delta^{15}N$ values of proteinaceous tissues, including the outer pre-apoptotic eye lens laminae, and must be removed when present in high enough concentrations to ensure accurate $\delta^{15}N$ measurements (Kim & Koch, 2012; Kuntz et al., 2024). Thus, after contaminant removal, bulk $\delta^{15}N$ values are influenced by the balance between amino acids that undergo deamination and transamination reactions and those that do not, potentially contributing to variations in TDFs across tissues. We observed minimal differences in $\delta^{15}N$ offsets between eye lens laminae and cartilaginous vertebrae, likely due to the similar amino acids in the protein structure of both tissues (Supplemental 5.7.3). However, $\delta^{15}N$ offsets increased slightly with age following the distinction of pre- vs. post-apoptotic laminae (Fig. 5.3B), suggesting effects of shifting protein composition (Supplemental 5.7.3). Cartilaginous vertebrae maintain consistent amino acid composition once mineralized, whereas the eye lens shows regional variation in protein fractions and amino acid composition. γ-Crystallin, expressed early in development, is concentrated in the inner, post-apoptotic laminae (Keenan et al., 2009; Vendra et al., 2016) and has a composition similar to collagens (Supplemental 5.7.3). In contrast, α-crystallin, a chaperone protein in the outer, pre-apoptotic laminae (Grey & Schey, 2008), has a substantially different amino acid profile (Supplemental 5.7.3). This compositional gradient results in the inner, post-apoptotic eye lens laminae exhibiting $\delta^{15}N$ values comparable to cartilaginous vertebrae, while the outer, pre-apoptotic laminae show higher $\delta^{15}N$ values due to the greater influence of highly fractionated amino acids.

5.4.3 Alignment of Isotopic Patterns

The similarities in $\delta^{13}C$ and $\delta^{15}N$ temporal profiles between eye lens laminae and cartilaginous vertebrae suggest that both tissues have comparable isotopic incorporation rates. Because these accretionary tissues form through sequential protein deposition without remodeling, they integrate dietary inputs over similar timescales. The agreement between NN and DTW approaches validates these observed similarities, while DTW uniquely visualizes how time lags would need to be adjusted to align isotopic profiles via warping paths. However, we found no consistent lag patterns between tissues—some warping paths showed eye lens laminae lagging vertebrae, while others showed the reverse (Supplemental 5.7.2, Fig. 5.9). One explanation is likely due to the oversimplification of VBGF, which does not account for changes in growth rate (Cailliet et al., 2006) that may shift with temperature or diet variation through time. In addition, the compositional changes between pre- and post-apoptotic layers affect precise dissection of eye lens laminae (Kuntz et al., 2024; Quaeck-Davies et al., 2018). There is also difficulty obtaining sufficient material from vertebral bands in smaller species and multiple annual bands must be pooled, which prevents finer temporal resolution. While these sources of error introduce uncertainty in temporal alignment, our sample age estimation across eye lens laminae generates lifetime records of stable isotope composition. This method may be particularly useful for chondrichthyans that exhibit ontogenetic shifts in habitat use or foraging ecology, offering unique insights into how resource use can vary across an individual's lifetime.

5.4.3 Case Study: Leopard Shark Ecology

5.4.3.1 Nursey Habitat

Despite being the model organism for elasmobranch stable isotope ecology, much of the Leopard Shark's ecological life history remains unresolved. Eye lens laminae provide a unique opportunity to investigate movement and foraging ecology across an individual's lifetime. Leopard Sharks from all localities exhibited similar declining $\delta^{13}C$ trends during embryonic stages (Fig. 5.4A,B), likely due to metabolic fractionation (Supplemental 5.7.4). The striking similarity in $\delta^{13}C$ values up until birth suggests that maternal diets were sourced from isotopically similar baselines. However, post-birth patterns diverge—individuals from the SFE maintain relatively consistent $\delta^{13}C$ values throughout their lifetime, while those from other localities shift to distinct isotopic baselines (Fig. 5.4A). Given that no other habitat in this study exhibits the same range of baseline $\delta^{13}C$ values as the SFE due to the SFE having the largest freshwater outflow of any California watershed (Emmett et al., 2000), two explanations emerge: either maternal foraging occurs in the SFE before migration and birth elsewhere, or the SFE serves as a shared nursery where individuals are born before dispersing to other regions. The presence of Leopard Shark neonates consistently in the SFE further supports its role as a critical habitat for early life stages, potentially linking subpopulations through a common natal origin.

Three main criteria for determining a shark nursery area are as follows: 1) juveniles must be more frequently encountered in the habitat compared to other areas; 2) juveniles should remain in the habitat for extended periods, indicating its importance for

their development; 3) the habitat must be repeatedly utilized across years (Heupel et al., 2007, 2018). The SFE and Tomales Bay are recognized as nursery areas for Leopard Sharks (Hughes et al., 2014) based on the presence of juveniles (Criterion 1). The SFE has been identified as both a primary (neonate/young-of-year) and secondary (juvenile) nursery habitat for the Leopard Shark, supported by the consistent presence of young sharks (Criterion 1) and long-term data spanning over 30 years (Criterion 3; Russo, 2019). Additionally, while Smith & Abramson's (1990) mark-recapture study showed individuals remained in the estuary for months or years post-tagging (Criterion 2), their habitat use between tagging and recapture remains uncertain. Baseline $\delta^{13}C$ values follow a predictable gradient from riverine to marine environments (Simenstad & Wissmar, 1985) and therefore the observed consistently low $\delta^{13}C$ eye lens patterns from Leopard Sharks (Fig. 5.4A,B) confirms residency and use of SFE.

5.4.3.2 Leopard Shark Movement and Foraging Ecology

Investigating isotopic trends throughout the Leopard Shark's lifetime can provide insights into how regional habitat variability shapes their movement and trophic ecology, as their behavior and resource use may vary significantly across different environmental conditions. We found that Leopard Sharks exhibit regional isotopic separation after birth (Fig. 5.4), reflecting distinct isotopic baselines shaped by regional variations in biogeochemical processes and productivity regimes. The Leopard Sharks caught in SFE exhibit the smallest TNW of all regions, suggesting consistent foraging and little movement compared to other subpopulations; Leopard Sharks caught in Bodega Bay, Tomales Bay, and Drake's Estero have similar TNWs and overlapping ellipses (Fig 5.5). Additionally, SFE Leopard Sharks exhibited lower $\delta^{13}C$ and higher $\delta^{15}N$ values throughout their lifetime when compared to other localities (Fig. 5.4 and 5.5), agreeing with previous claims of a resident Leopard Shark population (Smith, 2001).

Previous studies on Leopard Shark life history in central California documented both tidally influenced daily movements and seasonal migrations associated with estuarine habitats (Carlisle & Starr, 2009, 2010). These oscillating movement patterns across the estuarine boundary are likely shaped by a habitat's morphology, size, and tidal dynamics, which may be similar across small alluvial estuaries such as Elkhorn Slough (Carlisle and Starr 2009, 2010), Bodega Bay, and Drake's Estero. In these areas, individuals forage at the estuarine boundary, where coastal upwelling contributes to higher $\delta^{13}C$ values (Vokhshoori et al., 2014; Buck et al., 2014; Kimbro et al., 2009). In contrast, larger estuaries with deep channels, such as the SFE and Tomales Bay, provide tidal refugia for longer residency and sustained subsistence on the available resources. In these localities, terrestrial nutrients also contribute to baseline $\delta^{13}C$ values. The SFE receives freshwater outflow from the Sacramento-San Joaquin Delta, which delivers terrestrial C_3 carbon with lower $\delta^{13}C$ values (Cloern et al., 2002; Simenstad & Wissmar, 1985). While more muted, Tomales Bay also experiences seasonal freshwater outflow. Therefore, the differentiation in $\delta^{13}C$ values reflects the large terrestrial carbon source in the SFE, coastal upwelling carbon sources in Bodega Bay and Drake's Estero, and the mixing of terrestrial and marine carbon in Tomales Bay.

Leopard Shark eye lens $\delta^{15}N$ patterns were relatively consistent across regions, but individuals from the SFE exhibited higher $\delta^{15}N$ values compared to the other three regions (Fig. 5.4C,D). While higher $\delta^{15}N$ is commonly indicative of a trophic shift, Leopard Sharks are generalist, meso-predators with little evidence of ontogenetic diet shifts. An alternative explanation—similar to $\delta^{13}C$ patterns—is that baseline variation in $\delta^{15}N$ values is being propagated through the food web. In Bodega Bay, Drake's Estero, and Tomales Bay, upwelling-derived nitrogen dominates (Sigman et al., 2009). In contrast, anthropogenic NH_4^+ and NO_3^- inputs from wastewater treatment cause eutrophication in the SFE (Cloern et al., 2020), which results in elevated baseline $\delta^{15}N$ values (McClelland et al., 1997). Lastly, while the elevated $\delta^{15}N$ values exhibited by Leopard Sharks in later life may reflect an ontogenetic shift toward feeding at higher trophic levels as gape size increases, this trend is instead likely driven by changes in amino acid composition between pre- and post-apoptotic laminae.

The regional differences in Leopard Shark isotopic life histories suggest some individuals exhibit natal site fidelity, while others disperse from the SFE before foraging in isotopically distinct habitats. Although several localities in Central California have been proposed as Leopard Shark nursery habitats (Barker et al., 2015; Cooper, 2022; Hughes et al., 2014), we hypothesize that the SFE serves as the primary natal nursery for this genetic population due to: 1) the extensive habitat available to Leopard Sharks in the SFE, which is the largest estuary across their range, and 2) the likelihood that the majority of individuals in this study originated from the SFE. Additionally, with the regions sampled in this study falling within the Northern California genetic population (Barker et al., 2015), we hypothesize that Leopard Sharks in Central California function as a metapopulation, with dispersal of individuals across ontogeny facilitating genetic exchange.

5.4.3.3 Conservation Implications

Population structure plays a crucial role in shaping ecological responses to environmental change, and understanding movement, residency, and ontogenetic shifts is key to predicting these responses and guiding regional conservation efforts. Given that the SFE is considered a crucial transition zone for gene flow within the Leopard Shark's northern genetic population (Barker et al., 2015), our findings—highlighting both a resident population and a potential shared nursery habitat before dispersal and subsequent residency in other regions—reinforce its role as an essential subpopulation. With native fish populations in the SFE continuing to decline (Feyrer et al., 2007; Sommer et al., 2007), a deeper understanding of Leopard Shark population dynamics is urgently needed, particularly as take regulations in the state of California have remained unchanged for over three decades. Our results highlight the pressing need to reevaluate management strategies and update protections to reflect the species' complex life history and critical habitat use within the SFE.

5.5 References

Andley, U. P. (2008). The Lens Epithelium: Focus on the expression and function of the alpha-crystallin chaperones. Int J Biochem Cell Biol, 40(3), 317–323. https://www.ncbi.nlm.nih.gov/pmc/articles/PMC3624763/pdf/nihms412728.pdf

Barker, A. M., Nosal, A. P., Lewallen, E. A., & Burton, R. S. (2015). Genetic structure of leopard shark (Triakis semifasciata) populations along the Pacific coast of North America. Journal of Experimental Marine Biology and Ecology, 472, 151–157. https://doi.org/10.1016/j.jembe.2015.06.020

Bell-Tilcock, M., Jeffres, C. A., Rypel, A. L., Sommer, T. R., Katz, J. V. E., Whitman, G., & Johnson, R. C. (2020). Advancing diet reconstruction in fish eye lenses. Methods in Ecology and Evolution, February 2021. https://doi.org/10.1111/2041-210X.13543

Berman, E. R. (1991). Biochemistry of the Eye. Plenum Press, 476.

Bloemendal, H. (1981). Molecular and cellular biology of the eye lens. John Wiley & Sons. https://lccn.loc.gov/80026815

Bloemendal, H., De Jong, W., Jaenicke, R., Lubsen, N. H., Slingsby, C., & Tardieu, A. (2004). Ageing and vision: Structure, stability and function of lens crystallins. Progress in Biophysics and Molecular Biology, 86(3), 407–485. https://doi.org/10.1016/j.pbiomolbio.2003.11.012

Buck, C. M., Wilkerson, F. P., Parker, A. E., & Dugdale, R. C. (2014). The Influence of Coastal Nutrients on Phytoplankton Productivity in a Shallow Low Inflow Estuary, Drakes Estero, California (USA). Estuaries and Coasts, 37(4), 847–863. https://doi.org/10.1007/s12237-013-9737-6

Cailliet, G. M., Smith, W. D., Mollet, H. F., & Goldman, K. J. (2006). Age and growth studies of chondrichthyan fishes: The need for consistency in terminology, verification, validation, and growth function fitting. Environmental Biology of Fishes, 77(3–4), 211–228. https://doi.org/10.1007/s10641-006-9105-5

Carlisle, A. B., Goldman, K. J., Litvin, S. Y., Madigan, D. J., Bigman, J. S., Swithenbank, A. M., Kline, T. C., & Block, B. A. (2015). Stable isotope analysis of vertebrae reveals ontogenetic changes in habitat in an endothermic pelagic shark. Proceedings of the Royal Society B: Biological Sciences, 282(1799). https://doi.org/10.1098/rspb.2014.1446

Carlisle, A. B., & Starr, R. M. (2009). Habitat use, residency, and seasonal distribution of female leopard sharks Triakis semifasciata in Elkhorn Slough, California. Marine Ecology Progress Series, 380(2001), 213–228. https://doi.org/10.3354/meps07907

Carlisle, A. B., & Starr, R. M. (2010). Tidal movements of female leopard sharks (Triakis semifasciata) in Elkhorn Slough, California. Environmental Biology of Fishes, 89(1), 31–45. https://doi.org/10.1007/s10641-010-9667-0

Chikaraishi, Y., Ogawa, N. O., Kashiyama, Y., Takano, Y., Suga, H., Tomitani, A., Miyashita, H., Kitazato, H., & Ohkouchi, N. (2009). Determination of aquatic food-web structure based on compound-specific nitrogen isotopic composition of amino acids. Limnology and Oceanography: Methods, 7(NOV), 740–750. https://doi.org/10.4319/lom.2009.7.740

Cloern, J. E., Canuel, E. A., & Harris, D. (2002). Stable carbon and nitrogen isotope composition of aquatic and terrestrial plants of the San Francisco Bay estuarine system.

Limnology and Oceanography, 47(3), 713–729. https://doi.org/10.4319/lo.2002.47.3.0713

Cloern, J. E., Schraga, T. S., Nejad, E., & Martin, C. (2020). Nutrient status of San Francisco Bay and its management implications. Estuaries and Coasts, 43(6), 1299–1317. https://doi.org/10.1007/s12237-020-00737-w

Cooper, A. A. B. (2022). Demography , Diet , and Habitat Use of Leopard Sharks (Triakis semifasciata) in a Protected Estuarine Environment By. Sanoma State University.

DeNiro, M. J., & Epstein, S. (1978). Influence of diet on the distribution of carbon isotopes in animals. Geochemica et Cosmochimica Acta, 42, 495–506. https://doi.org/10.1002/mop.25285

Emmett, R., Llansó, R., Newton, J., Thom, R., Hornberger, M., Morgan, C., Levings, C., Copping, A., & Fishman, P. (2000). Geographic signatures of north american west coast estuaries. Estuaries and Coasts, 23(6), 765–792. https://doi.org/10.2307/1352998

Estrada, J. A., Rice, A. N., Natanson, L. J., & Skomal, G. B. (2006). Use of isotopic analysis of vertebrae in reconstructing ontogenetic feeding ecology in white sharks. Ecology, 87(4), 829–834. https://doi.org/10.1890/0012-9658(2006)87[829:UOIAOV]2.0.CO;2

Estupiñán-Montaño, C., Galván-Magaña, F., Sánchez-González, A., Elorriaga-Verplancken, F. R., Delgado-Huertas, A., & Páez-Rosas, D. (2019). Dietary ontogeny of the blue shark, Prionace glauca, based on the analysis of δ13C and δ15N in vertebrae. Marine Biology, 166(101), 1–13. https://doi.org/10.1007/s00227-019-3550-0

Estupiñán-Montaño, C., Tamburin, E., & Delgado-Huertas, A. (2021). Stable isotope evidence for movements of hammerhead sharks Sphyrna lewini, connecting two natural protected areas in the Colombian Pacific. Marine Biodiversity, 51(5), 1–8. https://doi.org/10.1007/s12526-021-01215-7

Feyrer, F., Nobriga, M. L., & Sommer, T. R. (2007). Multidecadal trends for three declining fish species: Habitat patterns and mechanisms in the San Francisco Estuary, California, USA. Canadian Journal of Fisheries and Aquatic Sciences, 64(4), 723–734. https://doi.org/10.1139/F07-048

Fry, B. (2006). Stable Isotope Ecology (521st ed.). Springer.

Giorgino, T. (2009). Computing and visualizing dynamic time warping alignments in R: The dtw package. Journal of Statistical Software, 31(7), 1–24. https://doi.org/10.18637/jss.v031.i07

Grey, A. C., & Schey, K. L. (2008). Distribution of bovine and rabbit lens α-crystallin products by MALDI imaging mass spectrometry. Molecular Vision, 14(January), 171–179.

Hadfield, J. D. (2010). MCMCglmm: MCMC Methods for Multi-Response GLMMs in R. Journal of Statistical Software, 33(2), 1–22. https://www.jstatsoft.org/v33/i02/

Hartig, F. (2022). DHARMa: Residual Diagnostics for Hierarchical (Multi-Level / Mixed) Regression Models. http://florianhartig.github.io/DHARMa/

Hazon, N., Wells, A., Pillans, R. D., Good, J. P., Anderson, W. G., & Franklin, C. E. (2003). Urea based osmoregulation and endocrine control in elasmobranch fish with special reference to euryhalinity. Comparative Biochemistry and Physiology - B Biochemistry and Molecular Biology, 136(4), 685–700. https://doi.org/10.1016/S1096-4959(03)00280-X

Heupel, M. R., Carlson, J. K., & Simpfendorfer, C. A. (2007). Shark nursery areas: Concepts, definition, characterization and assumptions. Marine Ecology Progress Series, 337, 287–297. https://doi.org/10.3354/meps337287

Heupel, M. R., Kanno, S., Martins, A. P. B., & Simpfendorfer, C. A. (2018). Advances in understanding the roles and benefits of nursery areas for elasmobranch populations. Marine and Freshwater Research, 70(7), 897–907. https://doi.org/10.1071/MF18081

Hughes, B. B., Levey, M. D., Brown, J. A., Fountain, M. C., Carlisle, A. B., Litvin, S. Y., Greene, C. M., Heady, W. N., & Gleason, M. G. (2014). Nursery functions of U.S. West Coast estuaries: The state of knowledge for juveniles of focal invertebrates and fish species. 168.

Ingram, T., Costa-Pereira, R., & Araújo, M. S. (2018). The dimensionality of individual niche variation. Ecology, 99(3), 536–549. https://doi.org/10.1002/ecy.2129

Jaenicke, R. (1999). Stability and folding of domain proteins. Progress in Biophysics and Molecular Biology, 71(2), 155–241. https://doi.org/10.1016/S0079-6107(98)00032-7

Keenan, J., Elia, G., Dunn, M. J., Orr, D. F., & Pierscionek, B. K. (2009). Crystallin distribution patterns in concentric layers from toad eye lenses. Proteomics, 9(23), 5340–5349. https://doi.org/10.1002/pmic.200800986

Kim, S. L., Casper, D. R., Galván-Magaña, F., Ochoa-Díaz, R., Hernández-Aguilar, S. B., & Koch, P. L. (2012). Carbon and nitrogen discrimination factors for elasmobranch soft tissues based on a long-term controlled feeding study. Environmental Biology of Fishes, 95(1), 37–52. https://doi.org/10.1007/s10641-011-9919-7

Kim, S. L., Del Rio, C. M., Casper, D., & Koch, P. L. (2012). Isotopic incorporation rates for shark tissues from a long-Term captive feeding study. Journal of Experimental Biology, 215(14), 2495–2500. https://doi.org/10.1242/jeb.070656

Kim, S. L., & Koch, P. L. (2012). Methods to collect, preserve, and prepare elasmobranch tissues for stable isotope analysis. Environmental Biology of Fishes, 95(1), 53–63. https://doi.org/10.1007/s10641-011-9860-9

Kim, S. L., Tinker, M. T., Estes, J. A., & Koch, P. L. (2012). Ontogenetic and Among-Individual Variation in Foraging Strategies of Northeast Pacific White Sharks Based on Stable Isotope Analysis. PLoS ONE, 7(9). https://doi.org/10.1371/journal.pone.0045068

Kimbro, D. L., Largier, J., & Grosholz, E. D. (2009). Coastal oceanographic processes influence the growth and size of a key estuarine species , the Olympia oyster. 54(5), 1425–1437.

Kuntz, J. P., Bell-Tilcock, M., Vecchio, J. L., Wallace, A. A., Sturrock, A. M., Perry, S. M., & Kim, S. L. (2024). Investigating eye lens composition for stable isotope analysis in

fishes: a comparison between Chondrichthyes and Actinopterygii. Environmental Biology of Fishes. https://doi.org/10.1007/s10641-024-01656-6

McClelland, J. W., Valiela, I., & Michener, R. H. (1997). Nitrogen-stable isotope signatures in estuarine food webs: A record of increasing urbanization in coastal watersheds. Limnology and Oceanography, 42(5 I), 930–937. https://doi.org/10.4319/lo.1997.42.5.0930

Mizuta, S., Hwang, J. H., & Yoshinaka, R. (2003). Molecular species of collagen in pectoral fin cartilage of skate (Raja kenojei). Food Chemistry, 80(1), 1–7. https://doi.org/10.1016/S0308-8146(02)00227-3

Pedersen, E. J., Miller, D. L., Simpson, G. L., & Ross, N. (2019). Hierarchical generalized additive models in ecology: An introduction with mgcv. PeerJ, 7(e6876). https://doi.org/10.7717/peerj.6876

Porter, M. E., Beltrán, J. L., Koob, T. J., & Summers, A. P. (2006). Material properties and biochemical composition of mineralized vertebral cartilage in seven elasmobranch species (Chondrichthyes). Journal of Experimental Biology, 209(15), 2920–2928. https://doi.org/10.1242/jeb.02325

Post, D. M. (2002). Using stable isotopes to estimate trophic position: Models, methods, and assumptions. Ecology, 83(3), 703–718. https://doi.org/10.1890/0012-9658(2002)083[0703:USITET]2.0.CO;2

Quaeck-Davies, K., Bendall, V. A., MacKenzie, K. M., Hetherington, S., Newton, J., & Trueman, C. N. (2018). Teleost and elasmobranch eye lenses as a target for life-history stable isotope analyses. PeerJ, 2018(6), 1–26. https://doi.org/10.7717/peerj.4883

R Core Team. (2023). R: A Language and Environment for Statistical Computing. https://www.r-project.org/

Reis-Santos, P., Gillanders, B. M., Sturrock, A. M., Izzo, C., Oxman, D. S., Lueders-Dumont, J. A., Hüssy, K., Tanner, S. E., Rogers, T., Doubleday, Z. A., Andrews, A. H., Trueman, C., Brophy, D., Thiem, J. D., Baumgartner, L. J., Willmes, M., Chung, M.-T., Charapata, P., Johnson, R. C., … Walther, B. D. (2023). Reading the biomineralized book of life: expanding otolith biogeochemical research and applications for fisheries and ecosystem-based management. Reviews in Fish Biology and Fisheries, 33(2), 411–449. https://doi.org/10.1007/s11160-022-09720-z

Russo, R. A. (2019). Primary and secondary nursery areas for leopard and brown smoothhound sharks in San Francisco Bay, California. California Fish and Game, 105(1), 21–30.

Schlacher, T. A., & Connolly, R. M. (2014). Effects of acid treatment on carbon and nitrogen stable isotope ratios in ecological samples: a review and synthesis. Methods in Ecology and Evolution, 5, 541–550. https://doi.org/10.1111/2041-210X.12183

Seidel, R., Blumer, M., Pechriggl, E. J., Lyons, K., Hall, B. K., Fratzl, P., Weaver, J. C., & Dean, M. N. (2017). Calcified cartilage or bone? Collagens in the tessellated

endoskeletons of cartilaginous fish (sharks and rays). Journal of Structural Biology, 200(1), 54–71. https://doi.org/10.1016/j.jsb.2017.09.005

Shipley, O. N., Henkes, G. A., Gelsleichter, J., Morgan, C. R., Schneider, E. V, Talwar, B. S., Frisk, M. G., & Shipley, O. N. (2021). Shark Tooth Collagen Stable Isotopes (δ15N and δ13C) as Ecological Proxies. Journal of Animal Ecology, 90(March), 2188–2201. https://doi.org/10.1111/1365-2656.13518

Shoulders, M. D., & Raines, R. T. (2009). Collagen structure and stability. Annual Review of Biochemistry, 78, 929–958. https://doi.org/10.1146/annurev.biochem.77.032207.120833

Sigman, D. M., Karsh, K. L., & Casciotti, K. L. (2009). Ocean Process Tracers: Nitrogen Isotopes in the Ocean.

Simenstad, C. a, & Wissmar, R. C. (1985). δ13C evidence of the origins and fates of organic carbon in estuarine and nearshore food webs. Marine Ecology, 22, 141–152.

Smith, S. E. (2001). Leopard Shark. California's Marine Living Resources: A Status Report. Status of the Fisheries Report - An Update through 2006, February, 14-1-14–17.

Smith, S. E., & Abramson, N. J. (1990). Leopard shark Triakis semifasciata distribution, mortality rate, yield, and stock replenishment estimates based on a tagging study in San Francisco Bay. Fishery Bulletin, 88(2), 371–381.

Sommer, T., Armor, C., Baxter, R., Breuer, R., Brown, L., Chotkowski, M., Culberson, S., Feyrer, F., Gingras, M., Herbold, B., Kimmerer, W., Mueller–Solger, A., Nobriga, M., & Souza, K. (2007). The collapse of pelagic fishes in the upper San Francisco Estuary. Fisheries, 32(6), 270–277.

Turner Tomaszewicz, C. N., Seminoff, J. A., Avens, L., & Kurle, C. M. (2016). Methods for sampling sequential annual bone growth layers for stable isotope analysis. Methods in Ecology and Evolution, 7(5), 556–564. https://doi.org/10.1111/2041-210X.12522

Tzadik, O. E., Curtis, J. S., Granneman, J. E., Kurth, B. N., Pusack, T. J., Wallace, A. A., Hollander, D. J., Peebles, E. B., & Stallings, C. D. (2017). Chemical archives in fishes beyond otoliths: A review on the use of other body parts as chronological recorders of microchemical constituents for expanding interpretations of environmental, ecological, and life-history changes. Limnology and Oceanography: Methods, 15(3), 238–263. https://doi.org/10.1002/lom3.10153

Vane, K., Cobain, M. R. D., & Larsen, T. (2025). The power and pitfalls of amino acid carbon stable isotopes for tracing the use and fate of basal resources in food webs. Ecological Monographs, 95(1), e1647. https://doi.org/10.1002/ecm.1647

Vecchio, J. L., & Peebles, E. B. (2022). Lifetime-scale ontogenetic movement and diets of red grouper inferred using a combination of instantaneous and archival methods. Environmental Biology of Fishes, 105(12), 1887–1906. https://doi.org/10.1007/s10641-022-01210-2

Vendra, V. P. R., Khan, I., Chandani, S., Muniyandi, A., & Balasubramanian, D. (2016). Gamma crystallins of the human eye lens. Biochimica et Biophysica Acta - General Subjects, 1860(1), 333–343. https://doi.org/10.1016/j.bbagen.2015.06.007

Vokhshoori, N. L., Larsen, T., & McCarthy, M. D. (2014). Reconstructing δ13C isoscapes of phytoplankton production in a coastal upwelling system with amino acid isotope values of littoral mussels. Marine Ecology Progress Series, 504(Altabet 1996), 59–72. https://doi.org/10.3354/meps10746

Wallace, A. A., Hollander, D. J., & Peebles, E. B. (2014). Stable isotopes in fish eye lenses as potential recorders of trophic and geographic history. PLoS ONE, 9(10). https://doi.org/10.1371/journal.pone.0108935

Wood, S. N. (2017). Generalized Additive Models: An Introduction with R (Second).

Xavier, J. C., Golikov, A. V, Queirós, J. P., Perales-raya, C., Rosas-luis, R., Abreu, J., Bello, G., Bustamante, P., Capaz, J. C., Dimkovikj, V. H., González, A. F., Guímaro, H., Guerra-Marrero, A., Gomes-Pereira, J. N., Hernández-Urcera, J., Kubodera, T., Laptikhovsky, V., Lefkaditou, E., Lishchenko, F., … Cherel, Y. (2022). The significance of cephalopod beaks as a research tool: An update. Frontiers in Physiology, 13(November), 1038064. https://doi.org/10.3389/fphys.2022.1038064

Zeichner, S. S., Colman, A. S., Koch, P. L., Polo-Silva, C., Galván-Magaña, F., & Kim, S. L. (2017). Discrimination factors and incorporation rates for organic matrix in shark teeth based on a captive feeding study. Physiological and Biochemical Zoology, 90(2), 257–272. https://doi.org/10.1086/689192

5.6 Figures

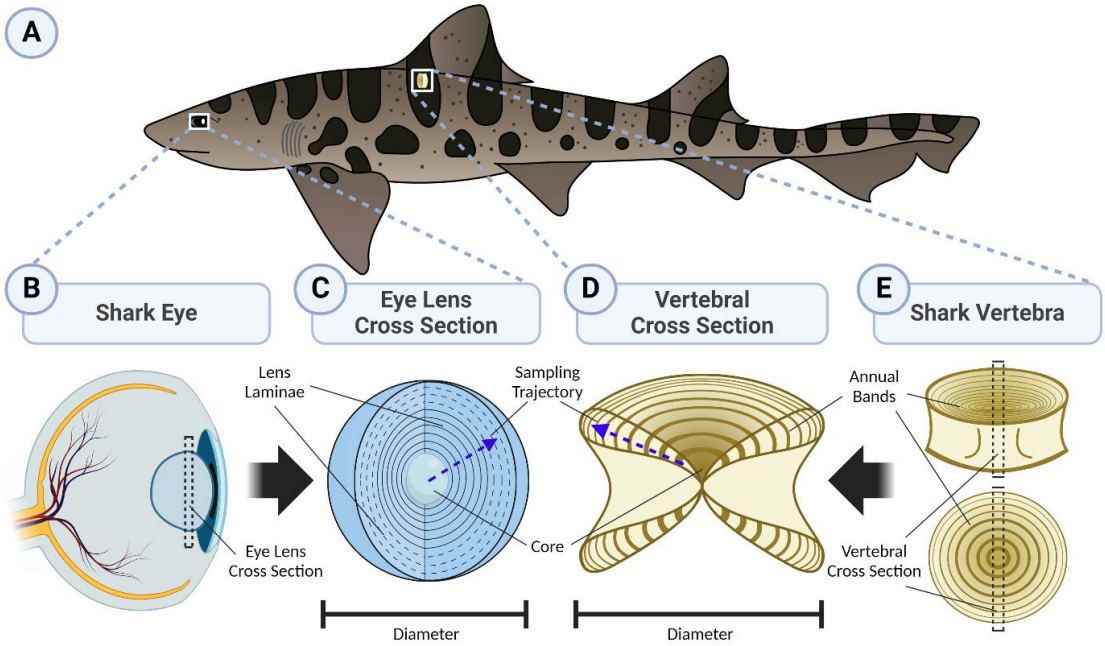

Figure 5.1: Chronological tissue types in (A) Leopard Sharks (*Triakis semifasciata*) that form inert layers across an individual's lifetime. (B) Shark's eye (anatomical depiction)

and (C) cross-section of the eye lens, showing the core (earliest formed tissue), concentric eye lens layers (laminae), increasing lens diameter with laminae formation. (E) Shark vertebra (anatomical depiction) and (D) vertebral cross-section, illustrating the vertebral core (earliest formed tissue), concentric annually deposited layers (annual bands), increasing vertebral centrum diameter with annual band formation. The blue dotted arrows represent the sampling trajectories for both tissues used in this study. Leopard Shark illustration by Adi Khen.

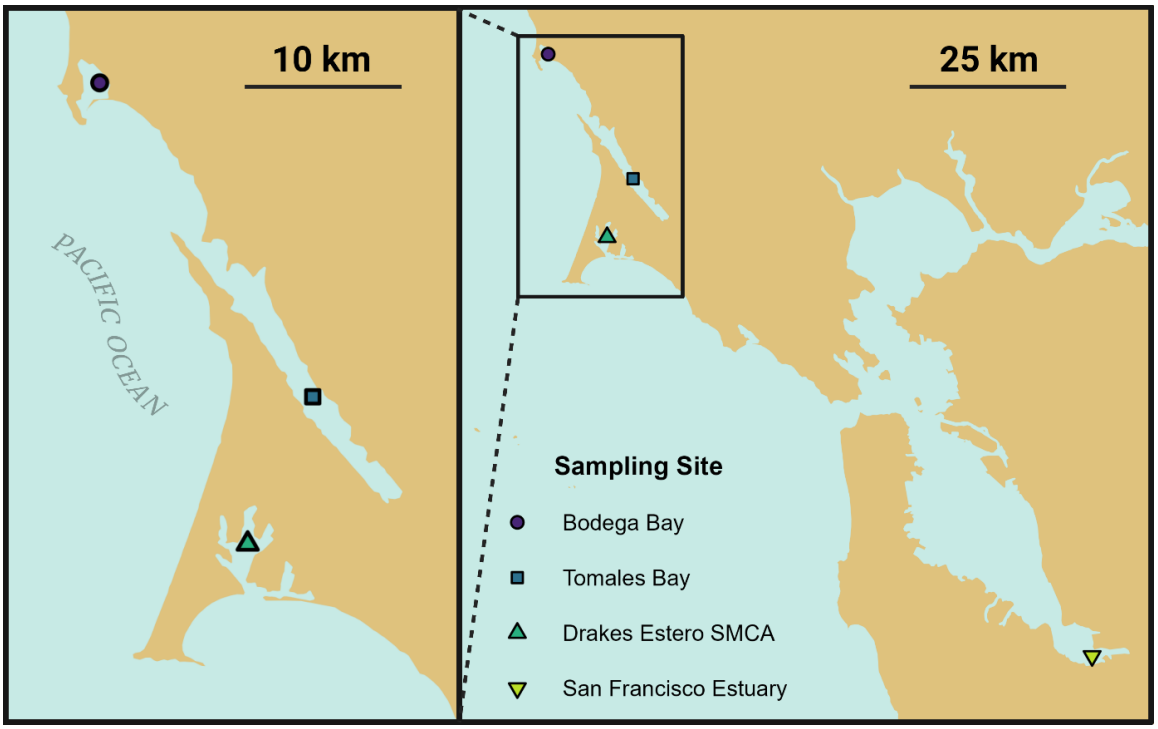

Figure 5.2: Leopard Shark sampling sites: Bodega Bay = purple circle; Tomales Bay = blue square; Drakes Estero = green triangle; the San Francisco Estuary = yellow upside-down triangle.

).

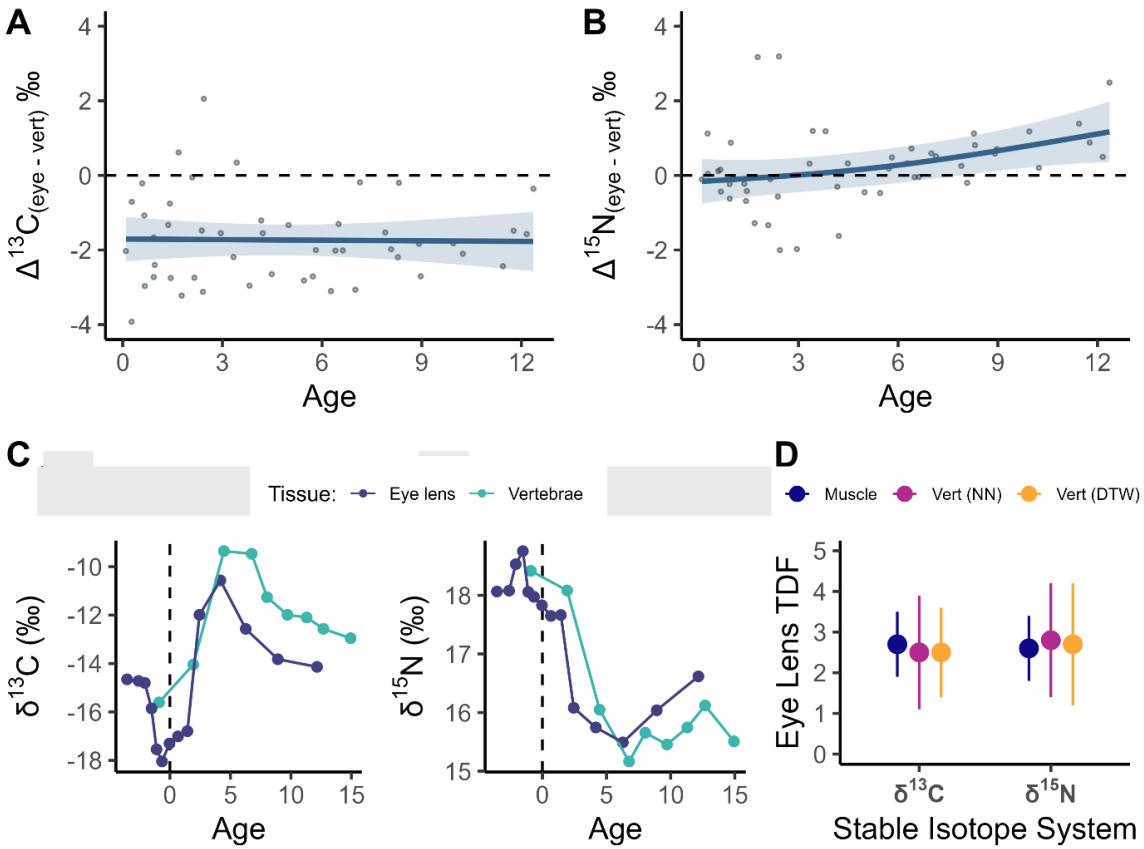

Figure 5.3: Comparison of $\delta^{13}C$ and $\delta^{15}N$ values between eye lens laminae and vertebral bands. GAM smooths of the difference between eye lens laminae and vertebral band for the (A) offset in $\delta^{13}C$ and (B) offset in $\delta^{15}N$ across age (≥ 0) using the nearest neighbor (NN) approach. (C) We also show comparisons of $\delta^{13}C$ and $\delta^{15}N$ values between eye lens laminae (dark blue) and vertebral bands (aqua) for a single specimen (Fish ID: LS_056; line plots for all individuals available in Supplemental 5.7.2, Fig. 5.7). (D) Estimated eye lens laminae trophic discrimination factors (TDFs) and propagated standard deviations for $\delta^{13}C$ and $\delta^{15}N$ of eye lens laminae in reference to (See Methods subsection 2.3 for detailed description) muscle (purple), vertebrae using NN (green), and vertebrae using dynamic time warping (DTW, yellow).

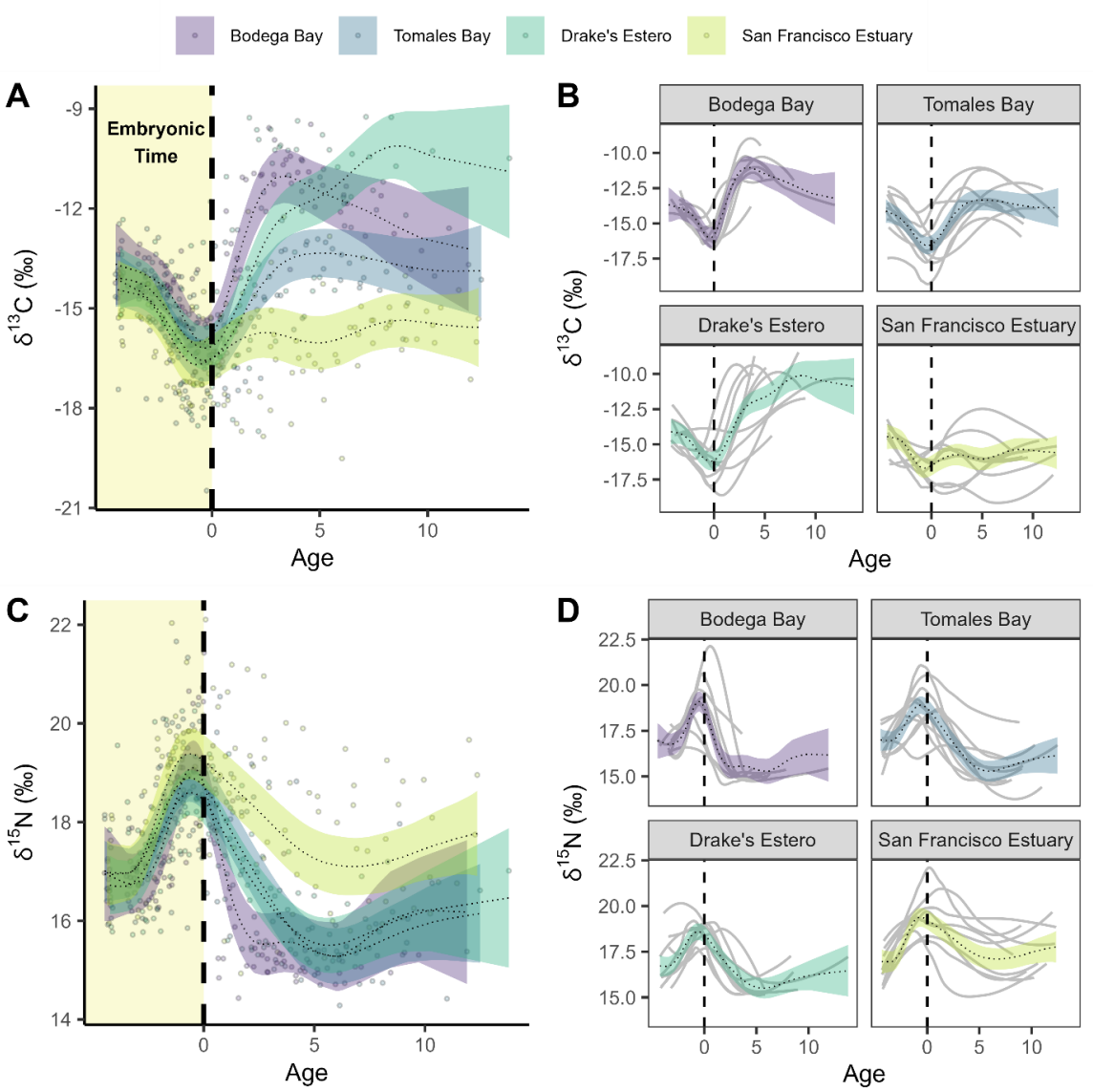

Figure 5.4: HGAM smooths of (A) $\delta^{13}C$ and (C) $\delta^{15}N$ across age for Leopard Sharks by region, with each dotted line representing the mean fit of the smooth for that region. Subpopulations HGAM smooths separated by region for (B) $\delta^{13}C$ and (D) $\delta^{15}N$, with loess smooth lines in grey for each individual within a given region. The smooth curve shaded regions indicate the 95% confidence intervals around the smooths. Regions are shown in distinct colors: purple (Bodega Bay), blue (Tomales Bay), green (Drake's Estero), and yellow (San Francisco Estuary). Vertical dashed line represents age 0 and birth, while the tan shaded region represents embryonic time.

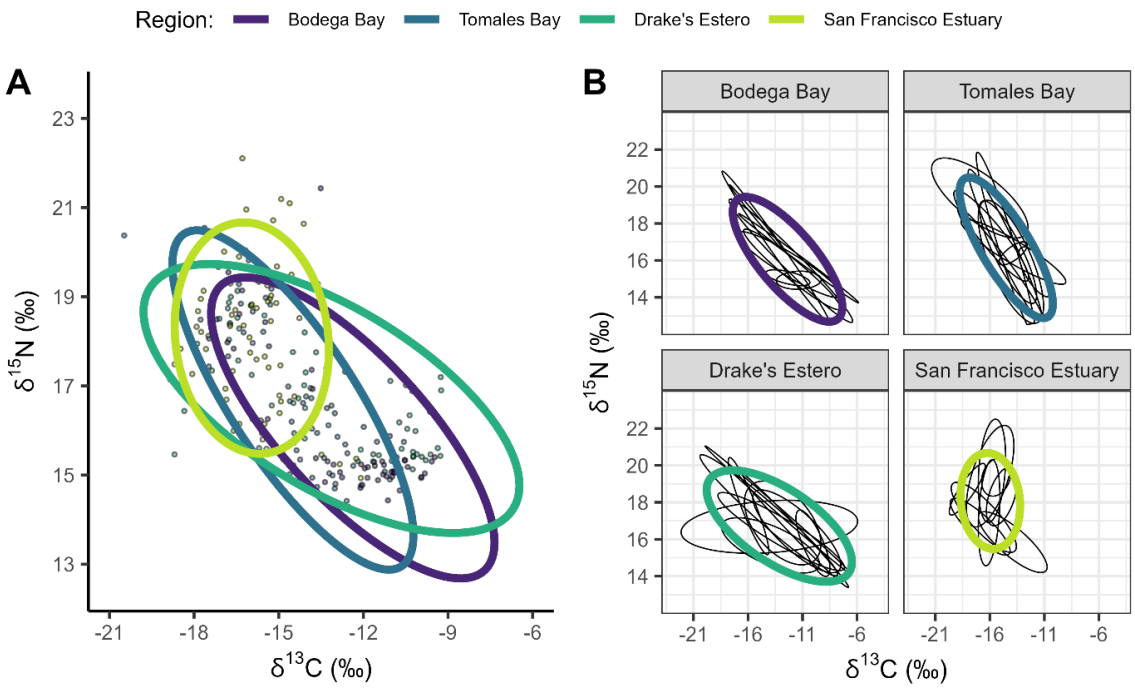

Figure 5.5: Isotopic niche ellipses for Leopard Sharks based on eye lens $\delta^{13}C$ and $\delta^{15}N$ values (age zero and older). (A) Regional ellipses represent the post-birth isospace with 95% confidence intervals based on Bayesian bivariate generalized linear models. (B) Subpopulation and individual ellipses separated by region. Regional ellipses and point colors indicate sampling of subpopulations: purple (Bodega Bay), blue (Tomales Bay), green (Drake's Estero), and yellow (San Francisco Estuary). Individual ellipses per locality are represented with black lines.

5.7 Supplemental

5.7.1 Age Estimation for Eye Lens Laminae and Vertebral Bands

The initial step in comparing eye lens laminae to a validated chronological tissue, such as vertebrae, is to standardize the growth relationships between them. While vertebral growth rates are known for Leopard Sharks (Kusher et al., 1992), eye lens growth rates remain unverified. Establishing these relationships is essential to ensuring that both tissues reflect age on the same time scale, allowing for accurate age determination of each lamina. To investigate the linear relationship of Leopard Shark total eye lens diameter versus total length, were utilized linear regression models (LMs) in the "stats" package (R Core Team, 2023). In Leopard Sharks, we found a strong linear relationship between eye lens capsule diameter and total body length (Fig. 5.6). The explanatory variable, total length (mm), accounted for a substantial portion of the variance in eye lens capsule diameter (mm), with $R^2 = 0.95$, and was statistically significant ($p < 0.001$). The resulting linear equation,

$$y = 0.005998x + 1.925, (\textbf{\textit{Equation 5.1}})$$

provides a basis for age estimation of eye lens laminae in this study. Because eye lenses and vertebral centra grow linearly with total length (Kusher et al., 1992; Quaeck-Davies et al., 2018), we can estimate the total length of the individual during the timing of tissue layer formation (L_t) in sub-adult and adult Leopard Sharks using a simple linear regression equation:

$$L_t = \frac{D_t - b}{m}, \textbf{(\textit{Equation 5.2})}$$

where D_t is the measured diameter midpoint (mm) of a given tissue (i.e., eye lens lamina or vertebral band), while b is the intercept and m is the slope of each tissue specific linear regression. These parameters for eye lenses were determined in this study, where m = 0.005998 and b = 1.925 (equation 1). While these parameters for vertebral centra were described by Kusher et al., (1992), where m = 0.010 and b = 0.737. To retroactively determine the age of each eye lens laminae and vertebral band, we then substituted the L_t term calculated from each sample for the length-at-age term (L_a) in a previously published Leopard Shark von Bertalanffy growth function (VBGF):

$$Age = t_0 - \left(\frac{log\left(1 - \frac{L_a}{L_\infty}\right)}{K}\right), \textbf{(\textit{Equation 5.3})}$$

where time-at-age-zero (t_0) = -2.03 and -2.74 for males and females, respectively; total asymptotic length (L_∞) = 1499 and 1602 mm for males and females, respectively; growth coefficient (K) = 0.089 and 0.072 for males and females, respectively (Kusher et al., 1992). This allowed for age estimation of each sample, direct comparison of isotopic patterns between tissues, and reconstruction of individual isotopic life histories across time.

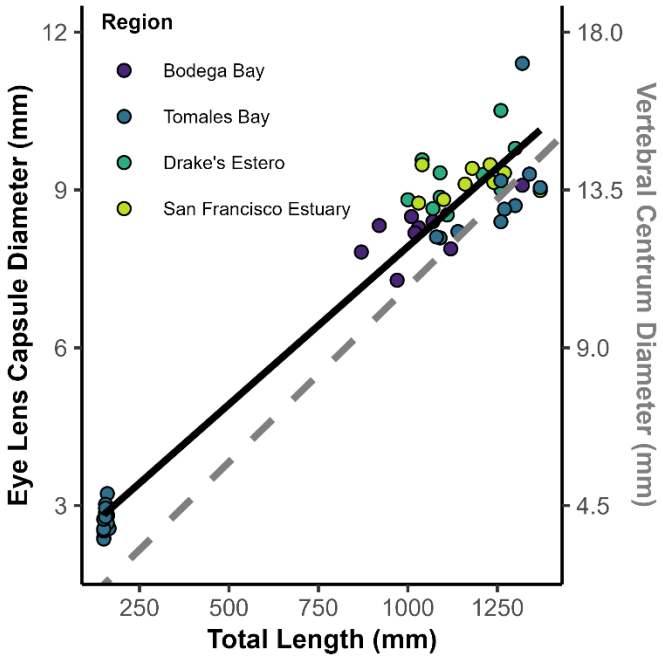

Figure 5.6: The total length of Leopard Sharks (*Triakis semifasciata*) corresponds with eye lens capsule diameter (mm) and vertebral centrum diameter (mm). Given that total length relates to age and vertebral centrum diameter is also related to age (grey dashed line; $R^2 = 0.89$; Kusher et al., 1992), eye lens capsule diameter also indicates total length and age as demonstrated with the strong correlation (black solid line; $R^2 = 0.95$; $p < 0.001$). Color of points represent region of individual sampled: Bodega Bay = purple; Tomales Bay = blue; Drake's Estero State Marine Conservation Area (SMCA) = green; the San Francisco Estuary = yellow.

5.7.2 Eye Lens and Vertebrae Isotopic Comparison

Here, we compared the stable isotope values between eye lens laminae and vertebral bands across six individuals to assess the validity of eye lenses as a chronologically recording tissue. We observed similar trends in $\delta^{13}C$ and $\delta^{15}N$ values between the two tissue substrates (Fig. 5.7); however, samples were not collected at identical time intervals. To account for this, we further analyzed the data using nearest neighbor (NN) and dynamic time warping (DTW) comparisons, as well as generalized additive models (GAMs).

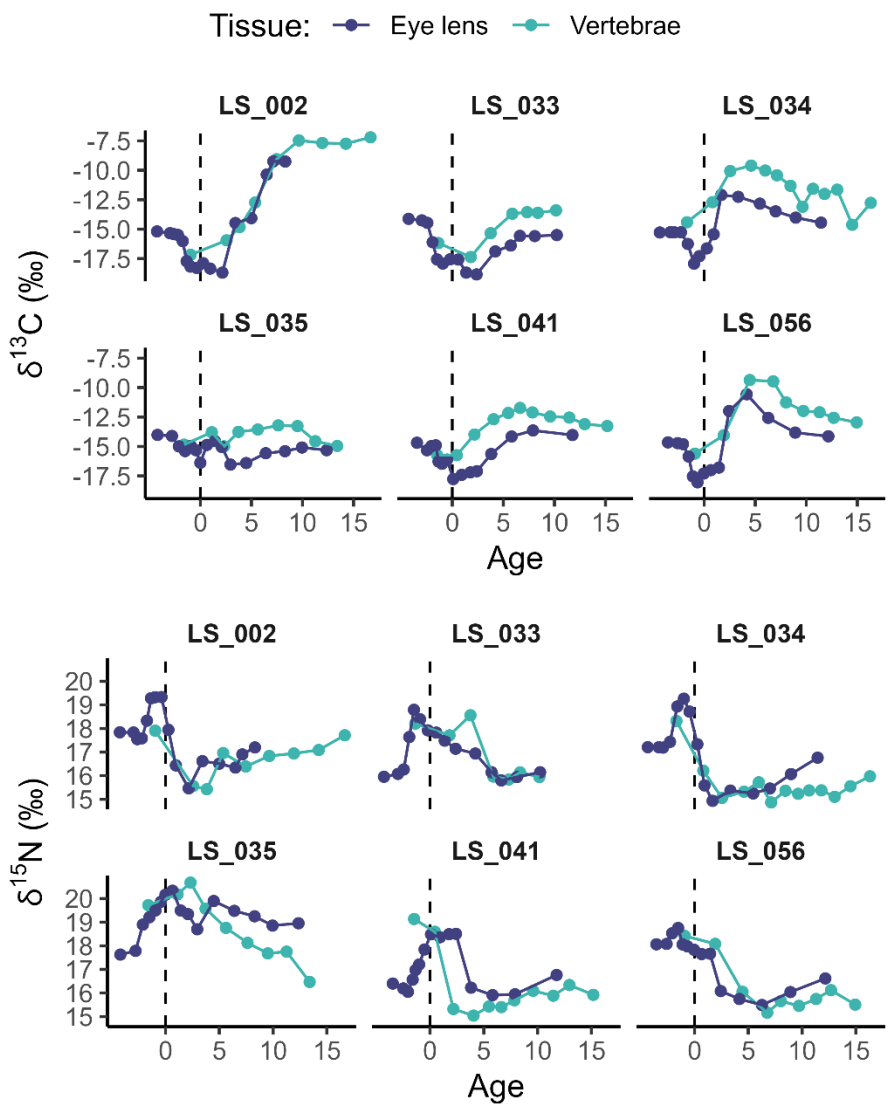

Figure 5.7: Line plots of Leopard Shark $\delta^{13}C$ and $\delta^{15}N$ values for eye lens laminae (dark blue) and vertebral bands (aqua) for all six individuals (fish id: LS_002, LS_033, LS_034, LS_035, LS_041, and LS_056). Black dashed line on x axis indicates age zero or timing of birth.

5.7.2.1 Nearest Neighbor Comparison

We noted an inconsistent offset in nearest neighbor $\delta^{13}C$ and $\delta^{15}N$ values between eye lens laminae and vertebral bands across age in GAMs that included all age data (Fig. 5.8A,C). Explanatory variables accounted for some of the variance in the response variable (difference in respective stable isotope value between tissues) for $\delta^{13}C$ and $\delta^{15}N$ GAMs which included all ages ($R^2 = 0.59$ and $R^2 = 0.31$, respectively). For both models, the explanatory variable of age (smooth term) was significant ($p < 0.001$). Additionally, while fish ID (random smooth effect) was significant in both models, its significance differed ($p < 0.001$ for $\delta^{13}C$ and $p = 0.03$ for $\delta^{15}N$). However, when only considering $\delta^{13}C$

and $\delta^{15}N$ values greater than or equal to age zero, the GAM smooths of the offset in nearest neighbor $\delta^{13}C$ and $\delta^{15}N$ values between eye lens laminae and vertebral bands across age were less variable (Fig 5.8B,D). When considering $\delta^{13}C$ and $\delta^{15}N$ values from age zero onward, the GAM smooths showed consistent trends with some variability (Fig. 5.8B,D). The $\delta^{13}C$ model explained little variance ($R^2 = 0.04$), indicating a stable offset across age (Fig. 5.8B). In contrast, the $\delta^{15}N$ model explained more variance ($R^2 = 0.23$), suggesting a slight increase in $\delta^{15}N$ differences over time (Fig. 5.8D). For more in depth age zero onward GAM results, see main text.

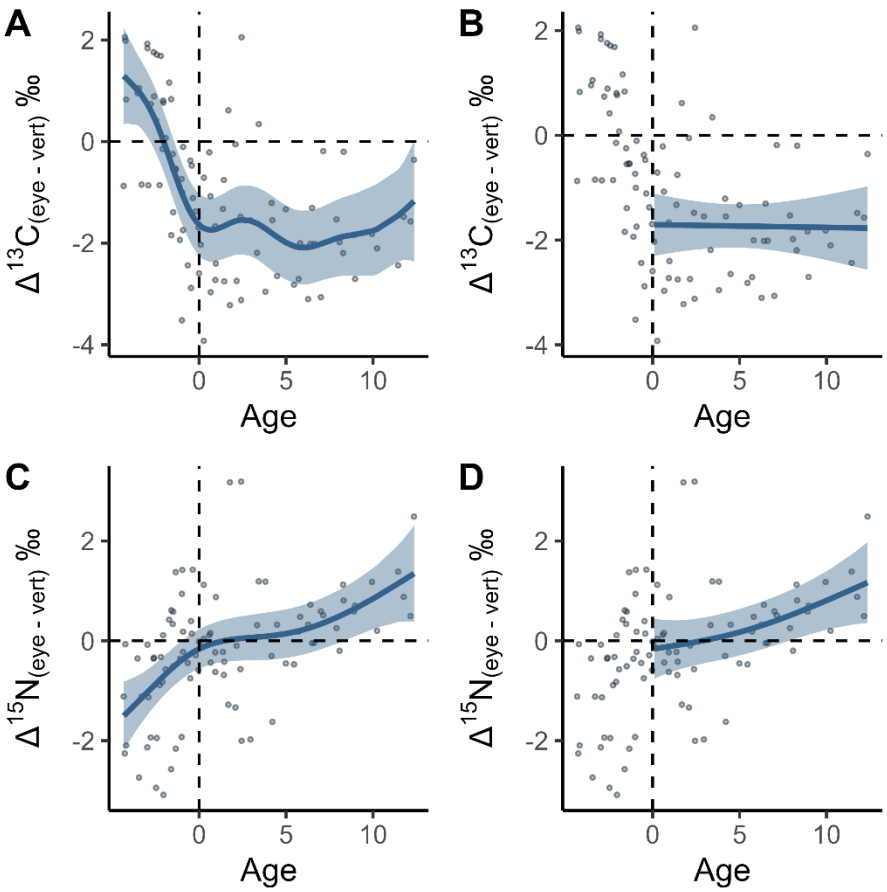

Figure 5.8: Leopard Shark GAM smooth curves of nearest neighbor isotope data between eye lens laminae and vertebral bands for all six individuals; (A) $\delta^{13}C$ difference (all data), (B) $\delta^{13}C$ difference (age ≥ 0 data), (C) $\delta^{15}N$ difference (all data), and (D) $\delta^{15}N$ difference (age ≥ 0 data) across age. Black dashed line on y axis indicates zero isotopic change, with black dashed line on x axis indicating timing of birth. Shaded region represents the 95 % confidence interval.

5.7.2.2 Dynamic Time Warping Comparison

For DTW analysis, we compared two common time point interpolated time series (n interpolated points per series = 100) for each individual, one derived from leopard Shark eye lens and the other from vertebral band isotopic data. The DTW alignment was performed using a constrained Rabiner-Juang step pattern (sub-type “C”), optimized for

minimizing local warping costs while preserving temporal consistency. We also utilized Sakoe-Chiba window with a size of 20 to limit the warping path's search space, ensuring biologically meaningful alignment within a reasonable temporal range. DTW warping paths (i.e., the alignment path of time eye lens time series to fit vertebral band time series) for $\delta^{13}C$ and $\delta^{15}N$ showed no consistent patterns (Fig. 5.9), suggesting that differences in isotopic timing across age are likely due to sampling or aging error.

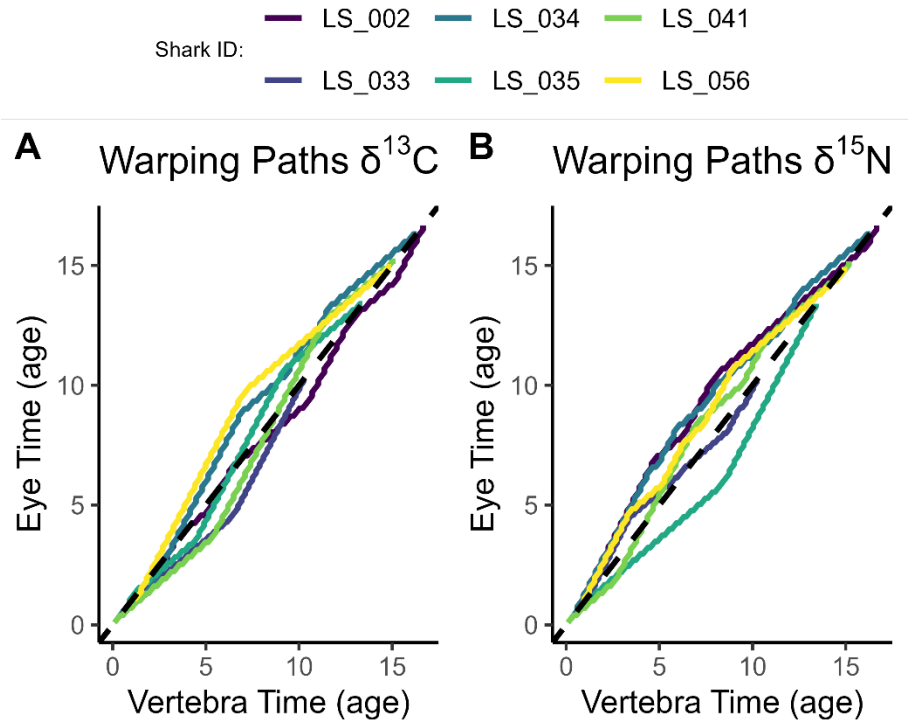

Figure 5.9: Dynamic time warping (DTW) paths for (A) $\delta^{13}C$ and (B) $\delta^{15}N$ across age in six Leopard Sharks, aligning eye lens laminae to vertebral bands. Warping paths illustrate how each time series is adjusted to minimize differences, with deviations from the dotted line (1:1) indicating mismatches in isotopic timing between tissues.

Compared to nearest neighbor GAMs, DTW $\delta^{13}C$ and $\delta^{15}N$ GAMs exhibited highly similar trends. In models using all age data, DTW $\delta^{13}C$ and $\delta^{15}N$ offsets between eye lens laminae and vertebral bands indicated a strong maternal influence prior to birth (Fig. 5.10A,C). Explanatory variables accounted for a substantial portion of variance ($R^2 = 0.58$ for $\delta^{13}C$, $R^2 = 0.44$ for $\delta^{15}N$), with age (smooth term) and fish ID (random smooth effect) both significant ($p < 0.001$ and $p = 0.03$, respectively). However, when considering only ages ≥ 0, DTW $\delta^{13}C$ and $\delta^{15}N$ offsets were less variable (Fig. 5.10B,D). The $\delta^{13}C$ model explained less variance ($R^2 = 0.21$), though age and fish id remained significant ($p < 0.001$ and $p < 0.001$, respectively), whereas the $\delta^{15}N$ model retained higher explanatory power ($R^2 = 0.41$) with significant age and fish id effects as well ($p < 0.001$ and $p < 0.001$, respectively). Lastly, we have only included nearest neighbor GAMs in the main text due to the similarity in results.

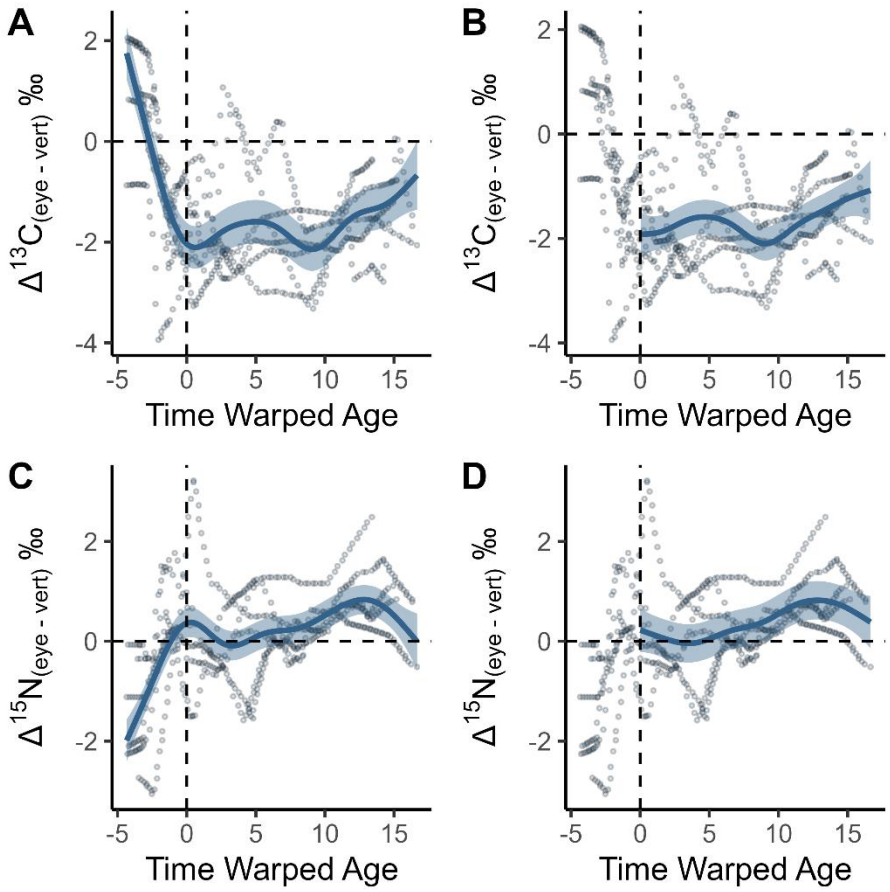

Figure 5.10: Leopard Shark GAM smooth curves of interpolated and dynamically time warped isotope data between eye lens laminae and vertebral bands for all six individuals; (A) $\delta^{13}C$ difference (all data), (B) $\delta^{13}C$ difference (age ≥ 0 data), (C) $\delta^{15}N$ difference (all data), and (D) $\delta^{15}N$ difference (age ≥ 0 data) across age. Black dashed line on y axis indicates zero isotopic change, with black dashed line on x axis indicating timing of birth. Shaded region represents the 95 % confidence interval.

5.7.3 Outer vs Inner Eye Lens $\delta^{15}N$

5.7.3.1 Amino Acid Comparison Between Tissues

Amino acids that do not undergo deamination or transamination exhibit little to no fractionation of nitrogen isotopes due to the absence of selective ^{14}N loss and are classified as 'source' amino acids, while those that do undergo these reactions retain higher proportions of ^{15}N with increasing trophic level and are termed 'trophic' amino acids (Chikaraishi et al., 2009). We observed minimal differences in $\delta^{15}N$ offsets between eye lens laminae and cartilaginous vertebrae, likely due to the similar proportions of source and trophic amino acids in the protein structure of both tissues. However, $\delta^{15}N$ offsets increased slightly with age (Fig. 5.3B), suggesting that shifts in protein composition and amino acid profiles contribute to this pattern. Cartilaginous vertebrae exhibit relatively homogeneous protein fractions and amino acid concentrations, with

type I and type II collagen containing 44.85% and 41.84% source amino acids, and 37.67% and 39.63% trophic amino acids, respectively (Table 5.1). In contrast, the eye lens exhibits regional differences in protein fractions and amino acid composition. γ-crystallin, primarily expressed during early development, is concentrated in the inner, post-apoptotic laminae (Keenan et al., 2009; Vendra et al., 2016). This crystallin protein exhibits a relatively similar amino acid composition to collagens, with 45.07% source amino acids and 40.42% trophic amino acids (Table 5.1). Conversely, α-crystallin, a chaperone protein predominantly located in the outer, pre-apoptotic laminae (Grey & Schey, 2008), contains a lower proportion of source amino acids (27.95%) and a higher proportion of trophic amino acids (57.54; Table 5.1). This compositional gradient yields $\delta^{15}N$ values in the inner, post-apoptotic eye lens laminae comparable to cartilaginous vertebrae, while the outer, pre-apoptotic laminae show elevated $\delta^{15}N$ values driven by greater trophic amino acid influence.

Table 5.1: Amino acid composition of each proteinaceous tissue.

Amino Acid	Type	Cartilage I	Cartilage II	Alpha-crystallin	Gamma-crystallin
Alanine	Trophic	11.49	9.81	3.58	1.04
Arginine	NA	5	5.11	7.65	5.49
Aspartic acid	Trophic	3.6	4.1	10.24	13.68
Cysteine	NA	0	0	0	5.18
Glutamic acid	Trophic	7.79	9.01	12.82	10.05
Glycine	NA	35.36	35.24	5.77	9.43
Histidine	NA	0.8	0.2	3.48	1.55
Hydroxylysine	NA	0.6	1.8	0	0
Hydroxyproline	NA	7.39	7.51	0	0
Isoleucine	Trophic	1.8	0.8	6.46	4.15
Leucine	Trophic	2.2	2.7	9.24	2.07
Lysine	Source	2.6	1.2	4.87	2.07
Methionine	Source	0.99	1	2.49	4.97
Phenylalanine	Source	1.2	1.2	5.67	7.15
Proline	Trophic	8.29	11.31	10.64	5.49
Serine	NA	4.5	3	7.06	8.29
Threonine	NA	3.7	3.9	3.38	2.28
Tyrosine	NA	0.2	0.2	2.09	13.16
Valine	Trophic	2.5	1.9	4.57	3.94

Note: Type refers to trophic or source amino acid for nitrogen isotopes and are from Grey & Schey (2008); Cartilage I and Cartilage II values are from Nuche-Pascual et al. (2021); Alpha- and Gamma-crystallin values are from Mizuta et al (2003). Values are in percent (%).

5.7.3.2 References

Chikaraishi, Y. et al. Determination of aquatic food-web structure based on compound-specific nitrogen isotopic composition of amino acids. Limnol. Oceanogr. Methods 7, 740–750 (2009).

Keenan, J., Elia, G., Dunn, M. J., Orr, D. F. & Pierscionek, B. K. Crystallin distribution patterns in concentric layers from toad eye lenses. Proteomics 9, 5340–5349 (2009).

Vendra, V. P. R., Khan, I., Chandani, S., Muniyandi, A. & Balasubramanian, D. Gamma crystallins of the human eye lens. Biochim. Biophys. Acta - Gen. Subj. 1860, 333–343 (2016).

Grey, A. C. & Schey, K. L. Distribution of bovine and rabbit lens α-crystallin products by MALDI imaging mass spectrometry. Mol. Vis. 14, 171–179 (2008).

Nuche-Pascual, M. T., Ruiz-Cooley, R. I. & Herzka, S. Z. A meta-analysis of amino acid $\delta^{15}N$ trophic enrichment factors in fishes relative to nutritional and ecological drivers. Ecosphere 12, (2021).

Mizuta, S., Hwang, J. H. & Yoshinaka, R. Molecular species of collagen in pectoral fin cartilage of skate (Raja kenojei). Food Chem. 80, 1–7 (2003).

Bloemendal, H. Molecular and cellular biology of the eye lens. (John Wiley & Sons, 1981).

5.7.4 Maternal Influence

5.7.4.1 Metabolic Fractionation during Embryonic Development

In this study, the majority of individuals from all localities exhibited remarkably similar patterns of eye lens laminae $\delta^{13}C$ and $\delta^{15}N$ values during embryonic development and until birth (Fig. 5.4). The species reproduce via ovoviviparity, where females carry egg sacs with sufficient yolk to nourish embryos until they hatch internally, and subsequently give birth to live young. The yolk, derived from the mother's diet during its formation, supports the embryo's metabolic and protein synthesis demands throughout development and serves as the source of stable isotope variation routed from maternal nutrition (Olin et al., 2018; Shipley et al., 2022). The increasing $\delta^{15}N$ patterns prior to birth reflect trophic fractionation, driven by embryos feeding on this maternal yolk (Olin et al., 2018; Shipley et al., 2022). A similar consistency is observed in embryonic $\delta^{13}C$ patterns; however, $\delta^{13}C$ values decrease prior to birth, deviating from the expected pattern of trophic fractionation. This opposite trend likely reflects a metabolic effect, where the high lipid content of the yolk, which has lower $\delta^{13}C$ values, is increasingly being fractionated and metabolized for protein synthesis. Regardless of metabolic effects, individual Leopard Sharks exhibited $\delta^{13}C$ and $\delta^{15}N$ variations within regions both prior to and at birth (Fig. 5.4). The regionally distinct isotopic trends observed in eye lens laminae of sharks older than three years (Fig. 5.4), combined with the fact that embryos inherit their nutrient isotopic composition from their mother's diet, imply that adult females' yolk stable isotope values—reflecting their diets—also vary regionally. These variations likely arise from spatial differences in the baseline isotope values of primary producers, driven by the distinct nutrient sources available in each locality.

5.7.4.2 References

Olin, J. A., Shipley, O. N., & Mcmeans, B. C. (2018). *Stable isotope fractionation between maternal and embryo tissues in the Bonnethead shark (Sphyrna tiburo)*. 489–499.

Shipley, O. N., Olin, J. A., Whiteman, J. P., Bethea, D. M., & Newsome, S. D. (2022). Bulk and amino acid nitrogen isotopes suggest shifting nitrogen balance of pregnant sharks across gestation. *Oecologia*, *199*(2), 313–328. https://doi.org/10.1007/s00442-022-05197-6

6. Summary & Conclusion of the Dissertation

6.1 Summary and Conclusion

Understanding the ecology of estuarine chondrichthyans like the Leopard Shark presents substantial challenges due to their cryptic behaviors, site-specific movements, and exposure to highly dynamic environmental gradients. These complexities are further intensified in urbanized estuaries such as SFBE, where nutrient loading, habitat alteration, and legacy contaminants have reshaped ecological processes. Compounding these issues is the lack of temporally resolved ecological baselines, which limits our ability to evaluate how mesopredators like Leopard Sharks respond to long-term anthropogenic stressors and climate-driven change.

To address these knowledge gaps, this dissertation investigates the trophic ecology, habitat use, and subpopulation connectivity of Leopard Sharks across Northern California estuarine and coastal systems using a suite of stable isotope tools, including bulk SIA and CSIA-AA. By focusing on four representative estuarine-coastal systems—SFBE, Drake's Estero, Tomales Bay, and Bodega Bay—this work provides a spatially and temporally nuanced understanding of Leopard Shark ecology in the context of shifting environmental baselines.

To first understand isotopic variation across the SFBE, chapter 1 constructs spatially explicit $\delta^{13}C$ and $\delta^{15}N$ isoscapes for his ecosystem, revealing fine-scale biogeochemical gradients shaped by hydrodynamics, land use, and anthropogenic inputs. These isoscapes delineate the relative influence of terrestrial, estuarine, and marine carbon sources while pinpointing $\delta^{15}N$ enrichment zones linked to wastewater effluent and altered residence times. These maps serve as critical tools for interpreting animal movement, foraging, and nutrient cycling across estuarine gradients.

Building on this foundation, chapter 2 uses muscle and tooth isotopes to evaluate seasonal habitat use and test assumptions of broad-scale estuarine migration in adult Leopard Sharks. Distinct isotopic profiles at each site indicate long-term residency and limited inter-estuarine movement, while elevated $\delta^{15}N$ values in SFBE sharks suggest a unique anthropogenic nitrogen baseline. CSIA-AA $\delta^{13}C$ data reveal that estuarine and coastal habitats support distinct basal productivity channels, highlighting dietary plasticity in response to local food web structures rather than regional migration.

Chapters 3 and 4 introduce and validate the use of eye lens laminae as a novel chronological substrate for reconstructing chondrichthyan life histories. Traditionally, vertebral bands have served this purpose, but they are labor-intensive to process and chemically complex to interpret. Chapter 3 explores the chemical composition across sequential laminae of the eye lens, revealing two distinct zones: a pre-apoptotic region near the core and a post-apoptotic region toward the outer layers. The pre-apoptotic laminae were found to contain elevated urea concentrations, a known potential source of

bias for $\delta^{15}N$ values. However, our analysis demonstrated that urea concentrations in these Leopard Sharks were not high enough to alter $\delta^{15}N$ values beyond analytical error, thereby supporting the integrity of nitrogen isotope records across the entire lens.

Finally, chapter 4 compares stable isotope profiles from eye lenses and vertebrae, revealing consistent $\delta^{13}C$ and $\delta^{15}N$ trends with predictable offsets, further validating eye lenses as a reliable tissue for reconstructing ontogenetic shifts. A case study across four Northern California sites showed that the SFBE Leopard Shark subpopulation exhibits lifelong site fidelity, while individuals from other locations likely migrated out of this estuarine nursery and remained within their respective regions into adulthood. These findings not only confirm the utility of eye lenses in elasmobranch research but also highlight the ecological uniqueness and conservation vulnerability of the SFBE subpopulation.

Overall, this dissertation provides a critical framework for understanding how estuarine predators interact with rapidly changing coastal environments. By integrating spatial isoscapes, temporally resolved isotope data, and novel analytical methods, this research offers actionable insights into the conservation of mobile estuarine mesopredators. These findings underscore the importance of site fidelity, the role of anthropogenic baselines in shaping trophic structure, and the need for high-resolution ecological baselines to predict species responses to environmental change. Together, they offer a foundation for future research and management strategies aimed at preserving ecological function in urbanized estuarine ecosystems.